MEASUREMENT OF THE *W* BOSON MASS

BY
DAVID P. SALTZBERG

DECEMBER 1994

Enrico Fermi Institute

The University of Chicago

Dissertation

THE UNIVERSITY OF CHICAGO

MEASUREMENT OF THE W BOSON MASS

A DISSERTATION SUBMITTED TO
THE FACULTY OF THE DIVISION OF THE PHYSICAL SCIENCES
IN CANDIDACY FOR THE DEGREE OF
DOCTOR OF PHILOSOPHY

DEPARTMENT OF PHYSICS

BY
DAVID P. SALTZBERG

CHICAGO, ILLINOIS
DECEMBER 1994

TABLE OF CONTENTS

Chapter

Appendix

LIST OF TABLES

LIST OF ILLUSTRATIONS

ABSTRACT

This thesis presents a measurement of the mass of the W boson using data collected during the 1992-93 collider run at the Fermilab Tevatron with the Collider Detector at Fermilab (CDF). A fit to the transverse mass spectrum of a sample of 5718 $W \rightarrow e\nu$ events recorded in an exposure of 18.2 pb^{-1} gives a best value of 80440 ± 145 (stat.)) ± 180 (syst.) MeV/c^2. The implications of this result for the Standard Model of the electroweak interaction are discussed.

ACKNOWLEDGEMENTS

The success of this experiment is due to the hard work of an extraordinary number of people involved in constructing and maintaining the accelerator and apparatus, calibrating the detectors, providing data and other resources, and giving physics advice. I cannot thank these hundreds individually, but I am indebted to them all for making this thesis possible and for enriching my experience as a graduate student.

I thank my advisor, Henry Frisch. He showed me that I really was interested in doing particle physics with the world's highest-energy collisions and not in something sensible. He always encouraged me to develop my ideas, many of which I certainly would have abandoned too quickly without his faith. He has an uncanny ability for identifying the most interesting and fruitful points to pursue in an analysis, a new piece of electronics, improvements to the trigger, or a new monitoring program. I learned from him much of how I think about physics, about starting and finishing projects, to look for interesting diversions, and how to get along with my collaborators. As a result, these five years have been more rewarding than I could have imagined. While I now thank many people for their help in particular projects and details, Henry was always deeply involved and guiding me through all of them. As my advisor and friend, Henry has been a profound influence.

I thank Claudio Campagnari and Marshall Miller for getting me started at B0 with the trigger. I thank Myron Campbell for his instruction and patience while I was resurrecting the Chicago level-two teststand and learning my way around the trigger. Leslie Rosenberg gave me help with a bad-tempered PDP-11. I thank my fellow trigger factotums, Bill Badgett and Soo Bong Kim, for sharing the pager and for the commiseration while we chased flakiness in the hardware. I further thank Kevin Burkett, Milciades Contreras, Sarah Eno, Mark Krasberg, Sacha Kopp, Jim Romano, and Jinsong Wang for time we spent in the trigger room. I thank Steve Hahn, Jim Hylen and Jim Patrick for training me as an "Ace" and for their continuous presence in the control room, keeping the experiment running.

Sarah Eno showed me the way through the morass of the CDF analysis package and spent much time discussing the strategy of the W mass analysis with me. I thank her for advice while I was working on hardware, making datasets, monitoring the data, and trying to measure the W mass. She also performed important studies of the W recoil. Sarah was always willing to discuss my latest idea or problem—I am sure she will make a terrific advisor now that she is Professor Eno.

The support of the EFI Electronics Development Group was essential to preparing the trigger for Run-1A. John Dudas and Son Mai make board modifications that are works of art. Mike Zeleznik helped with the CAD system, and Greg Snllivan looked over my shoulder, while I was designing the Nemesis board. I thank Harold Sanders for answering all my stupid questions, but not without making me think first.

Sacha Kopp and Jim Romano for made PHYSMON sophisticated enough to be worthwhile. Kaori Maeshima and Jim Patrick provided invaluable help integrating the package with the data-taking in the control room. I thank Marcus Hohlmann for not letting PHYSMON die at the end of Run-1A. I apologize to the handscanners; I am reminded of "The Ballad of John Henry."

Larry Nodulman provided the final false curvature removal in the CTC and, with Karen Byrum, the relative CEM gain calibration. He paid excruciating attention to the systematic uncertainties in this thesis and continually challenged my understanding of the measurement. I admire his ability to distill complex relationships down to simple rules of thumb. His efforts contributed greatly to the quality of the result.

William Trischuk, Phil Schlabach, Larry Nodulman, Barry Wicklund, Steve Errede, and Morris Binkley blazed a trail for this measurement. Steve Hahn and Gary Houk achieved the accurate source calibration of the CEM towers and, with Marcus Hohlmann, helped analyze the calibration runs. Kaori Maeshima and Stephan Lammel made the data available through the "Expressline" data reconstruction. Sacha Kopp and Carla Pilcher assembled the "good-run" list. I thank Aseet Mukherjee for the arduous CTC calibration and for making sure I was reconstructing tracks properly. Peter Berge also helped me understand tracking. Hans Jensen pointed out the importance of the magnetic field map. I thank Jim Hylen for his measurement of the magnetic field intensity inside the solenoid. Barry gave valuable advice and ideas about electrons. I thank Mel Shochet for his advice on this analysis and other projects through the years and for proofreading this thesis. A. Castro, R. Kadel, S. Park, K. Ragan, F. Snider, J. Tonnison, and R. L. Wagner for catalogued and checked the material inside the tracking volume. Bill Ashmanskas, Pat Lukens, and Barry Wicklund performed beautiful studies of this material using photon conversions.

Randy Keup and Young-Kee Kim are helping to the bitter end.

Randy measured the CTC absolute momentum scale and provided additional understanding of the W recoil model. I thank Young-Kee for her systematics studies, for gathering so many experts biweekly, and for keeping everyone focussed on getting a high-quality measurement finished quickly.

The graduate students, post-docs and others at the University of Chicago and in the CDF collaboration made my stay here even more enjoyable. They took breaks to talk about their analyses, the latest interesting events, coping with the latest offline problem, or preferably about something completely unrelated.

The National Science Foundation provided three years of support. I thank David Grainger for a fellowship for this last year. I thank Goldie Sugarman for her recognition of this work.

Finally, I thank my family—my parents and Carol, Linda, Stuart, and Rick for nurturing my interest in science. Their love and encouragement made it possible for me to attend school through the 22nd grade.

Chapter 1

INTRODUCTION

The development of a unified theory of the electromagnetic and weak forces [1] marked an important step towards understanding the interactions among elementary particles. The combined theory, now called the "Standard Model of the Electroweak Interaction," has been proven extraordinarily successful by over two decades of diverse experiments [2]. However, the theory displays unexplained symmetries and also requires that the measured values of many physical constants be added to the theory by hand. A deeper theory might predict the values of some of these observable quantities and explain the underlying symmetries. There are at least two paths on which experiments could motivate a more comprehensive theory. First, such a theory may arise from the direct discovery of new phenomena. Second, the theory can be tested by making precise and probing measurements in search of contradictions with the theory. The measurement of the W mass is a step down the second path.

As shown in Figure 1.1, most electroweak experiments may be categorized as those probing neutral- versus charged-current interactions, where neutral-currents involve the exchange of the photon or a Z boson and charged-

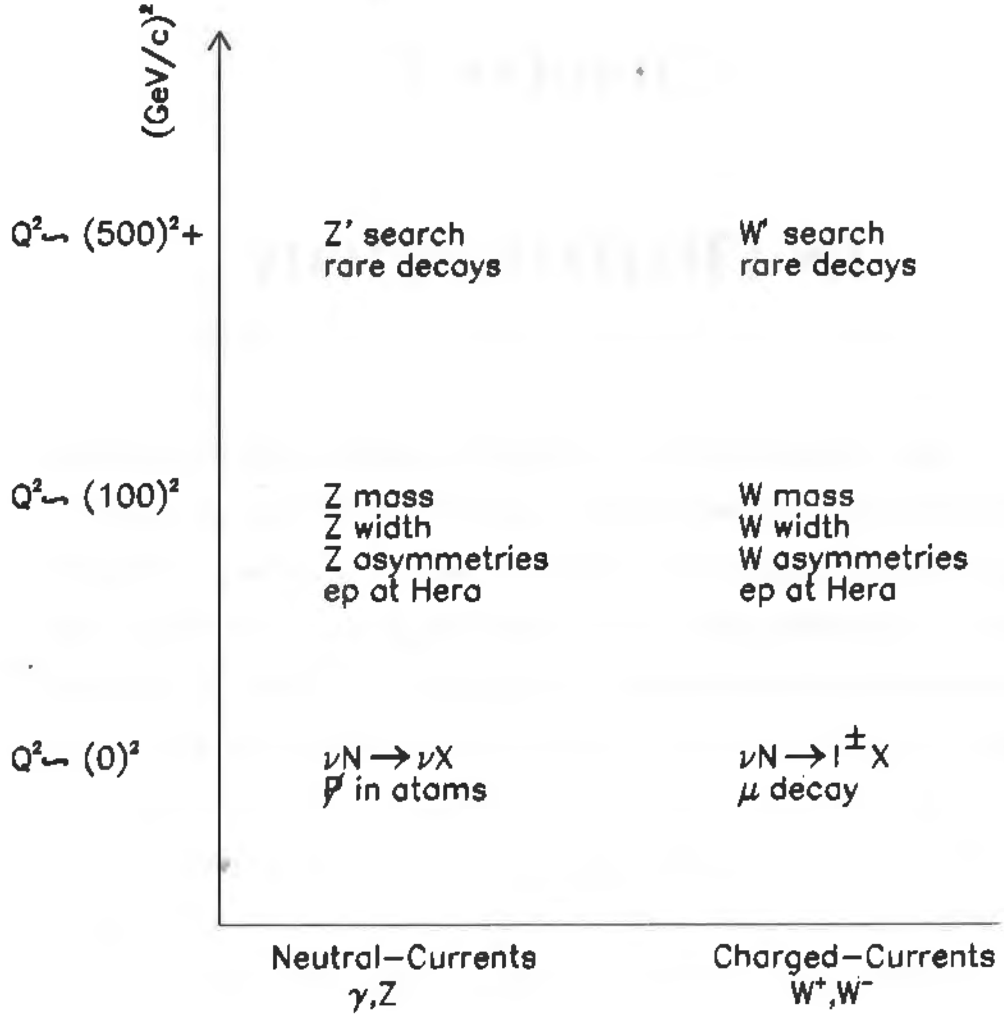

Figure 1.1: Where different experiments probe the electroweak Standard Model.

Mass ($\mathrm{GeV/c^2}$)	Experiment	Reference
81 ± 5	UA1-83	[3]
80^{+10}_{-6}	UA2-83	[4]
83.5 ± 2.9	UA1-86	[5]
80.2 ± 1.5	UA2-87	[6]
80.0 ± 4.1	CDF-89	[7]
80.53 ± 0.49	UA2-90	[8]
79.91 ± 0.39	CDF-90	[9]
80.36 ± 0.37	UA2-92	[10]

Table 1.1: Some previously published W mass measurements. Not all of the above measurements are independent.

currents involve the exchange of a W^+ or W^- boson. These experiments may also be divided into those at low versus high Q^2, where Q^2 denotes the approximate squared momentum transfer characterizing the interaction. Precise probes of electromagnetism and measurements of the properties of Z production and decay serve as tests of the neutral-currents at low and high Q^2, respectively. Deep inelastic scattering of neutrinos from nuclei and precise measurements of the properties of muon decay and atomic transitions in Cesium probe only at low Q^2. The measurement of the W mass is one of the few measurements which is sensitive to the presence of new physical phenomena involving charged currents at high Q^2.

A summary of previously published measurements of the W mass is given in Table 1.1. This work will achieve a precision nearly twice that of the best previously published value.

This thesis describes the measurement of the W mass using W bosons produced in antiproton-proton ($\overline{p}p$) collisions at the Fermilab Tevatron [11] with a center-of-mass collision energy of 1800 GeV. Specifically, this thesis presents an analysis of the decays of the W into an electron and neutrino from a dataset with a luminosity of 18.2 pb^{-1} collected by the Collider Detector at Fermilab (CDF) from August 1992 to May 1993.

In Chapter 2, an overview of the analysis strategy is described along with the critical detector components. In Chapters 3 and 4, the calibration and understanding of the detector response to the electron from a W decay are described. The measured masses of the Υ and Z resonances are used as a check. In Chapter 5, the reconstruction of the detector response to the rest of the particles in the event, necessary to infer the neutrino momentum, is described. In Chapter 6, the event modeling is described. Chapter 7 shows how the presence of background processes is handled. Chapter 8 gives details of the fitting method used to extract the W mass from the data. In Chapter 9, the value of the W mass is presented and the the experimental uncertainties are summarized. The measured W mass is compared to previous measurements and current predictions. The implications of this measurement for the Standard Model are discussed.

Chapter 2

OVERVIEW

This chapter provides an overview of the analysis. It begins with a discussion of how the nature of W boson production and decay motivates the strategy used to measure the W mass. A short description of the detectors critical to the measurement follows. The basic strategy of the mass scale calibration, crucial to this measurement, is described. A brief description of the datasets required for calibrations and for measuring the W mass is given. Finally, an outline of how the W mass is extracted from the calibrated data is provided.

2.1 Nature of W Events

The production of W bosons is described at lowest order by the Drell-Yan process [12], where a quark and antiquark in the antiproton-proton collision annihilate to produce a W boson as illustrated in Figure 2.1. The W is produced with momentum relative to the center of mass of the antiproton-proton collision in the transverse and longitudinal directions. This momentum is balanced by an energy flow of hadronic particles, referred to as "recoil"

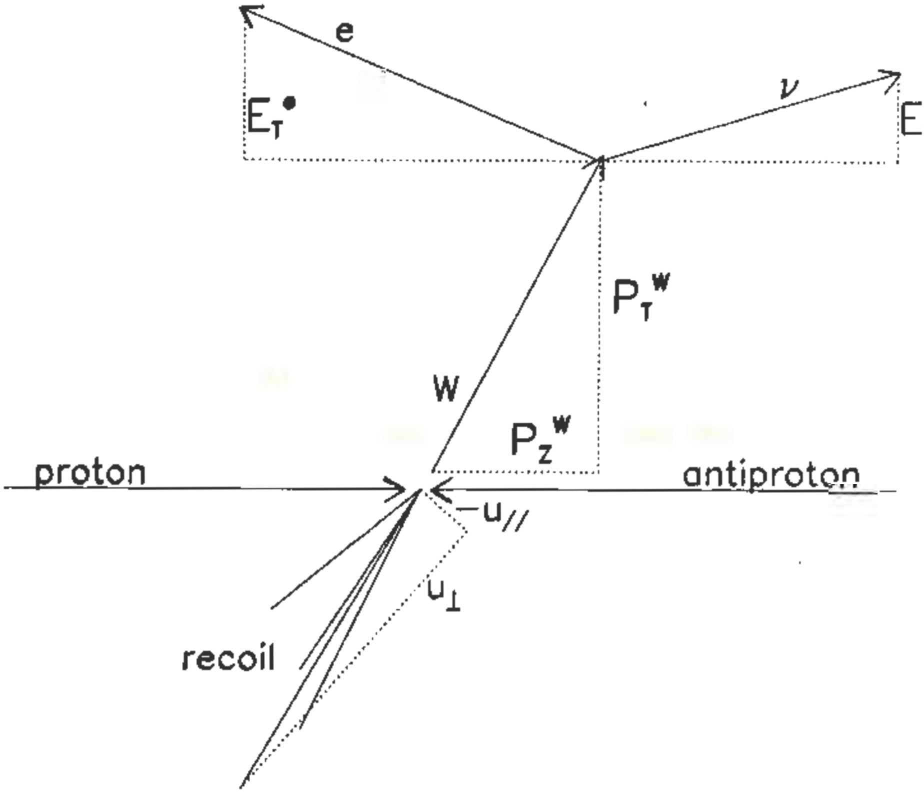

Figure 2.1: Kinematics of W boson production and decay for the events used in this analysis.

in this thesis. The W bosons used in this analysis have decayed into an electron and a neutrino. Since the apparatus cannot detect the neutrino and cannot measure the z-component of the recoil momentum, there is insufficient information to reconstruct the invariant mass of the W on an event-by-event basis. Rather, this analysis constructs the *transverse mass* of each W event, which is analogous to the invariant mass except that only the components of energy flow transverse to the beamline are used. Specifically,

$$(M_T c^2)^2 = (E_T^e + E_T^\nu)^2 - (\mathbf{E_T^e} + \mathbf{E_T^\nu})^2, \qquad (2.1)$$

where M_T is the transverse mass of the W, c is the speed of light, E_T^e is the transverse energy of the electron, and E_T^ν is the transverse energy of the neutrino.[1] The boldface denotes two-component vector quantities. The masses of the decay products are negligible and treated as zero. The energy of the neutrino is not measured, but rather is inferred using conservation of momentum. Specifically,

$$\mathbf{E_T^\nu} = -(\mathbf{E_T^e} + \mathbf{u}), \qquad (2.2)$$

where $\mathbf{E_T^\nu}$ and $\mathbf{E_T^e}$ are the transverse energy vectors of the neutrino and electron, and $\mathbf{u}$ denotes the transverse energy vector of the recoil.

When $|\mathbf{u}| \ll E_T^e$, the transverse mass measurement of Equation 2.1 becomes

$$(M_T^W c^2) \approx 2E_T^e + u_{//}, \qquad (2.3)$$

where $u_{//}$ is the transverse energy of the recoil projected along the azimuthal direction of the electron. The resolutions on the measurements of the electron energy and recoil must be understood to make adequate predictions of the

---

[1] Although energy is a scalar quantity, "transverse energy" commonly denotes the transverse component of a vector whose *magnitude* is a particle's energy measured in a calorimeter and *direction* is parallel to the particle's momentum.

transverse mass shape. In addition, effects which systematically bias the measurement components of the recoil vector **u** along the electron direction must be considered. Note that Equation 2.3 is shown only to illustrate these points and that Equation 2.1 is the definition of transverse mass used everywhere in this analysis.

2.2 The Detector

This section briefly describes the CDF detector [13] and provides references for more detailed information. The CDF detector is shown in Figure 2.2.

The momentum of a charged particle is measured from the curvature, azimuthal angle, and polar angle of the track left in the tracking devices, the vertex time projection chamber (VTX) [14] and the central tracking chamber (CTC) [15], as the particle traverses a magnetic field which points almost parallel to the beamline. The VTX and CTC are immersed in this largely axial magnetic field. For the purposes of triggering [16] and dataset selection, the field is treated as a 1.4116 T uniform axial field, and the drift times are set assuming an estimate of the positions and potentials of the field and sense wires. The momenta of tracks from W electrons reconstructed with the final calibration usually differs from those using this approximation by less than 10% and the average differs by less than 0.1%. The CTC momentum measurement is the ultimate source of all energy calibrations in this experiment.

The energy of a central electron is measured from the electromagnetic shower it produces in the central electromagnetic calorimeter (CEM) [17]. For the purposes of triggering and dataset selection, the CEM calibrations are derived from testbeam data taken during 1984-85. To compensate for scintillator

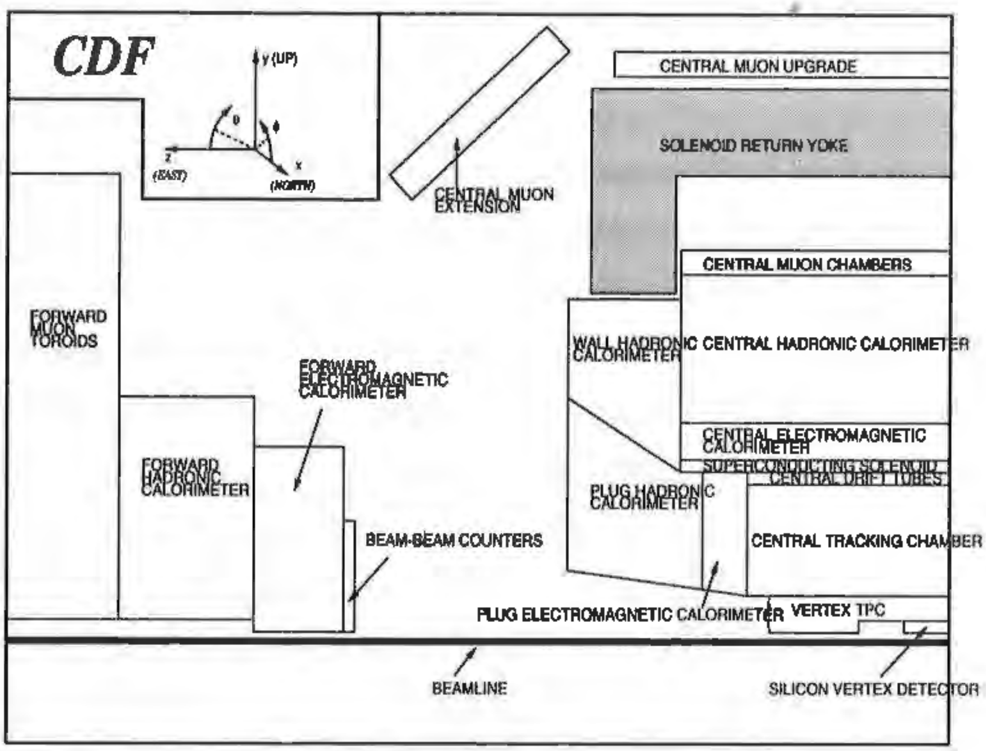

Drawing by R. Keup

Figure 2.2: One quarter of the CDF detector. The other quadrants are essentially symmetric about the interaction point which is on the lower right of this picture.

aging, the gains were set in early 1992 using Cesium-137 gamma-ray sources which may be moved along each calorimeter tower at a depth corresponding to electron shower maximum ($\sim 6\ X_0$). The final calibration, derived from the CTC momentum scale in Chapter 4, differs from this calibration with an RMS spread of 3.4%, while the average was correct to better than 1%. Throughout this thesis, momentum measurements by the CTC are denoted as p and calorimeter energy measurements are denoted as E.

Muons created with pseudorapidity[2] $|\eta| < 0.6$ pass through the CEM and the calorimeter behind it, the central hadronic calorimeter (CHA) [18], leaving a minimum-ionizing energy deposition, typically ~ 3 GeV. The muon subsequently traverses two sets of drift chambers, the central muon chambers (CMU and CMUP) [19], separated by 0.6 m of steel. Muons emerging at polar angles closer to the beamline ($1.1 < |\eta| < 0.6$), cross a different set of drift chambers, the central muon extension (CMX). To identify muons, the tracks in either of these chambers are matched to CTC tracks associated with minimum-ionizing calorimeter energy depositions.

For the W events used in this analysis, the recoil usually consists of low-energy particles which spray in all directions from the $\overline{p}p$ interaction. The central calorimeters measure the energy flow of these particles over the range $|\eta| < 1.1$. Gas-based sampling electromagnetic and hadronic calorimeters extend this coverage to $|\eta| < 3.6$ [20]. The gains of these devices were set using 50 GeV/c electrons and 50 GeV/c pions in a testbeam. Understanding the response of these devices to the recoil from bosons is problematic for two reasons. First, it depends on difficult details of the flow and energy distributions of these particles. Second, the absolute gains and non-linearities of most of

---

[2] Pseudorapidity (η) is a convenient measure of polar angle at $\overline{p}p$ colliders. It is defined as $\eta \equiv -ln(tan(\theta/2))$, where θ is the polar angle relative to the proton-beam direction.

these calorimeters are not known to great precision. Rather than attempt an understanding of these detectors from "first principles," the energy response to recoil energy is mapped out using $Z \to ee$ events.

2.3 Mass Scale Calibration

The calibration of the mass scale is crucial to the W mass measurement. The basic architecture of the CDF detector is a calorimeter behind a magnetic spectrometer. This configuration allows an *in situ* calibration directly from the collider data. The magnetic spectrometer is calibrated using the $J/\psi \to \mu\mu$ resonance and final alignments are largely accomplished by exploiting the charge independence of the electromagnetic calorimeter measurement. The calorimeter is calibrated by exploiting the linearity and stability of the magnetic spectrometer. A diverse range of physical processes, described in the following section, allows calibration and numerous checks of the calorimeter and magnetic spectrometer mass scales.

2.4 Datasets

In this analysis, six significant datasets are employed. These are described briefly below and in more detail in subsequent chapters. All data are required to come from a "good" run. A run was deemed "good" if no significant problem with the detector, trigger or data-acquisition system was recorded in the shift logbook [21]. A run could be revoked from the good-run list if a problem were found during subsequent analysis. Runs were also required to have more than a 1.806 nb^{-1} exposure. The electron and muon data samples lose 4.9% and 6.8% of the luminosity (initially 20.7 pb^{-1}) to these cuts, respectively. Moreover, requiring that the run not be taken immediately after one of three long collision hall accesses, when the phototube gains were unstable, causes 7.2% of the electron data to be removed. The final dataset corresponded to 18.2 pb^{-1}.

A sample of $\sim 60,000$ $J/\psi \rightarrow \mu\mu$ candidates sets limits on systematic deficiencies of the central tracking chamber (CTC) and determines its absolute momentum scale. These events allow examination of the behavior of the measured mass as a function of geometrical properties of J/ψ production and decay, such as opening polar angle between the muons, the average polar angle of the muons, the region of the magnetic field being sampled, and the transverse momentum of the J/ψ. The variation of the J/ψ mass peak with the transverse momentum of the J/ψ is used to set a limit on the nonlinearity of the device. Ultimately, the measured value of the J/ψ mass peak sets the absolute calibration of the CTC from which all other energy scales in the detector are derived.

A sample of $\sim 140,000$ inclusive central electrons with $E_T > 9$ GeV is used to understand the response up to an overall normalization of the central electromagnetic calorimeter (CEM). These events exploit the uniformity and stability of the CTC to set common gains among the 478 CEM towers, "flatten out" the energy response of the towers, which can vary by 10% near their azimuthal edges, and reduce time dependences. A high-E_T subset of these events, *i.e.*, those with $E_T > 18$ GeV, whose momentum measurement in the CTC is most sensitive to the presence of alignment errors, exploits the charge-independence of the CEM measurement to remove charge-dependent offsets from the CTC calibration.

A sample of ~ 2000 dimuon events near the Υ mass serves as a check on the CTC momentum scale.

A sample starting with 605 dimuon events near the Z mass serves as an additional check of the CTC momentum scale. The width of the Z peak also provides the nominal measure of the CTC resolution.

A sample starting with 28107 $W \rightarrow e\nu$ candidates, with both momentum and energy measurements of the electron, is used to set the absolute scale of the CEM from the CTC. The cuts on electron identification in this W sample are much looser than those imposed on the inclusive electron sample to avoid energy-dependent selection biases. This is the sample used to demonstrate the performance of the calibrated CTC to tracks with low curvature (high p_T) in Section 3.2. These data also serve a check of the CTC and CEM resolutions. The number of these events exhibiting electron bremsstrahlung is used to determine the amount of material inside the tracking volume. A 5718-event subsample (which completely contains the 4425 events used to set the CEM scale) is used to measure the W mass.

A sample starting with 3533 dielectron events near the Z mass is used to map out the response of the calorimetry to boson recoil as described in Chapter 5. The cuts on this sample are kept as close as possible to those which selected the $W \rightarrow e\nu$ sample; this yields a sample of 558 events. A subset of this sample, the 254 events where both electrons are detected by the CEM, measures the CEM resolution and serves as a check of the CEM energy scale normalization.

2.5 Extracting the W Mass

Using these datasets and the final calibrations derived from them, the transverse mass of each W event is constructed. Using the understanding of detector responses extracted from the datasets, a simulation generates the predicted transverse mass spectrum for a range of W masses. The data are compared to simulated transverse mass lineshapes for different masses to extract the measurement of the W mass. The statistical uncertainties are extracted from the fits. To measure the systematic uncertainties, many artificial datasets with an effect varied are generated and fit as the data. The observed mass shifts are used to calculate the systematic uncertainties.

Chapter 3

TRACKING CHAMBER CALIBRATION

The absolute energy scale with which the $W \rightarrow e\nu$ and $Z \rightarrow ee$ mass measurements are made derives from the absolute momentum scale calibration of the central tracking chamber (CTC). This chapter begins with a description of the reconstruction of charged particle momenta and trajectories from their tracks. The following section of this chapter shows the results of the final CTC alignment using electrons, and estimates uncertainties on the W mass from the residual variation after this alignment. In the next section, the absolute scale is set using the position of the $J/\psi \rightarrow \mu\mu$ peak. Next, complementary checks of the scale from a direct measurement of the magnetic field, the mass values of the $\Upsilon \rightarrow \mu\mu$ peaks, and the $Z \rightarrow \mu\mu$ mass are shown. A tracking momentum resolution is returned from the fit to the $Z \rightarrow \mu\mu$ peak and is used later as a check on the tracking resolution extracted from the electron data. The concluding section gives a summary of the systematic uncertainties on the W mass from setting the CTC scale.

3.1 Track Reconstruction

The ionization of gas by the passage of charged particles produces "tracks" in the VTX and CTC detectors. Tracks reconstructed in the $r - z$ view using the VTX determines the location of the interaction point vertex on an event-by-event basis to within 1 mm along the beamline, *i.e.*, in z. The distribution of vertices (shown for the $W \rightarrow e\nu$ sample in Figure 3.1) has an RMS spread of 25-30 cm, depending on the accelerator conditions. Events associated with a vertex more than 60 cm from the center of the detector are rejected to keep only those events for which the projective nature of the detector is used and for which the tracking measurements are best understood. Charged particles with $|\eta| < 1.2$ pass through a ~ 1.4 T axial magnetic field leaving a track in the CTC with curvature in the $r - \phi$ plane inversely proportional to the particle's transverse momentum. The track's trajectory is measured at up to 84 space points from a radius of 30.9 to 132.0 cm from the beamline. These points are fit to the trajectory of a particle described by five helical parameters: $r - \phi$ curvature, $r - \phi$ impact parameter, azimuthal angle, polar angle, and origin of the track along the beamline (in z). In 1986, the field was mapped using a rotating search coil [22] and deviations from a uniform axial field of order 1% were measured. Since during the map the solenoid was run at 5000 A, rather than the 4650 A used during the 1992-93 run, the field measurements were scaled down by the ratio of the currents and corrections of order 1% were made to account for saturation in the steel return yoke. The resultant deviations from an otherwise helical trajectory are included in the fit used to reconstruct the tracks.

The resolution of the track momentum for prompt particles is improved by a factor of two by the subsequent application of a "beam-constraint."

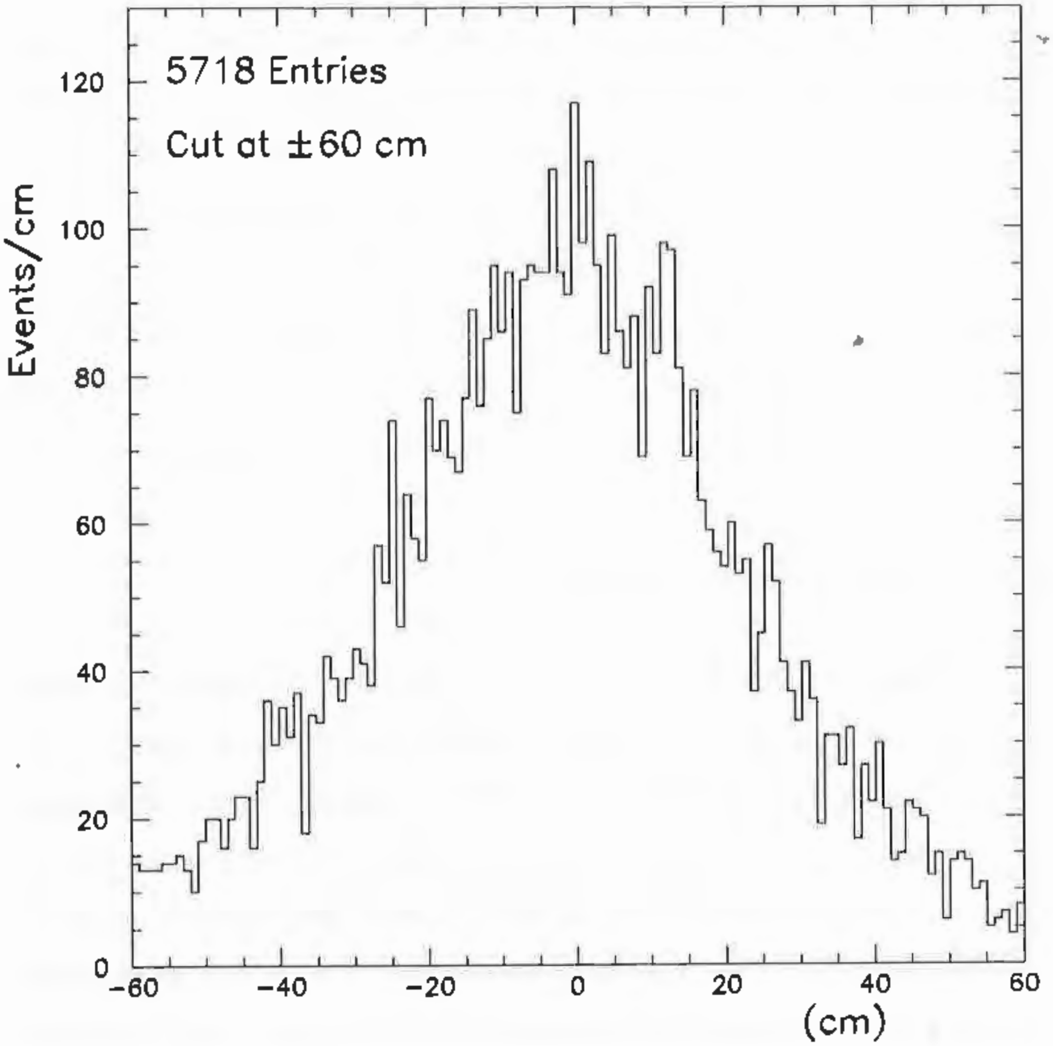

Figure 3.1: Distribution of vertices in the z-direction relative to the center of the CDF detector in the $W \rightarrow e\nu$ sample.

The beam-constraint adds a point to the track by including the interaction point. To accomplish this, the positions and slopes of the beams are measured on a run-by-run basis using the measured origin of inclusive charged particle tracks in the silicon vertex detector (SVX) [23]. These data and the event-vertex position in z as measured by the VTX yield the extra point on the beamline in the $r - \phi$ projection. The beam-constraint of muon tracks includes the effect of ionization energy loss to the $(8.9 \pm 1.3)\%$ X_0 (on average) of material traversed before entering the CTC. (See Section 4.6.) The effect of electron bremsstrahlung is not included in the track reconstruction, but rather is included in the simulation of track reconstruction in Chapter 4.

3.2 False Curvatures

Misalignments of the wires, inadequate nominal drift times in the CTC, and large-scale distortions of the chamber may give rise to false curvatures in the track reconstruction. Since a false curvature is independent of the charge of the particle, it causes a charge-dependent momentum shift between positive and negative tracks. The fractional shift in momentum is largest at small curvatures, *i.e.*, high transverse momentum. Fortunately, these offsets cancel to first-order in mass measurements of the W, Z, J/ψ, and Υ, since the momentum spectra of their daughters are charge-symmetric. The false curvatures must be kept small to control second-order biases on the W mass which may arise from at least two effects: non-linearities arising from the limitations of the charge-averaging of the charge offsets and polar-angle-dependent false curvatures affecting the W mass due to the charge asymmetry in the production and decay of W bosons.

False curvatures are reduced by exploiting the charge-independence of the CEM measurement of the electron energy. Constraining the ratio of the electron energy measured in the CEM to electron momentum measured in the CTC, E/p,[1] to be independent of charge for high-E_T electrons removes most of the false curvatures [24]. A sample of approximately 10,000 inclusive central electrons with $E_T > 18$ GeV, whose curvatures are small enough to be affected, is used for this purpose. The nominal alignments in r, ϕ, and z are adjusted so that there is no splitting in $< E/p >$ between electrons and positrons. A residual modulation of the splitting versus azimuthal angle, ϕ, would worsen the tracking resolution but should not introduce a bias in the scale measurement. A residual modulation in polar angle, θ, would worsen the resolution as well as introduce a scale bias. The scale bias arises from the charge asymmetry of the lepton direction from W decay [25]. A small residual modulation versus ϕ of the track is removed by effectively adding an offset to the nominal beam position. The polar-angle modulation is removed by putting in an effective "twist" of the CTC, or a small counter-rotation of the two CTC endplates. Figure 3.2 shows the difference in the ratio $< E/p >$ for electrons and positrons from the final $W \rightarrow e\nu$ sample before and after the ultimate calibration. This difference is proportional to the false curvature. The residual false curvatures as a function of track ϕ and θ, after all corrections, are shown in Figure 3.3. This sample is not the same as used for the calibration and is the sample used for the mass and scale measurements so these plots serve as a useful check.

The systematic uncertainties due to the presence of false curvatures may be estimated. As stated above, a 2% modulation in the momentum scale as a function of azimuthal angle should not affect the measurement since there are no azimuth-dependent physics biases. The scale bias induced by the false

---

[1] For convenience, the requisite factor of c is dropped in this ratio.

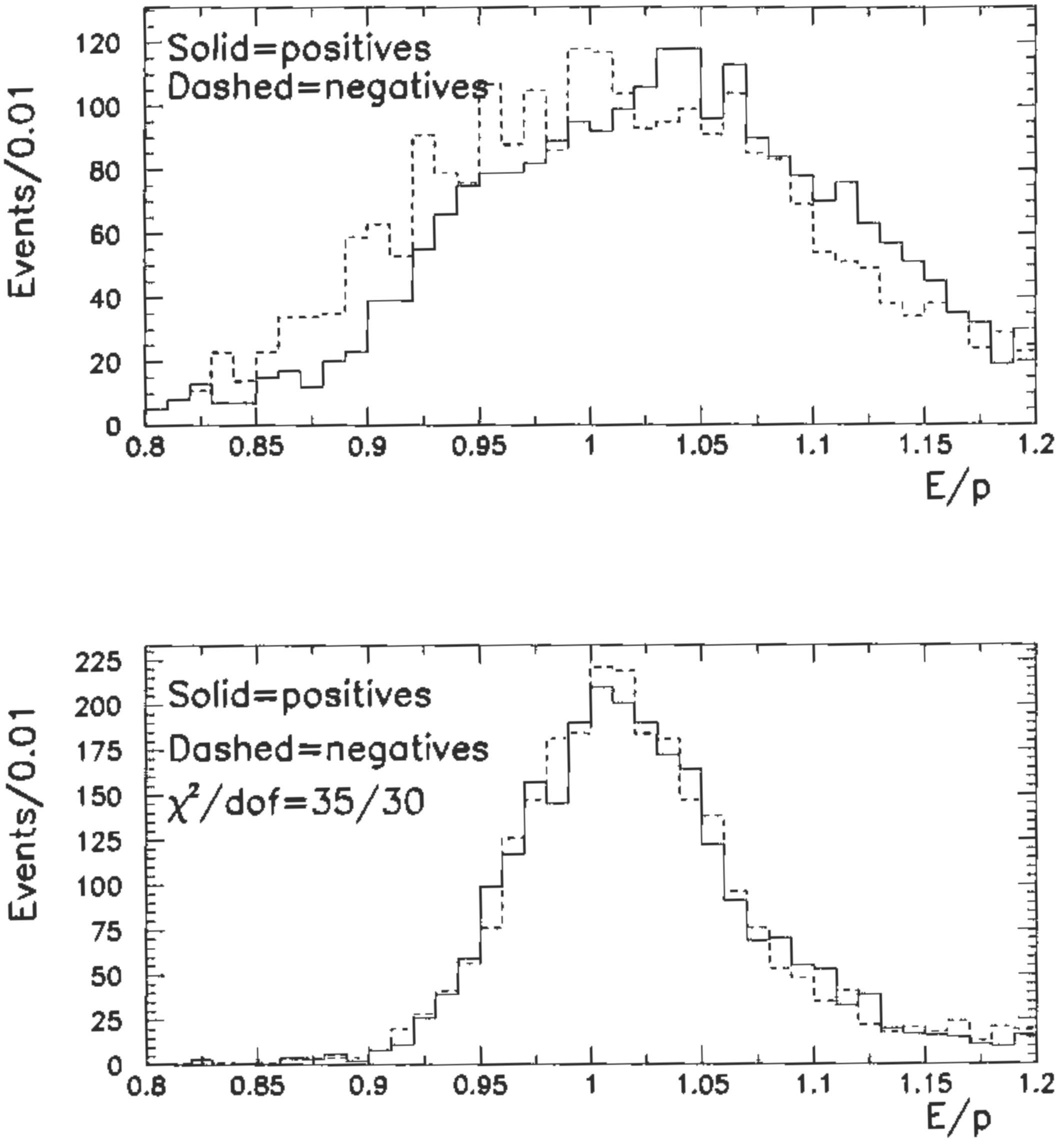

Figure 3.2: Upper: Ratio of E/p for central positrons (solid) and electrons (dashed) with the original CTC calibration in the $W \rightarrow e\nu$ sample. Lower: Same plot after all calibrations and beam constraint.

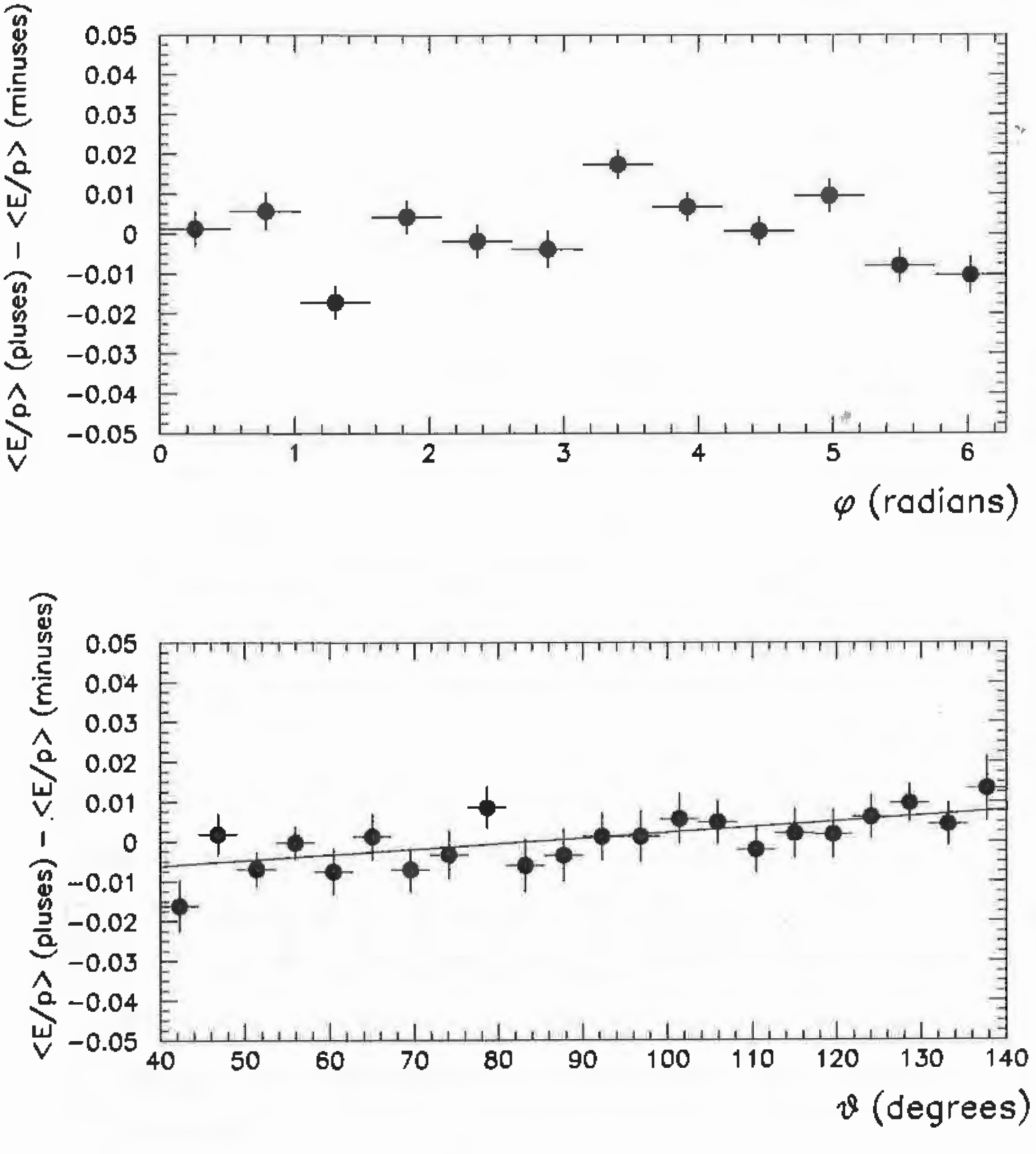

Figure 3.3: Upper: Residual false curvature modulation in CTC as a function of azimuthal angle, ϕ, after all calibrations in the $W \rightarrow e\nu$ sample. Lower: Residual false curvature modulation in CTC as a function of polar angle, θ, after all calibrations. The means of E/p are taken over the range 0.9 to 1.1.

curvature due to a residual 0.5% polar-angle false curvature modulation via the asymmetry of the electron distribution from W decay is studied using the simulation introduced in Chapter 6. The effect contributes a 0.02% scale uncertainty, or 15 MeV/c^2 on the W mass. The possibility of non-linearity in the CTC momentum measurement is addressed in the following section.

3.3 CTC Scale Calibration

The nominal absolute scale of the CTC, from which all other energy scales in the experiment are derived, is determined by normalizing the observed $J/\psi \rightarrow \mu\mu$ peak to the value of 3096.93 MeV/c^2 from the Particle Data Group (PDG) [26]. The sample of 60,000 $J/\psi \rightarrow \mu\mu$ events is shown in Figure 3.4. The procedure is summarized here, but more detail may be found in Reference [27].

A list of systematic uncertainties incurred while normalizing the CTC scale to the J/ψ mass and in extrapolating to the curvatures of W electrons is given in Table 3.1. The entries in the table are now described line-by-line. The data are fit to a Gaussian with a linear background in a 100 MeV/c^2 window centered on the PDG value. The fit determines the mean with a statistical accuracy of 0.1 MeV/c^2. Fits using wider windows yield shifts consistent with that expected from the radiative tail. Each muon is corrected for minimum-ionizing energy loss in material traversed before entering the tracking volume. The amount of material is calculated both from a detailed accounting of all matter installed between the beamline and tracking volume and is also directly measured from the size of the radiative tail of the E/p distribution for W electrons and counting conversions. (See Chapter 4.) The additional material indicated by the measurement is included when reconstructing tracks. Since

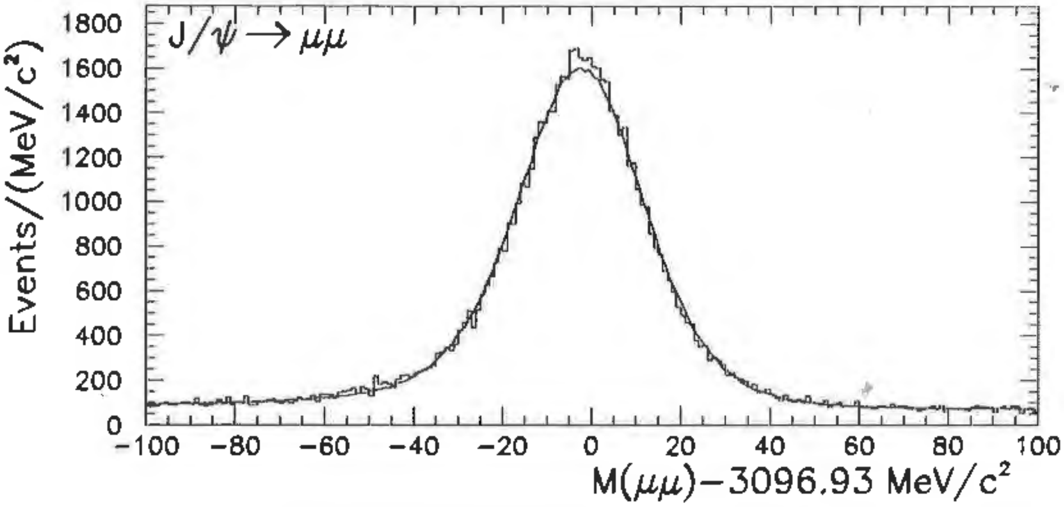

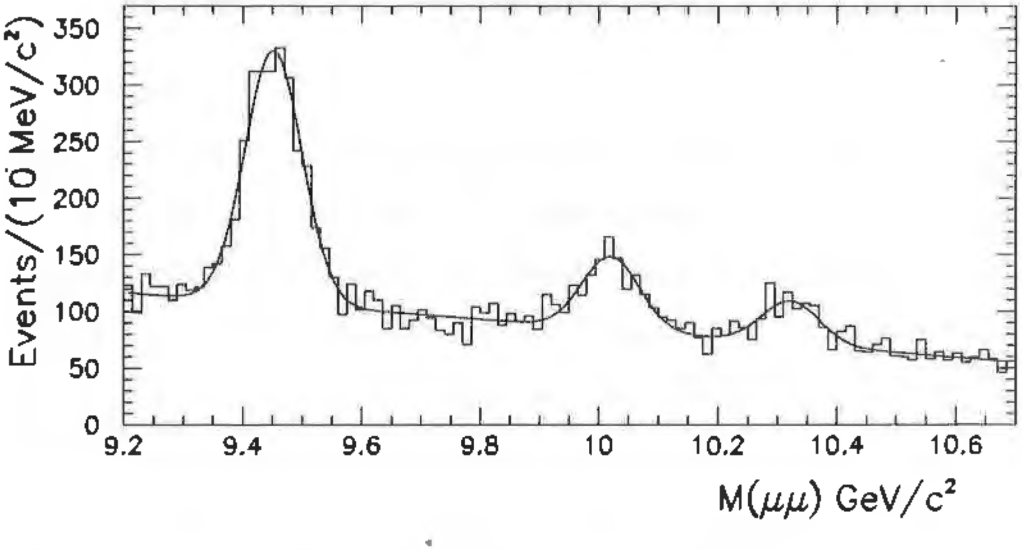

Figure 3.4: Upper: Dimuon mass spectrum near the J/ψ mass. The curve is from a Monte Carlo simulation. Lower: Dimuon mass spectrum near the Υ mass. The fits are Gaussians with a quadratic background.

Effect	Uncertainty (MeV/c^2)
Statistics	0.1
Muon energy loss before tracking	1.1
Beam-constraint	0.3
Opening polar angle effect	0.1
Residual field non-uniformity	0.6
Background	0.1
Time variation	0.5
Radiative decay	0.2
Non-linearity	0.5
PDG	0.1
TOTAL (in quadrature)	1.5

Table 3.1: Uncertainties incurred using the J/ψ peak to set the CTC scale for tracks from W electrons.

a significant fraction of J/ψ mesons come from decays of B mesons which travel some distance from the primary vertex, the J/ψ mass may shift when the beam-constraint is applied. The observed shift, 0.3 MeV/c^2, is taken as a systematic uncertainty. A dependence of the J/ψ mass on the opening polar angle ($\Delta \cot\theta$) between the two tracks is observed. This may be due to an error which causes the polar angle to be mismeasured rather than an error on the curvature measurement, which is all that is relevant for the W mass measurement. To keep the momentum scale determination independent of this polar-angle variation, the momentum scale determination uses J/ψ decays with $\Delta \cot\theta=0$, where the invariant mass is insensitive to polar-angle mismeasurements. To avoid double counting of systematic uncertainties, the variation with opening angle has been removed by reconstructing tracks as if the CTC were compressed by 3 mm from its nominal length of 3214 mm. The adjustment may actually be correcting some other deficiency, such as the tilt in the stereo sense wire angles, rather than the actual length of the chamber.

Although the magnetic field was mapped with high precision in 1986, residual deviations from the map may affect momentum measurements. The residual systematic uncertainty is determined by modeling the variation of the magnetic field as quadratic in z and looking for a linear variation of the J/ψ mass with $< z^2 >$ of the tracks. An uncertainty of 0.6 MeV/c^2 is attributed for this variation. Breaking up the dataset into smaller samples and comparing the mass shifts between using linear and quadratic background shapes suggests that the presence of background contributes less than a 0.1 MeV/c^2 uncertainty. An unexplained 1.0 MeV/c^2 drop in the J/ψ mass is observed over the course of the run. Since the scale is set by the average, the maximum deviation, 0.5 MeV/c^2, is taken as a systematic uncertainty. The shift due to radiative decays of the J/ψ, *i.e.*, $J/\psi \rightarrow \mu\mu\gamma$, is determined from Monte Carlo studies to be -0.44±0.20 MeV/c^2 when fitting a Gaussian plus linear background over the nominal mass range. This correction is applied to the final fit value. The following section sets a limit on CTC non-linearity equivalent of 0.5 MeV from the J/ψ mass when used as the normalization at the W mass. The uncertainty in the PDG J/ψ mass, 0.1 MeV/c^2, is added to the uncertainty.

The final fit value is 3095.1 ± 1.5 MeV/c^2. Thus the CDF momentum scale needs to be shifted up by 1.00056±0.00048 for the J/ψ mass to agree with the PDG value. This correction is applied to set the nominal CTC momentum scale for this analysis. This translates into a correction of $+45 \pm 40$ MeV/c^2 at the W mass.

3.4 CTC linearity

The momentum scale is set using tracks from J/ψ decays, but the scale is used at the W mass. The extrapolation needs to account for possible non-linearities. These may arise from a number of sources including incorrectly-modeled energy loss, correlations with the angular variations, or incorrect CTC alignment causing false curvatures. The first two sources were addressed in the preceding sections. The last source is now discussed in more detail. One can expand the invariant mass formula in terms of track curvatures. By doing so, the largest term not removed by the average over charges is a function of curvature squared, which is plotted in Figure 3.5. The extrapolation to the W mass involves the difference between the average curvature squared of the J/ψ decay products and the average curvature squared of the W decay products. Since the extrapolated shift is small and not entirely understood, it is accounted for by an uncertainty of 0.5 MeV/c^2 with no shift.

3.5 Checks

Three complementary and independent checks are made of the momentum scale. First, the normalization of the J/ψ mass implies a correction of 1.00056 ± 0.00048 to the nominal magnetic field value; this correction has also been measured directly using an NMR probe. Second, the masses of the $\Upsilon \rightarrow \mu\mu$ resonances check the CTC scale using events with pairs of tracks with larger opening angles than the $J/\psi \rightarrow \mu\mu$ events. Third, the mass of the $Z \rightarrow \mu\mu$ resonance checks the scale using curvatures similar to those used in the W mass measurement.

After the 1992-93 run ended, J. Hylen inserted an NMR probe into

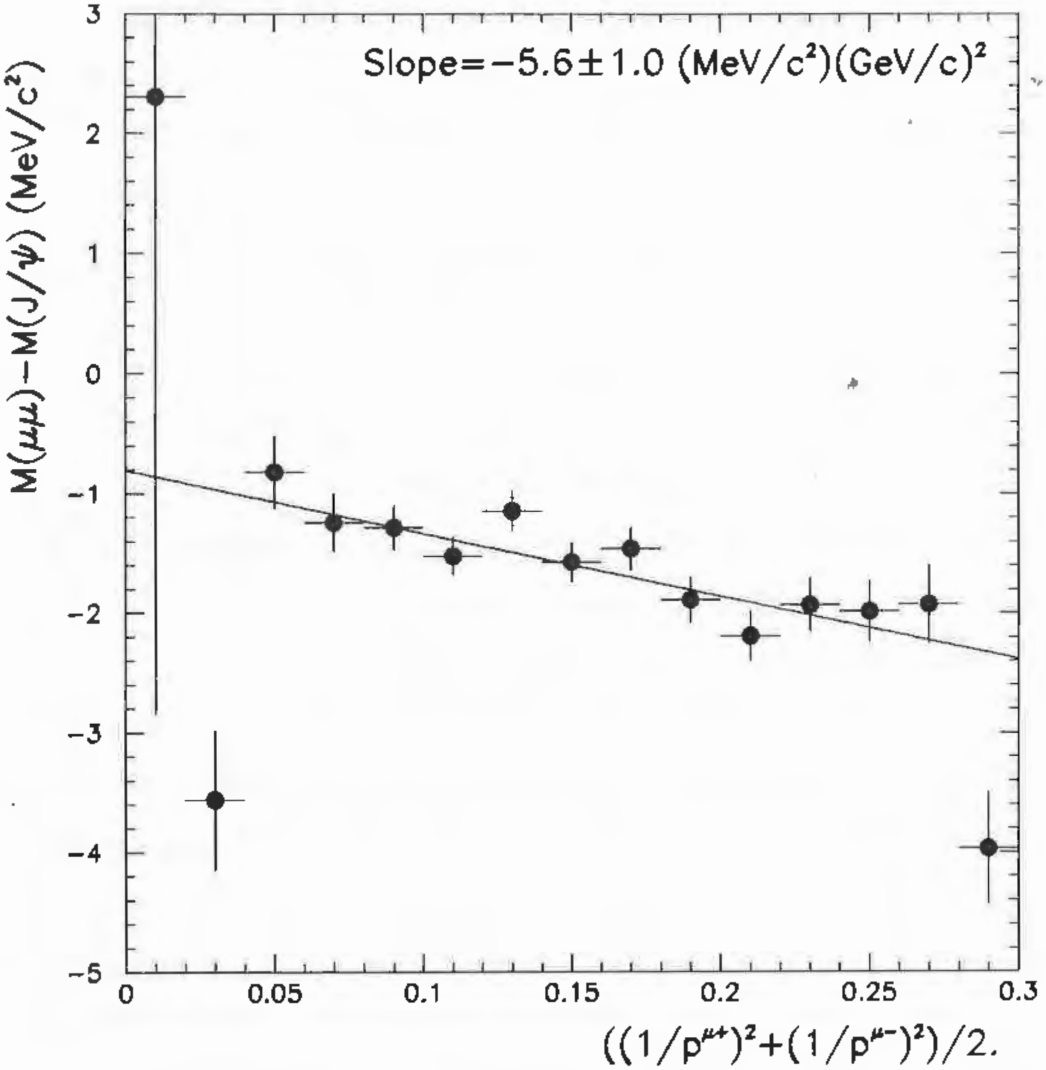

Figure 3.5: Variation of J/ψ mass with average squared curvature. Large curvature means small momentum. The electrons from W decays would lie in the first bin in this plot (0.001 GeV^{-2}c^2). The average for J/ψ decays is 0.10 GeV^{-2}c^2.

the solenoid at a precisely-determined point (r=15 cm, z=150 cm) and used it to measure a precise value of the magnetic field intensity [28]. The value of the magnetic field for that point was predicted using the 1986 magnetic field map and a magnet-saturation correction due to the different operating currents. The measurement indicates that the nominal magnetic field of 1.4116 T should be corrected upwards by a factor of 1.00070 ± 0.00021, in good agreement with the equivalent (nominal) correction implied by the normalization to the $J/\psi \rightarrow \mu\mu$ peak of 1.00056 ± 0.00048. Note that the direct comparison of the normalization of the J/ψ mass and normalization of the magnetic field assumes the nominal locations of CTC wire radii to be correct to a few hundred microns. For example if the radius of the chamber were different, that would mimic a scale shift. Ultimately, the J/ψ peak is used since it does not rely on knowledge of the absolute radii of the CTC wires.

The locations of the three observable Υ resonances: 1S, 2S, and 3S, check the CTC scale using events with pairs of tracks with larger opening angles than the $J/\psi \rightarrow \mu\mu$ events since their masses are larger and do not suffer the same selection bias (trigger p_T threshold). The measured values after the absolute scale calibration are shown in Table 3.2. While the agreement for the 1S and 2S is good, the value for the 3S peak shows a marginally significant difference. However, the 3S peak is sensitive to the background shape, has few events, and it is hard to imagine a real systematic error on the 3S peak which would not affect the 1S and 2S resonances.

The measured mass of the $Z \rightarrow \mu\mu$ resonance checks the CTC using tracks with curvatures comparable to those used to measure the W mass. The measurement is limited by the finite statistics in the peak. The measurement, includes Drell-Yan interference, radiative decays ($Z \rightarrow \mu\mu\gamma$) and the detector resolutions discussed in Chapter 6. The measured value, 91290 ± 190 MeV/c^2

Resonance	Corrected Mass (MeV/c^2)	World-Average Mass (MeV/c^2)
$\Upsilon(1S)$	$9457 \pm 2 \pm 7$	9460.3 ± 0.2
$\Upsilon(2S)$	$10026 \pm 5 \pm 7$	10023.3 ± 0.3
$\Upsilon(3S)$	$10331 \pm 8 \pm 7$	10355.3 ± 0.5
$Z \rightarrow \mu\mu$	$91290 \pm 180 \pm 65$	91187 ± 7

Table 3.2: Measured masses of the $\Upsilon \rightarrow \mu\mu$ and $Z \rightarrow \mu\mu$ resonances compared to the published values. The first uncertainty on the corrected value is from statistics. The second is the systematic uncertainty from setting the momentum scale.

is in good agreement with the precise LEP result of 91187 ± 7 MeV/c^2 shown in Table 3.2. The tracking resolution is fit simultaneously with the scale, yielding a measurement of the tracking resolution at the Z mass of [27]

$$\frac{\delta C}{C} = 0.00084 \pm 0.00008(\text{stat.}) \pm 0.00003(\text{syst.}). \tag{3.1}$$

The contributions to this systematic uncertainty include acceptance, triggering, and fitting.

3.6 Summary

Setting the CTC scale, while crucial to the mass measurement, is robust and does not contribute a large systematic uncertainty. Normalizing the CDF momentum scale to the J/ψ mass causes a systematic uncertainty of 40 MeV/c^2 on the W mass measurement. Several independent checks of the CTC scale are in good agreement. The residual false curvatures as a function of polar angle after their correction add a an uncertainty of 15 MeV/c^2 on the W mass. The tracking curvature resolution ($\Delta C/C$) at the Z mass is measured to be 0.00084 ± 0.00009.

Chapter 4

ELECTRON MEASUREMENT

The CEM measurement of the electron energy dominates the transverse mass measurement, so understanding its scale and resolution is essential. This chapter begins with a description of the central electron reconstruction algorithm. The following section of this chapter describes the calibration of the CEM response, *i.e.,* removing scale dependences on shower position and time, but leaving the overall energy normalization to be determined later in this chapter. The following sections describe the $W \rightarrow e\nu$ and $Z \rightarrow ee$ samples which measure the CEM resolution and set the CEM scale. Before setting the scale, the next section describes how the CEM resolution is extracted from the $Z \rightarrow ee$ data and provides a check using the $W \rightarrow e\nu$ data. In the next section the $W \rightarrow e\nu$ data are used to set the absolute energy scale of the CEM. A measurement of the CEM non-linearity, which affects the Z mass measurement, but not the W mass measurement, is described. The measured mass of the $Z \rightarrow ee$ peak is compared to the precise LEP value as a check of the CEM scale.

4.1 Electron Reconstruction

The electron shower induced in the lead-scintillator sandwich of the CEM produces light in the scintillator. The light is collected from either side of the tower in azimuth and measured by phototubes. The geometric mean of the charge from the two phototubes is used as the measure of tower energy. The geometric mean is used to reduce the gain dependence on local shower position due to light attenuation in the scintillator. To construct clusters of energy, cluster seed towers are chosen from an event as the CEM towers with the largest transverse energy. The two towers on either side in the polar direction ("shoulder towers") are included in the cluster, unless this would require crossing the boundary at $\eta = 0$, in which case the cluster consists of just two towers. Central electromagnetic clusters whose seed tower is one of the outer towers of the CEM are excluded from this analysis. The energy of the electron is taken as the sum of energies from the cluster of seed and shoulder towers. Individual clusters continue to be identified in this way until no towers above the seed tower threshold of 5 GeV remain. For the cluster to be considered a central electron in the $W \rightarrow e\nu$ sample, the ratio of the energy in the hadronic towers behind the CEM towers in the cluster to the total CEM electromagnetic energy must be less than 10%. There also must have been one track with p_T >13 GeV/c in the CTC which extrapolates to the face of one of the CEM towers in the cluster which must have had $E_T > 22$ GeV.

4.2 All-But-Scale CEM Calibration

Variations of the raw CEM response due to scale differences among CEM towers, dependence on shower position within a tower, and time dependence are reduced to improve the CEM resolution. To accomplish this, Larry Nodulman and Karen Byrum have used a sample of inclusive central electrons with $E_T > 9$ GeV which have both their momentum and energy measured independently by the CTC and CEM, respectively [29]. The momentum, p, is measured using the "beam-constraint" described in Section 3.1. These electrons are presumably produced from the semi-leptonic decays of particles containing charm or bottom quarks and from the conversion of photons into electron pairs in the material close to the beamline. The trigger selection and electron identification cuts are similar to the cuts imposed in inclusive electron analyses [30]. An additional cut that $E_T + p_T c > 22$ GeV, away from the trigger thresholds, reduces threshold biases due to backgrounds and fluctuations. A sample of about 140,000 of these electrons are selected with the same fiducial cuts and from the same runs as the electrons in the $W \rightarrow e\nu$ sample. The responses are calibrated iteratively using the mean of E/p in the interval 0.9 to 1.1.

The average gain of each tower is set using the approximately 100-200 of these electrons which hit each tower in each half of the run. Towers without enough inclusive electrons to be calibrated are excluded from the fiducial region for seed towers in the W mass analysis.

The variations in response due to position of the shower within the tower was measured in a testbeam when the calorimeters were much younger, but the high statistics of this sample allows some additional adjusting of the response maps at the 0.5% level using concurrent data. Figures 4.1 and 4.2

show the relative response after all corrections to the CEM for electrons in the final W sample as a function of shower position in the azimuthal and polar directions. In these figures, x_{local} denotes the distance from the center of a calorimeter tower in the azimuthal direction, z denotes the polar distance from the center of the detector along the calorimeter at a depth of 6 X_0, and z_{edge} denotes the distance from the nearest calorimeter edge in the polar direction.

An independent average gain for each tower for the running periods before and after an accelerator shutdown in January 1993 (during which the collision hall was open for several weeks) is determined from the average response of the 100-200 electrons per tower. The CEM energy scale was seen to drop by 4% over the course of the run. The gain variation is reduced by fitting the data to eight independent slopes as a function of run number–before and after the January shutdown for each quadrant of the CEM, which corresponds to separate thermal masses. This change in gain was confirmed by an observable difference in the Cesium-137 source calibrations taken before and after the run [31]. These changes were not uniform and appeared to be correlated with either or both the segmentation of the high-voltage distribution to the phototubes and the thermal mass segmentation [31]. However, the changes were not correlated with either any measured drifts in the high voltage (although these measurements may have been unreliable) and the relevant temperature measurements were deleted online. Figure 4.2 shows the average energy response after all corrections as a function of days since August 26, 1992.

Figure 4.3 shows the total correction factor relative to the online calibration for the electrons in the W sample. The spread of these corrections is small, 3.5%, with no electron receiving a correction larger than 15%.

Since the inclusive electron data have a large fraction of fakes and even the real electrons are produced by processes whose energy flow near the

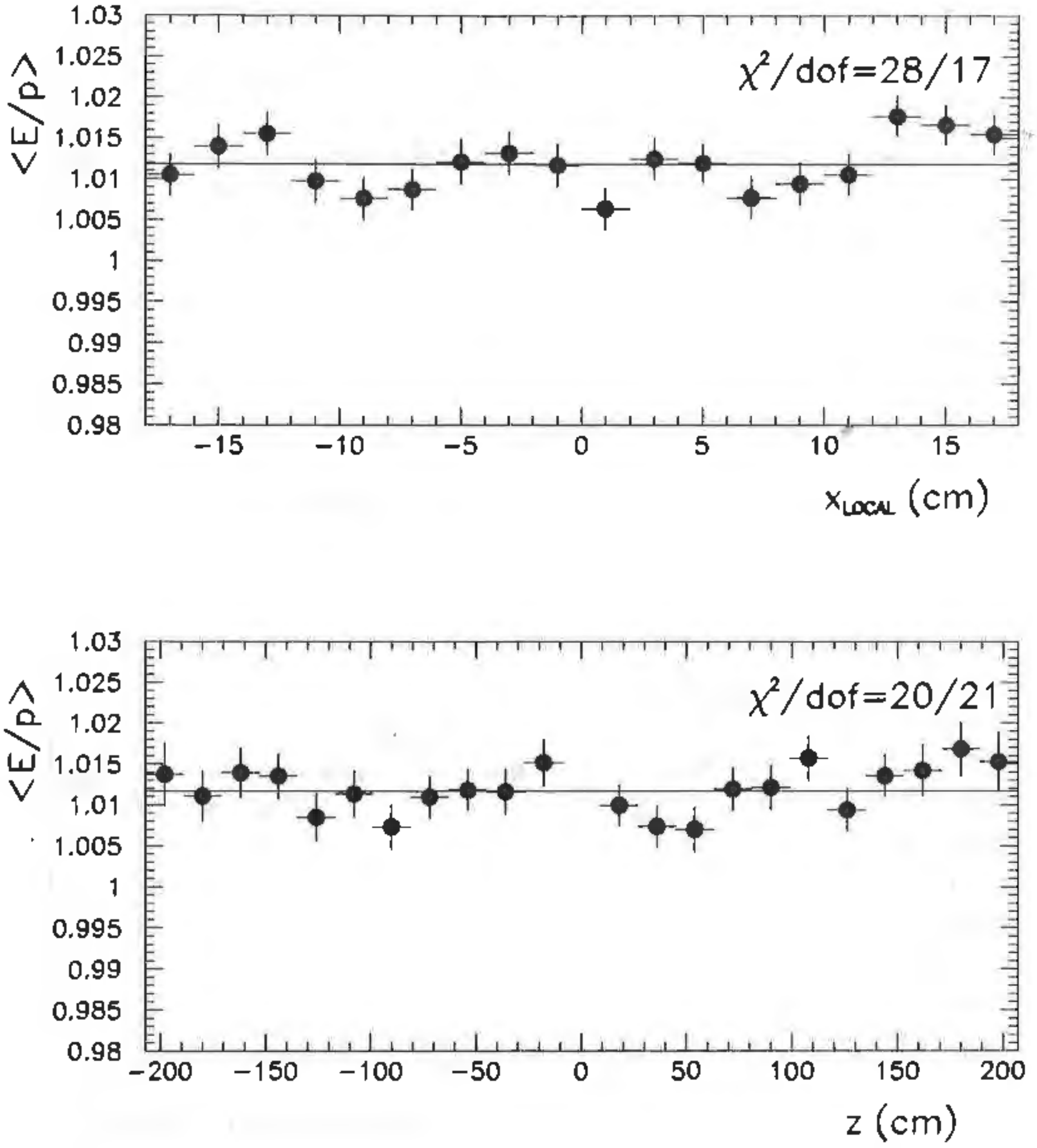

Figure 4.1: Upper: Relative response of the electrons in the W sample as a function of the azimuthal distance in centimeters from the center of the tower. Lower: Same as a function of the polar distance in centimeters from the center of the detector. Energies are after all corrections. The points are the mean of E/p in the range 0.9 to 1.1.

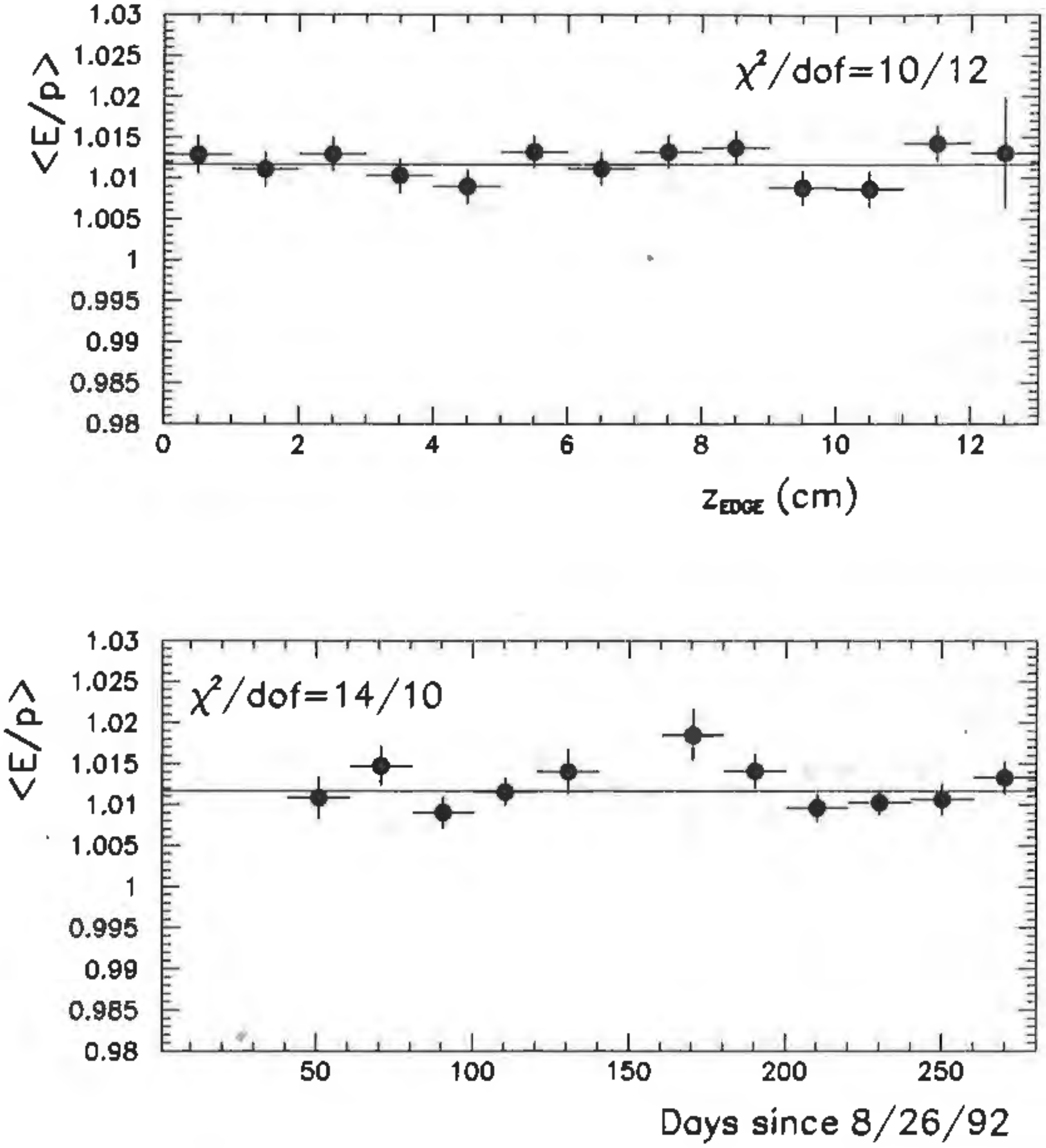

Figure 4.2: Upper: Relative response of the electrons in the W sample as a function of the distance in centimeters to the closest edge in the polar direction. Lower: The relative response as a function of the number of days since August 26, 1992. Energies are after all corrections. The points are the mean of E/p in the range 0.9 to 1.1.

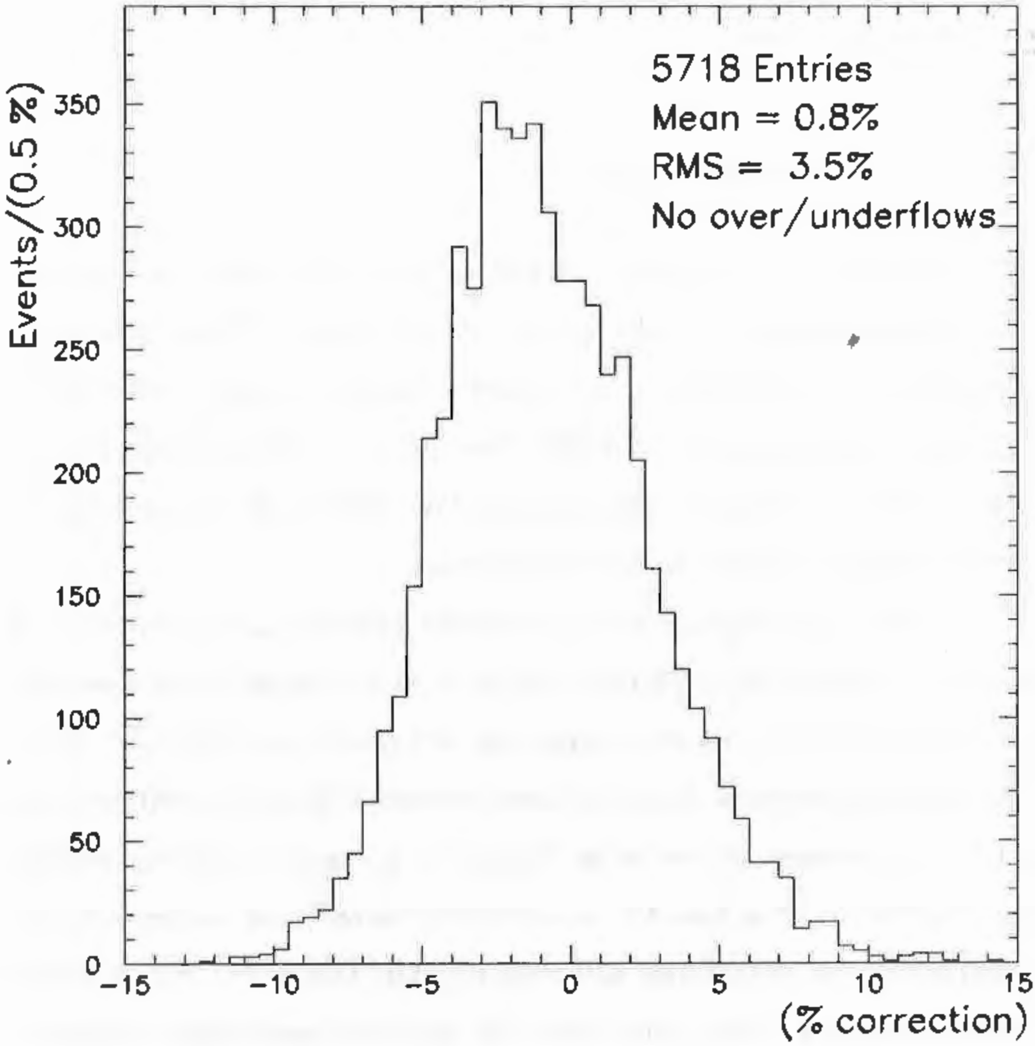

Figure 4.3: Distribution of total correction factors applied to the energies of the electrons in the W sample.

electron is difficult to model, these data cannot be used to set an overall scale for the calorimeter. To that end, electrons from W decay are used as described in the following sections.

4.3 $W \rightarrow e\nu$ Sample

The $W \rightarrow e\nu$ events serve several purposes. They make up the sample of $W \rightarrow e\nu$ events which is used to extract the W mass. These electrons are used in this chapter to transfer the absolute momentum scale of the CTC to the absolute energy scale of the CEM. They serve as a check on the nominal CEM and CTC resolutions. They measure the CEM non-linearity, necessary for extracting the Z mass, but not the W mass.

The sample begins with 28107 events collected using the online calibration with cuts of $E_T^e > 22$ GeV and $p_T^e > 13$ GeV/c on the electron, and $\not{E}_T > 22$ GeV. The cuts applied to make the final sample are listed in Table 4.1. A line-by-line description of each of these cuts now follows: In addition to the good-run requirement described in Chapter 2, a range of runs immediately after each of three long detector accesses are removed since temperature and other conditions in the collision hall were unstable. One and only one electron candidate may be present in the event. The nominal event vertex is chosen as the closest one reconstructed by the VTX to the origin of the electron track and must be within 60 cm in z from the origin of the detector coordinates. The RMS residuals of hits used in the fitted track to the fit must be less than 350 μm. The electron track after the beam-constraint must extrapolate to within 5 cm of the event vertex. The $r-\phi$ impact parameter of the electron track relative to the beamline before the application of the beam constraint must be within 1 cm to remove cosmic rays; this cut is 100% efficient for elec-

Cut	Events Remaining	Luminosity (pb^{-1})
Original sample (see text)	28107	20.7
Good run	26887	19.7
Run not immediately after a long access	24722	18.2
Exactly one electron candidate	23693	
$\lvert z_{\mathrm{vertex}} \rvert < 60$ cm	22425	
RMS Electron track residuals $< 350\ \mu$m	21815	
Electron track can be attached to a vertex	21549	
Electron track impact parameter <1.0 cm	21519	
Electron track beam constr. pull $< 3.0\sigma$	20189	
electron is fiducial	14001	
$E_T^e > 25$ GeV	13025	
$E_T^\nu > 25$ GeV	10739	
$p_T^e > 15$ GeV/c	10399	
$\lvert \mathrm{u} \rvert < 20$ GeV	9072	
No jets with $E_T > 30$ GeV	8961	
No other track with $p_T > 10$ GeV/c	8657	
Track isolation around electron	8067	
Fit region: $65 < M_T^W < 100$ GeV/c^2	5718	
Scale Fit region: $0.9 < E/p < 1.1$	4425	

Table 4.1: Cuts used to make the $W \rightarrow e\nu$ sample.

trons in $Z \rightarrow ee$ events. The electron position in the central detector must pass extremely tight fiducial cuts (5 cm from the azimuthal edge of the towers, 9 cm away from the central crack, and at least as central as the middle of tower 8.) The transverse momentum of the electron track must change by less than three standard deviations when beam-constrained. The electron E_T and neutrino E_T, which is inferred from the total energy imbalance in the detector, are required to be greater than 25 GeV, after all calibrations, to reduce backgrounds while retaining most of the W events. The electron track p_T after all calibrations and beam-constraint must be greater than 15 GeV/c. Note that the energy cuts presuppose knowledge of the CEM energy scale so the event selection and calibration procedure requires one complete iteration. Cuts requiring no events with jets with $E_T > 30$ GeV or recoil $|u| > 20$ GeV reduce background. In addition these cuts yield a sample that is easier to simulate and keep the events with the best resolution on the transverse mass. To reduce the number of $Z \rightarrow ee$ events where the second electron is not identified, no event with another track with momentum greater than 10 GeV/c is allowed. A narrow track-isolation cut around the electron, allowing no tracks with $p_T > 1$ GeV/c within a circle of 0.25 in η-ϕ space, allows background to be reduced without excessively biasing the topology of the event. Note that for the purposes of the stiff-track removal and cone-isolation, the tracks were reconstructed without a beam-constraint. The final W sample contains 8067 events, of which 5718 are in the region $65 < M_T < 100$ GeV/c^2. A subset with $0.9 < E/p < 1.1$, containing 4425 events, are used for determination of the CEM energy scale as described later in this chapter.

4.4 $Z \to ee$ Sample

The $Z \to ee$ sample serves two purposes. The width of the $Z \to ee$ peak measures the CEM resolution. The extracted Z mass serves as a check on the setting of the CEM scale.

The selection of $Z \to ee$ events with one electron detected by the CEM is kept as close as possible to that of the $W \to e\nu$ event selection described above and is detailed in Table 4.2. Most of these cuts are described in the preceding section. If both electrons from the Z hit the central detector, then which electron is considered "first" is determined randomly. Otherwise, the central electron is dubbed "first." The cut on the second-electron E_T uses the E_T that is inferred from the first electron and the underlying event, just at $\not{E}_T$ is calculated for W events, to more closely mimic the resolution for the cut on neutrino transverse energy in the W selection. The event selection yields 254 $Z \to ee$ candidates in the range $81 < M_{\text{inv}}^{ee} < 101$ GeV/c^2, from which the Z mass is extracted. There are no like-sign events in the 254-event central-central sample.

4.5 CEM Resolution

The width of the $Z \to ee$ peak is used to measure the CEM resolution. The CEM resolution is parameterized by

$$(\frac{\delta E}{E})^2 = (\frac{(13.5 \pm 0.7)\%}{\sqrt{E_T}})^2 + \kappa^2, \tag{4.1}$$

where the first term is an irreducible stochastic term measured with a 50 GeV/c electron testbeam [17]. (Note that accounting for scintillator deterioration, a more accurate number might be $(13.7 \pm 0.7)\%$ which is close enough as to

Cut	Events Remaining	Luminosity (pb^{-1})
Original sample (see text)	3533	20.7
Good run	3366	19.7
Run not immediately after a long access	3114	18.2
Exactly two central electron candidates	2536	
$\|z_{\text{vertex}}\| < 60$ cm	2423	
<First electron track residuals> < 350 μm	2380	
First electron track can be attached to a vertex	2362	
First electron track impact parameter <1.0 cm	2362	
First electron track beam constr. pull < 3.0σ	2245	
First electron fiducial	1555	
Second electron fiducial	1242	
First $E_T^e > 25$ GeV	1122	
Second $E_T^e > 25$ (effective) GeV	1040	
First $p_T^e > 15$ GeV/c	993	
Second $p_T^e > 15$ GeV/c (if central)	990	
$\|u\| < 20$ GeV	859	
No jets with $E_T > 30$ GeV	853	
No extra track with $p_T > 10$ GeV/c	677	
Track isolation around first electron	623	
Track isolation around second electron	607	
$81 < M^{ee} < 101$ GeV/c^2	544	
Central-Central	254	
Central-Plug	239	
Central-Forward	51	

Table 4.2: Cuts used to make the $Z \rightarrow ee$ sample.

make no difference.) In the second term, κ reflects residual gain variations not removed by the calibration procedure. For example, the finite number (100-200) of electrons used to set the tower-by-tower gain would cause a 0.8% constant term. Imperfections in the time-dependent or position-dependent calibration, or a slight difference from the 13.5% in the stochastic term would be absorbed into the constant term.

The constant term is extracted from the observed width of the $Z \rightarrow ee$ peak. The main contributions to this width are the intrinsic width of the Z, 2.489 GeV [32], radiative decays ($Z \rightarrow ee\gamma$), and the smearing due to CEM resolution. The fractional RMS of the peak in the interval $81 < M_{ee} < 101$ GeV/c^2 is $(3.48\pm0.18)\%$. Lineshapes of $Z \rightarrow ee$ including the above effects and an event simnlation similar to that used for the W events in Chapter 6 are generated for different assumed constant terms. Comparing to the data indicates that the best constant term to use in Equation 4.1 is

$$\kappa = (1.2^{+0.9}_{-1.2})\%. \tag{4.2}$$

A consistency check may be made by examining the width of the spectrum of the ratio of E/p for the electrons in the $W \rightarrow e\nu$ sample. The main contributions to the width of the E/p peak are the CEM energy resolution, the momentum CTC resolution and the spreading due to bremsstrahlung by the electrons. The sigma/mean of the E/p peak fit to a Gaussian over the interval $0.9 < E/p < 1.1$ is $(4.30 \pm 0.05)\%$. Removing the spreading due to bremsstrahlung, the sigma/mean is $(4.03 \pm 0.05)\%$. Using Equations 3.1 and 4.1 and that the $< E_T^e >$ of these electrons is 38.2 GeV indicates that the constant term is $(1.1^{+1.1}_{-1.1})\%$, which agrees extremely well with the number obtained from the $Z \rightarrow ee$ data. Note that this method is only used as a check, since it treats all electrons as if of the same transverse energy. Also, it is possible that there are unknown systematic errors which cancel when taking the ratio of electron energy to momentum, E/p, so the extracted constant term would be erroneously low.

One can also estimate the value of the constant term from "first principles." Since only 100-200 inclusive electrons were available to set the gain in each tower for each half of the run and the RMS of E/p for the inclusive electrons is 9%, the constant term should be at least 0.8%, or slightly larger due to imperfections in the calibration procedure, such as the mapping, time dependence and polar-angle dependence of leakage.

Thus the number used for the constant term by using the width of the $Z \rightarrow ee$ peak is in good agreement with the central value obtained from the estimate using the widths of the E/p distribution and the $Z \rightarrow \mu\mu$ peak as well as with a direct estimate from the calibration procedure.

4.6 CEM Scale Calibration

To determine the CEM energy scale using these data, a thorough understanding of the electron E and p measurements up to the arbitrary normalization for E is necessary. The ratio of electron energy to momentum, E/p, for electrons in the W sample is shown in Figures 4.5 through 4.7. The long tail on the high side of the distribution is due to bremsstrahlung from the electron. The electron may lose energy to photons either as it is created from the W decay (internal bremsstrahlung) or as it passes through the $(8.9 \pm 1.1)\%\ X_0$ (on average) of material before entering the CTC (external bremsstrahlung). Since the associated photons are usually collinear with the electron, they often hit the same calorimeter tower as the electron so that the CEM response is relatively unaffected by the bremsstrahlung process. In either case, the electron momentum, p, is lower than the calorimeter measurement, E, producing the long tail in E/p.

The modeling of the E/p spectrum uses the same production mechanism and modeling of the measurement of the recoil as the W simulation described in Chapters 5 and 6. This radiative simulation also includes the contribution from the three-body W decay matrix element for $W \rightarrow e\nu\gamma$ calculated by Berends and Kleiss [33] and implemented by R. G. Wagner [34]. The simulated electrons and photons are stepped through the inner material where the processes of electron bremsstrahlung and photon conversion as described by Tsai [35] are included. The electron and its associated photons are propagated to the calorimeter where the formation of electromagnetic clusters is simulated.

The simulation of the shape of the E/p distribution requires knowledge of the amount of material traversed by the electrons before entering the CTC, since the low-energy bremsstrahlung shifts the peak of E/p. The material was tabulated from a direct accounting of all matter installed between the colliding beams and the CTC [36]. The material traversed by every electron in the W sample from its origin to the middle of the CTC is extracted from this database and is predicted to have a mean of 6.4% X_0 as shown in Figure 4.4. Since the W data themselves are used to extract the material, the average radiation length is scaled up by a small amount, 0.4%, to correct for a selection bias against going through larger amounts of material incurred by the electron p_T cut. The amount of material used in the simulation is measured from the size of the E/p tail relative to the peak which effectively counts the number of hard bremsstrahlung events. The value of

$$\frac{\text{number of events with } 1.3 < E/p < 2.0}{\text{number of events with } 0.8 < E/p < 1.2} \tag{4.3}$$

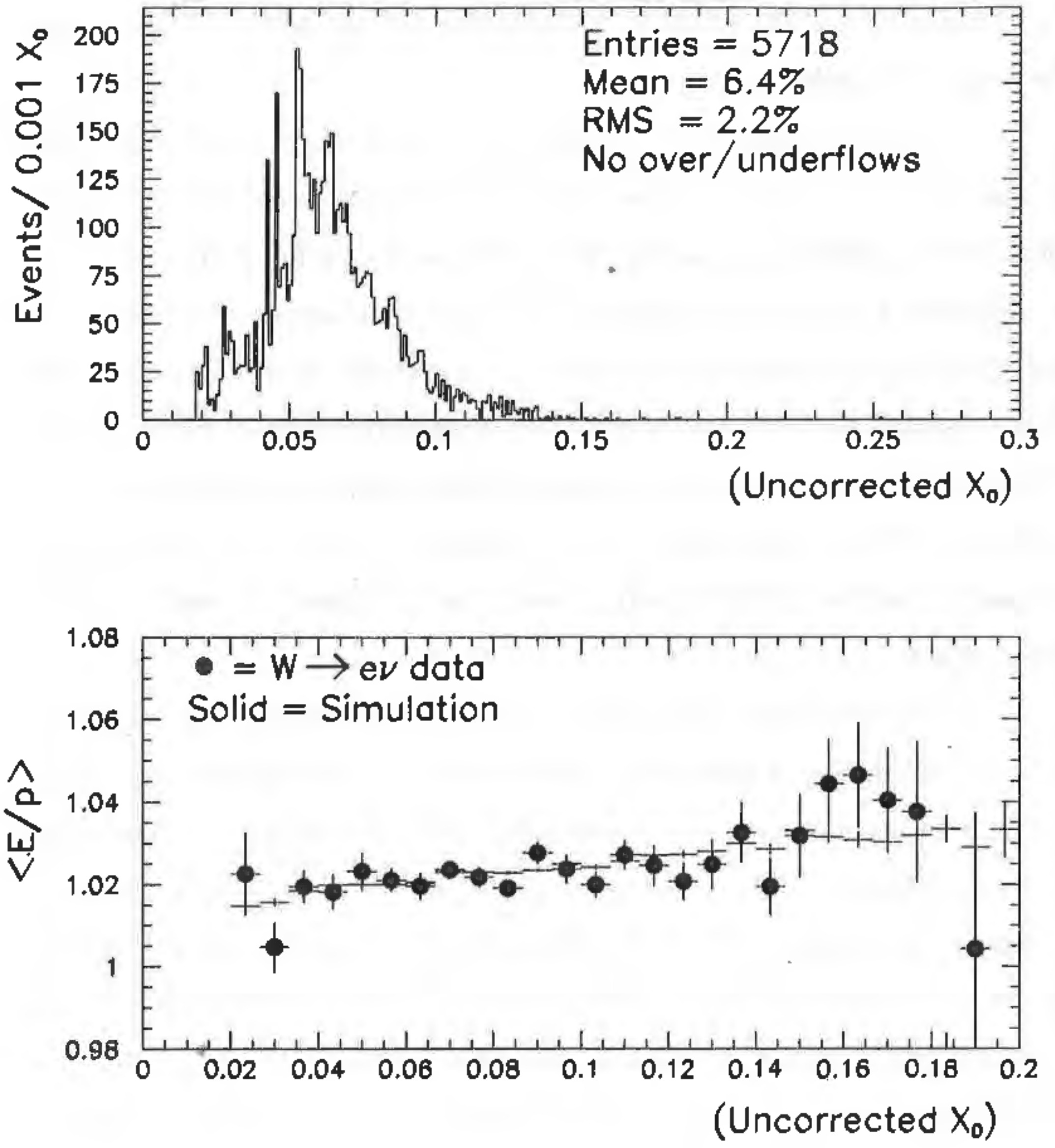

Figure 4.4: Upper: Amount of material traversed by each electron in the W sample up to the middle of the tracking volume as predicted by the direct accounting. Lower: Variation of $< E/p >$ in the data and simulation after scaling material. The mean of $< E/p >$ is taken in the interval from 0.8 to 1.2 for this plot since this window makes the mean more sensitive to the amount of bremsstrahlung.

Effect	Uncertainty (on ξ)	Uncertainty ($\% X_0$)
Statistics	0.10	0.6
Backgrounds	0.03	0.2
Resolution	0.09	0.6
Window definitions	0.10	0.6
Total Uncertainty	0.17	1.1%

Table 4.3: Uncertainties in measuring the amount of material inside the tracking volume. The scale factor, ξ, is a factor multiplying the material extracted from the database.

is measured to be 470/4686. For the simulation to reproduce this tail, the accounting of the material must be increased by a scale factor, ξ, of 1.40 ± 0.17. The sources of the uncertainty on this number are summarized in Table 4.3. The 0.10 (0.6% X_0) statistical uncertainty is due to the finite number of events in the tail. A 0.03 (0.3% X_0) uncertainty is a conservative limit on the effect of backgrounds in the sample, which is measured by adding cuts on the $r - z$ shower profile shape and matching to the electron track. The shift is consistent with half the non-electron background (estimated in Chapter 7) lying in the tail of E/p. The 0.09 (0.6% X_0) uncertainty due to "resolutions" is the variation seen on the material estimation from varying the resolutions coherently within their 1σ bounds. An additional uncertainty of 0.10 (0.6% X_0) is taken to account for variations as the window definitions for the "peak" and "tail" are changed. This is comparable to the statistical uncertainty and is probably double counting, but is taken to be conservative. (Note that this is not the same as the uncertainty taken later on the energy scale for "fitting" where the window for the fit is varied.) For estimating systematic uncertainties on the scale from the material, the uncertainty on ξ is taken as 0.17. Thus, the average amount of material traversed by electrons from W decay before entering the tracking volume is $(8.9 \pm 1.1)\%\ X_0$, compared to the result from direct accounting of 6.4% X_0. An additional uncertainty of order 0.7% X_0 should be included in this comparison corresponding to not knowing at what radius in the CTC to stop counting material; this uncertainty does not apply to the amount of material used in the simulation since it is measured using the tail of the E/p distribution. This discrepancy was of some concern, but subsequent studies of the amount of material using photon conversions are all in agreement with the measured amount of material using the tail of E/p and inconsistent with the number from the direct accounting [37].

The factor ξ appears independent of the electron's azimuthal or polar location, vertex position, time, and location of shower in local CEM tower coordinates. The relative distribution of material is seen to be essentially correct by comparing the value of $< E/p >$ versus the amount of material supposedly traversed by the electron in the data to that of the simulation, as shown in Figure 4.4. Note that even if the material distribution in Figure 4.4 had been replaced by a single-valued function with the same mean, the fitted energy scale and calculated amount of material would have changed only negligibly.

One may also look for anomalous behaviour of the required amount of material for different ranges of electron E_T. A significant disagreement could indicate a problem with inadequate modelling of the electron E_T spectrum, the bremsstrahlung process, the p_T cut, the energy dependence of the resolutions or an unexpected energy dependence of the electron identification criteria. As shown in Table 4.6, the simulation predicts a slight rise in the number of events in the tail relative to the peak as electron E_T increases, mostly due to the p_T cut. There is no statistically significant pattern of disagreement in the data.

The simulation produces lineshapes of the E/p spectrum between

Range (MeV)	tail/peak	ratio (data) (%)	ratio (simulation) (%)
$25 \leq E_T < 30$	9/88	10.2 ± 3.4	10.3 ± 0.8
$30 \leq E_T < 35$	119/1057	11.3 ± 1.0	9.8 ± 0.2
$35 \leq E_T < 40$	226/2275	9.9 ± 0.7	10.1 ± 0.2
$40 \leq E_T < 45$	99/1184	8.4 ± 0.8	10.4 ± 0.2
$45 \leq E_T < 50$	32/249	12.9 ± 2.3	11.1 ± 0.5
$50 \leq E_T < 55$	9/69	13.0 ± 4.3	12.1 ± 1.2

Table 4.4: Energy dependence of the size of the "tail" of the E/p spectrum relative to its peak.

0.9 and 1.1 for a range of effective CEM scales and tracking resolutions. The mechanics of this fitter are the same as the W transverse mass fitter with the W mass and width left floating, described in detail in Chapter 8. The CEM scale is set so that the result of the fit to the reconstructed data is the nominal CEM scale. The best-fit tracking curvature resolution floats to

$$\frac{\delta C}{C} = 0.00079 \pm 0.00002 \text{ (stat.)} \pm 0.00012 \text{ (syst.)}, \tag{4.4}$$

which agrees well with that obtained from the observed width of the $Z \rightarrow \mu\mu$ peak of 0.00084 ± 0.00009. (See Equation 3.1.) The sources of the systematic uncertainties are 0.00002 from the uncertainty on the material scaling factor, ξ, 0.00010 from the electron resolution, and 0.00006 from doubling the size of the fit region to $0.8 < E/p < 1.2$. This confirms that the measured CEM and CTC resolutions are either adequate or that they are wrong in such a way as to exactly compensate in the ratio. The best fit for the E/p spectrum is shown for various ranges and types of scale in Figures 4.5 to 4.7. The poor agreement in the tail of E/p in Figure 4.7 may be due to the effect of the missing material distribution on the electron p_T cut. A range of windows for

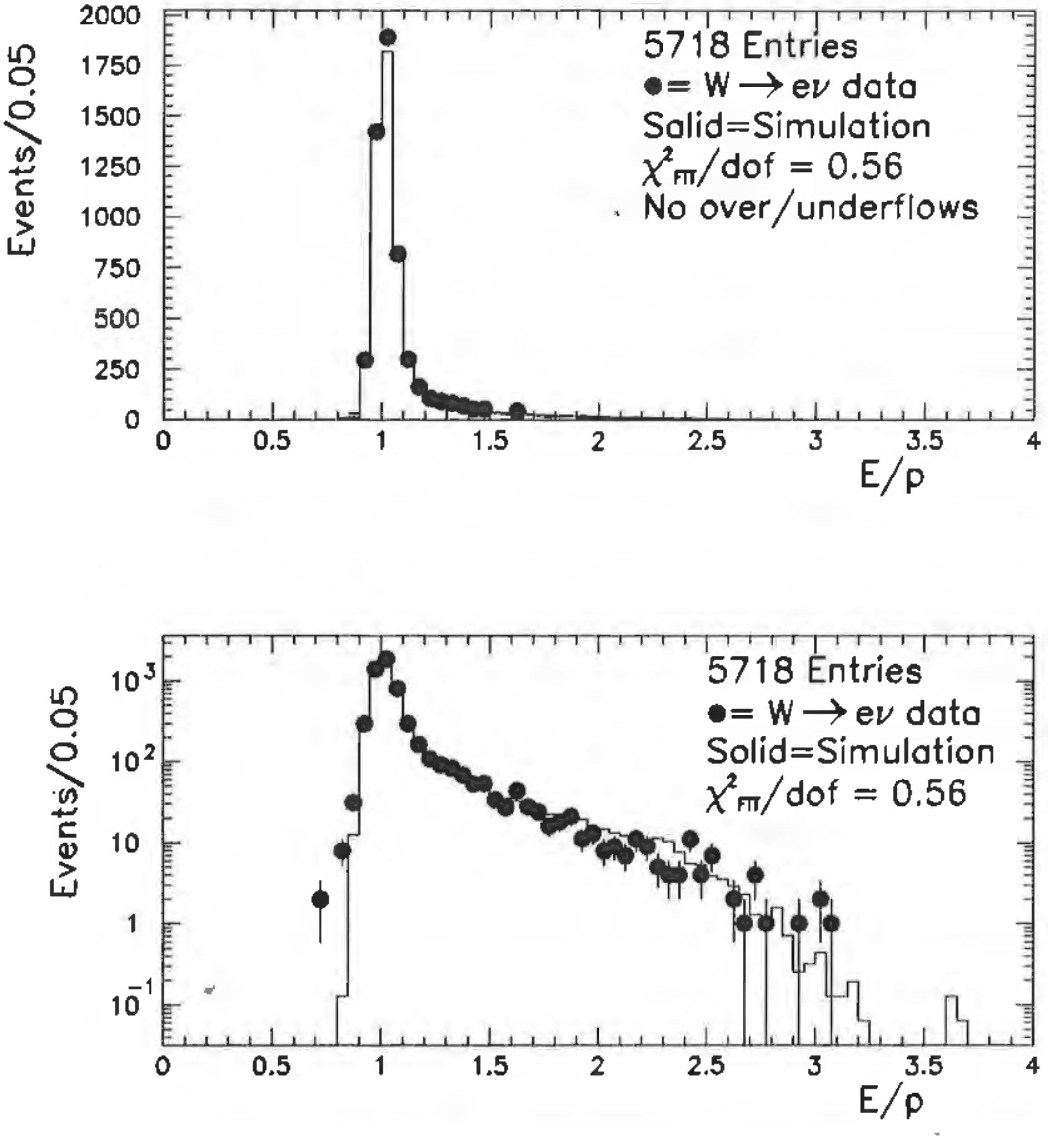

Figure 4.5: Upper: E/p for electrons in the W sample on a linear scale. Lower: Logarithmic scale. The points are the electron data and the histogram is the best-fit simulation.

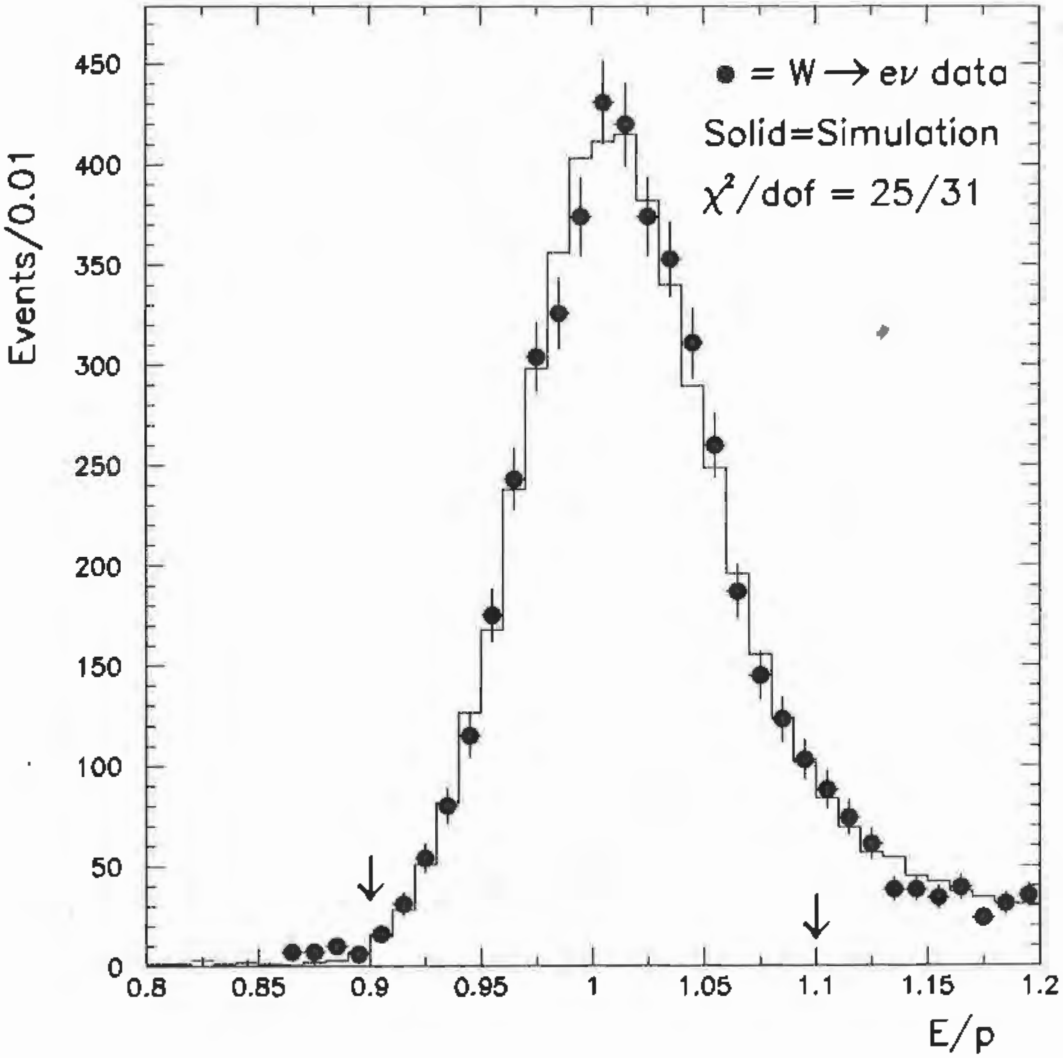

Figure 4.6: Peak of E/p for electrons in the W sample. The points are the electron data and the histogram is the best-fit simulation.

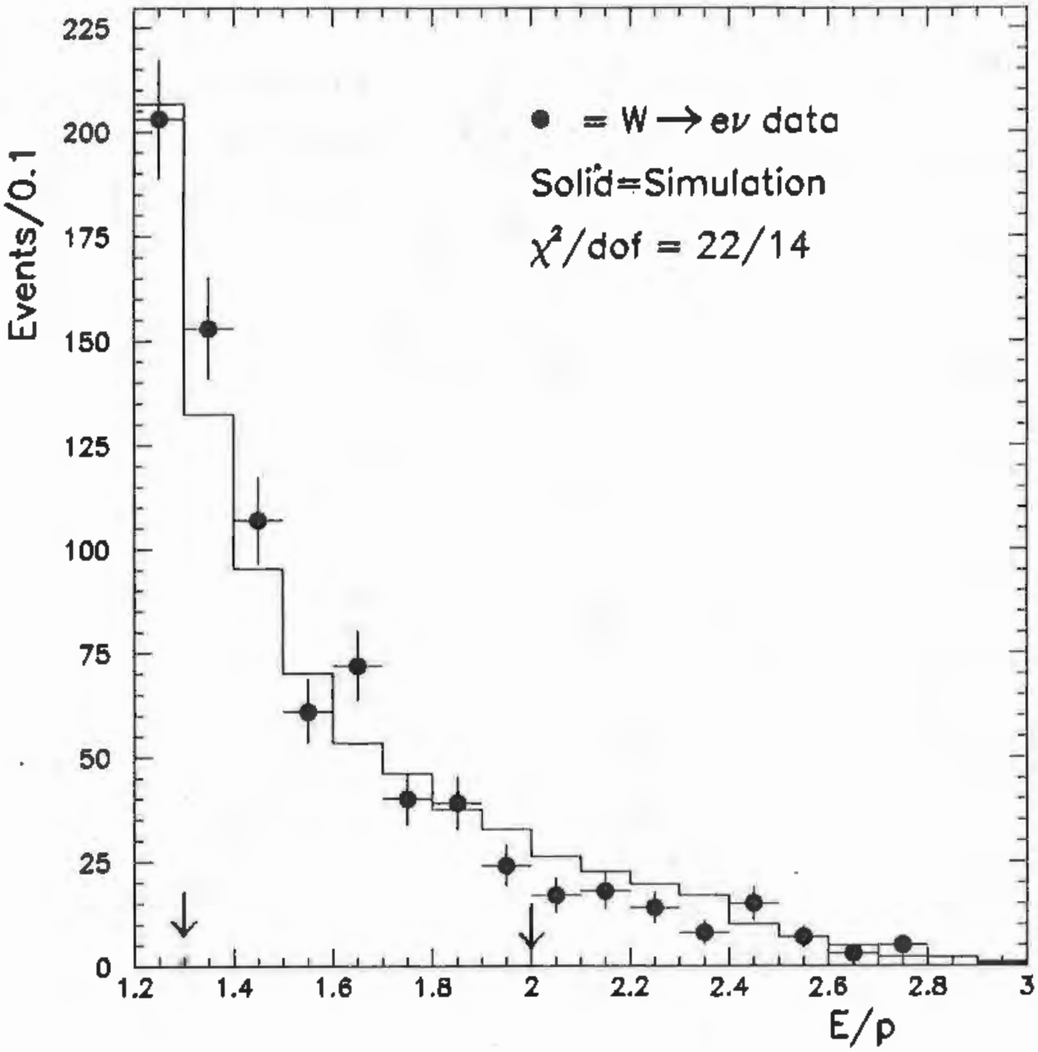

Figure 4.7: Tail of E/p for electrons in the W sample. The points are the electron data and the histogram is the best-fit simulation.

Material Scale (ξ)	Energy Scale (%)	Track Resolution (%)	
1.00	99.80 ± 0.01	0.0773	
1.20	99.91 ± 0.01	0.0793	
1.40	100.01 ± 0.01	0.0803	nominal
1.60	100.10 ± 0.01	0.0815	
1.80	100.16 ± 0.01	0.0820	

Table 4.5: Variation of the fitted energy scale and track resolution as the material scaling factor is changed from the simulation. The nominal energy scale for this study was 100.00% with a track resolution of 0.08%.

the tail are used and the variation, although marginally statistically significant (2 σ), is taken as a systematic uncertainty on the material determination.

The contributions of systematic uncertainties on the amount of material, the electron resolution, and other effects on the CEM scale uncertainty and estimated CTC resolution are investigated by fitting artificial data, with an an effect modified, to the nominal lineshape and recording the shift. The results of this study for the amount of material are shown in Table 4.5. Taking the 0.17 uncertainty on the scaling factor, ξ, (1.1% X_0), an uncertainty on the energy scale of 0.09% is measured. A similar study for the constant term parametrizing the electron resolution is summarized in Table 4.6 and seen to contribute a 0.08% uncertainty on the CEM scale. Since the smearing of E/p accomplished by the tracking and electron resolutions does not have the same functional form, the fractional RMS is not expected to be a constant. Note that the fractional RMS (in the interval $0.9 < E/p < 1.1$) in the data, $(4.00 \pm 0.04)\%$, agrees remarkably well with the prediction of $(4.01 \pm 0.01)\%$, showing that the resolution functions are appropriate. This data point compared to Table 4.6 shows that the uncertainty taken on the constant term is

Constant Term (%)	Energy Scale (%)	Track Resolution (%)	RMS (%)	
0.2	99.94 ± 0.01	0.072	3.75 ± 0.02	
0.7	99.95 ± 0.01	0.075	3.88 ± 0.02	
1.2	99.99 ± 0.01	0.079	4.01 ± 0.01	nominal
1.7	100.02 ± 0.01	0.085	4.14 ± 0.02	
2.2	100.03 ± 0.01	0.091	4.39 ± 0.02	
2.7	100.10 ± 0.01	0.098	4.60 ± 0.02	

Table 4.6: Variation of the fitted energy scale and track resolution as the constant term parameterizing the electron resolution is changed from the value in the simulation. The fractional RMS of E/p in the fit range is shown for the listed set of parameters. The nominal energy scale was 100.00% with a track resolution of 0.08%.

Effect	Uncertainty (%)	ΔM_W (MeV/c^2)
Statistics in E/p peak	0.08	65
Material	0.08	65
Electron resolution	0.08	65
Backgrounds	0.04	30
Fitting	0.06	50
Total	0.16	125

Table 4.7: Uncertainties in setting the CEM energy scale from the CTC momentum scale.

conservative. A 0.06% shift is seen as the fit window is doubled; this is conservatively taken as an additional systematic uncertainty due to fitting. Table 4.7 summarizes the systematic uncertainties in setting the CEM scale estimated in this section and Chapter 3. The uncertainties due to deriving the CEM energy scale from the CTC momentum scale are 65 MeV/c^2 from the finite statistics in the E/p peak, 60 MeV/c^2 from the material measurement, 65 MeV/c^2 from the electron resolution, 30 MeV/c^2 which is the shift from the backgrounds other than $W \rightarrow \tau\nu \rightarrow e\nu\nu\nu$ (See Chapter 7.), and 50 MeV/c^2 from the shift due to doubling the size of the fit window. Including the uncertainties on the absolute momentum of the CTC, the total scale uncertainty is 130 MeV/c^2 (150 MeV/c^2 at the Z mass).

4.7 CEM Non-Linearity

The following section describes a check of the CEM scale calibration using a measurement of the $Z \rightarrow ee$ mass. The non-linearity is defined as the change in the CEM calibration as the $< E_T >$ of the electrons increases. One must measure CEM non-linearity only for using the measurement of the Z mass as a check. Since the calibration was made with W electrons, and the electrons from Z events have larger average transverse energies, a non-linearity would affect the Z mass measurement. Since the E/p measurement strongly correlates with the E_T measurement, on cannot just plot $< E/p >$ versus E_T. The CEM non-linearity is measured by comparing the E/p ratio as a function of electron E_T in $W \rightarrow e\nu$ data to the simulation which includes the best knowledge of the resolutions on E, p, and the E_T spectrum of the electrons. Because the CEM response is assumed to be linear in the simulation, an E_T dependence in the residuals of the data and simulation is a measurement of the CEM non-linearity.

The radiative simulation is employed to search for a non-linearity in the CEM energy response. Unlike the variation of the CEM response with respect to energy-independent variables such as shower position, the response with respect to energy will be biased by the resolutions. However, since the detector resolutions are included in the radiative simulation, the difference between the energy responses with respect to electron transverse energy in the data and simulation reflects the non-linearity. Figure 4.8 shows the strong dependence of E/p on electron E_T both in the data and simulation where the mean has been taken over the interval $0.9 < E/p < 1.1$. The residuals, obtained by dividing the two curves and subtracting 1.0, are also shown fit to a line. This correction is not applied to the W data since the energy scale derives from the same events as used to fit the W mass. However, the correction is applied to the fitted Z mass which is measured as a check on the energy normalization. In the W calibration data, $< E_T^e >$=38.2 GeV and in the $Z \rightarrow ee$ data, $< \sqrt{E_T^{e1} E_T^{e2}} >$=42.8 GeV. The slope of the residuals in Figure 4.8 is $(0.00050 \pm 0.00022 \pm 0.00043)$ GeV^{-1}, where the first uncertainty is statistical and the second results from varying the resolutions within their 1σ bounds.

Thus the Z mass measured in the following subsection is corrected for a non-linearity of the CEM energy response by -210 ± 200 MeV/c^2. The difference between $< E_T^e >$ in the E/p fit region and the $< E_T^e >$ for the entire W mass fitting sample is 0.12 GeV, so the contribution of CEM non-linearity on the W mass measurement is smaller than 5 MeV/c^2.

4.8 $Z \rightarrow ee$ Mass

The data are fit to lineshapes made at different Z masses using the same fitting machinery used to fit the E/p peak and also used to fit the transverse mass spectrum in Chapter 8, where it is fully described. The fit range is dielectron masses between 81 and 101 GeV/c^2. The modeling of the production and measurement of Z bosons is similar to that for W bosons described in Chapter 6. The Z simulation includes a $Z +$ Drell-Yan matrix element and

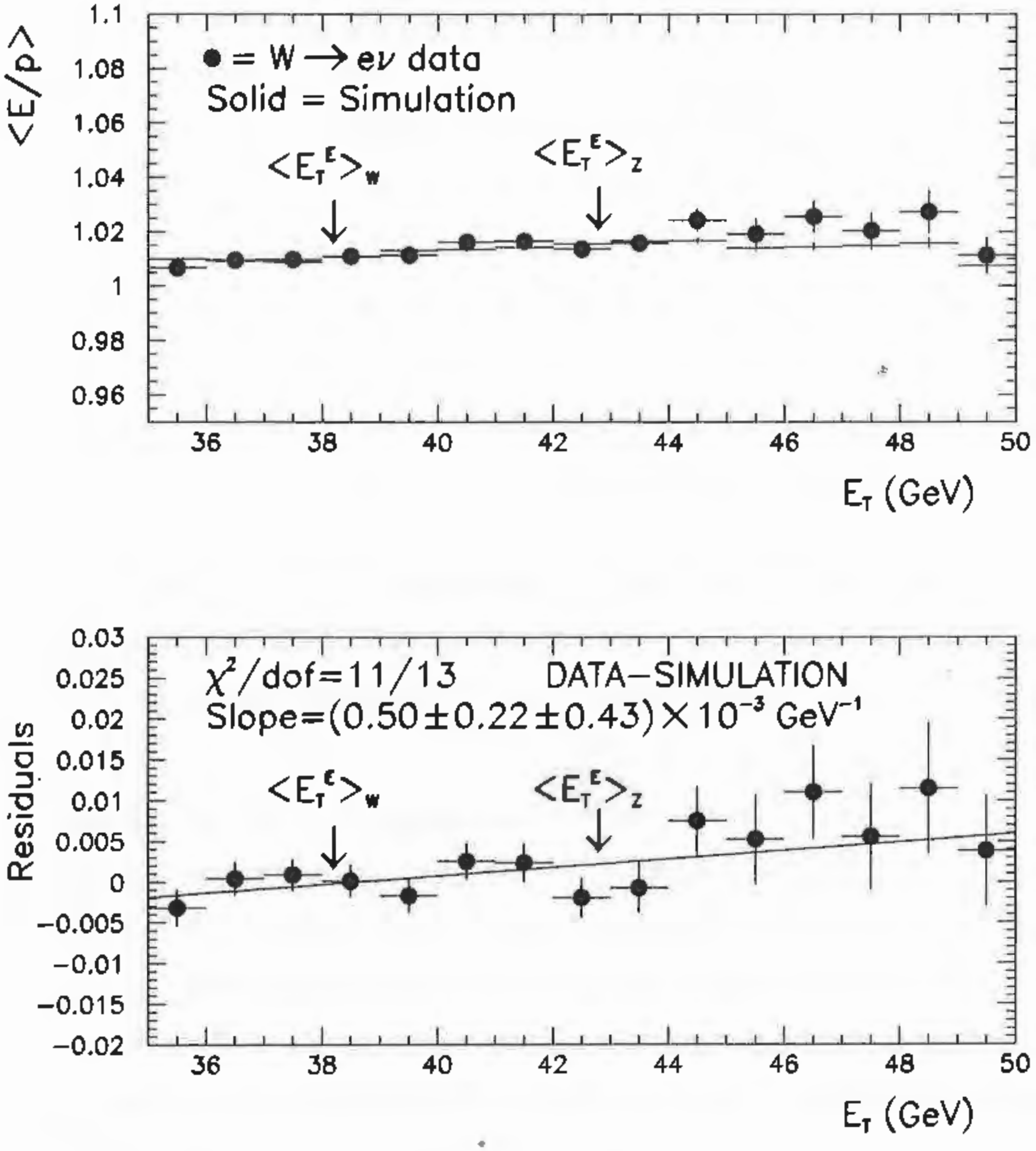

Figure 4.8: Upper: Variation of the mean of E/p with electron transverse energy in the data and radiative simulation. Lower: Data minus the simulation.

Effect	ΔM_Z^{ee} (MeV/c^2)
Statistics	190
CEM constant term	negligible
Structure function choice	negligible
Non-linearity	200
Backgrounds	10
Fitting	5
Scale	150
Total	310

Table 4.8: Uncertainties in measuring the Z mass. Uncertainties less than 5 MeV/c^2 are considered negligible.

includes a parameterization of the radiative decay, $Z \rightarrow ee\gamma$, as described by Berends and Kleiss [33] and implemented by R. G. Wagner [34]. The mass shift from including the Drell-Yan term is negligible; including radiative decays in the templates shifts the mass by 140 MeV/c^2.

A summary of the uncertainties in measuring the Z mass is shown in Table 4.8. The mass is determined with a statistical precision of 190 MeV/c^2. Using the same technique as used to measure systematic uncertainties in the scale measurement, no significant dependence on the Z mass is seen on the choice of the electron constant term within its 1σ bounds. Similarly, no significant dependence is seen on the structure function choice. As described in the previous subsection, the fitted Z mass is lowered by 210 ± 200 MeV/c^2 to account for the calorimeter non-linearity in transferring the scale measured for W electrons to Z electrons. The background rate due to "QCD," *i.e.*, events due to jets faking electrons or electrons from heavy-flavor, is estimated in the same way as done for the W sample in Chapter 7 to be fewer than 0.3 events. Similarly, $Z \rightarrow \tau\tau$ decays add fewer than 0.1 events. If 0.4 events were in the sample, the worst-case background shape would shift the mass by 10 MeV/c^2, which is taken as an uncertainty due to backgrounds. Due to the finite statistics used in the lineshapes for fitting, an uncertainty of 5 MeV/c^2 is incurred. The 0.16% uncertainty in setting the energy scale corresponds to the 150 MeV/c^2 uncertainty at the Z mass.

Accounting for the final energy scale measurement being 0.02% different from that used for reconstruction, the measured Z mass using electrons is

$$90760 \pm 190 \text{ (stat.)} \pm 250 \text{ (syst.) MeV/c}^2. \tag{4.5}$$

This is 1.4 standard deviations from the LEP value of of 91187±7 MeV/c^2 [32]. The large uncertainty demonstrates that it is preferable not to normalize the W mass measurement to the Z mass. The data and best fit are shown in Figure 4.9.

One may compare the Z mass measured from data before and after the January access using separate determinations of the scale from E/p. The before–after shift in the Z mass is +900±420 MeV/c^2. However, the corresponding shift in the W data, where the sensitivity to a shift is greater (since there is more statistical power and most systematic uncertainties cancel in the comparison), is found to be only +70±340 MeV/c^2.

4.9 Summary

This chapter described how the W electrons are reconstructed and their energy response calibrated. The $W \rightarrow e\nu$ and $Z \rightarrow ee$ data samples used in the analysis are described. The resolution of the CEM electron energy measurement was studied and a value for the constant term in Equation 4.1 of $\kappa = (1.2^{+0.9}_{-1.2})\%$ was measured, in good agreement with other estimates. The

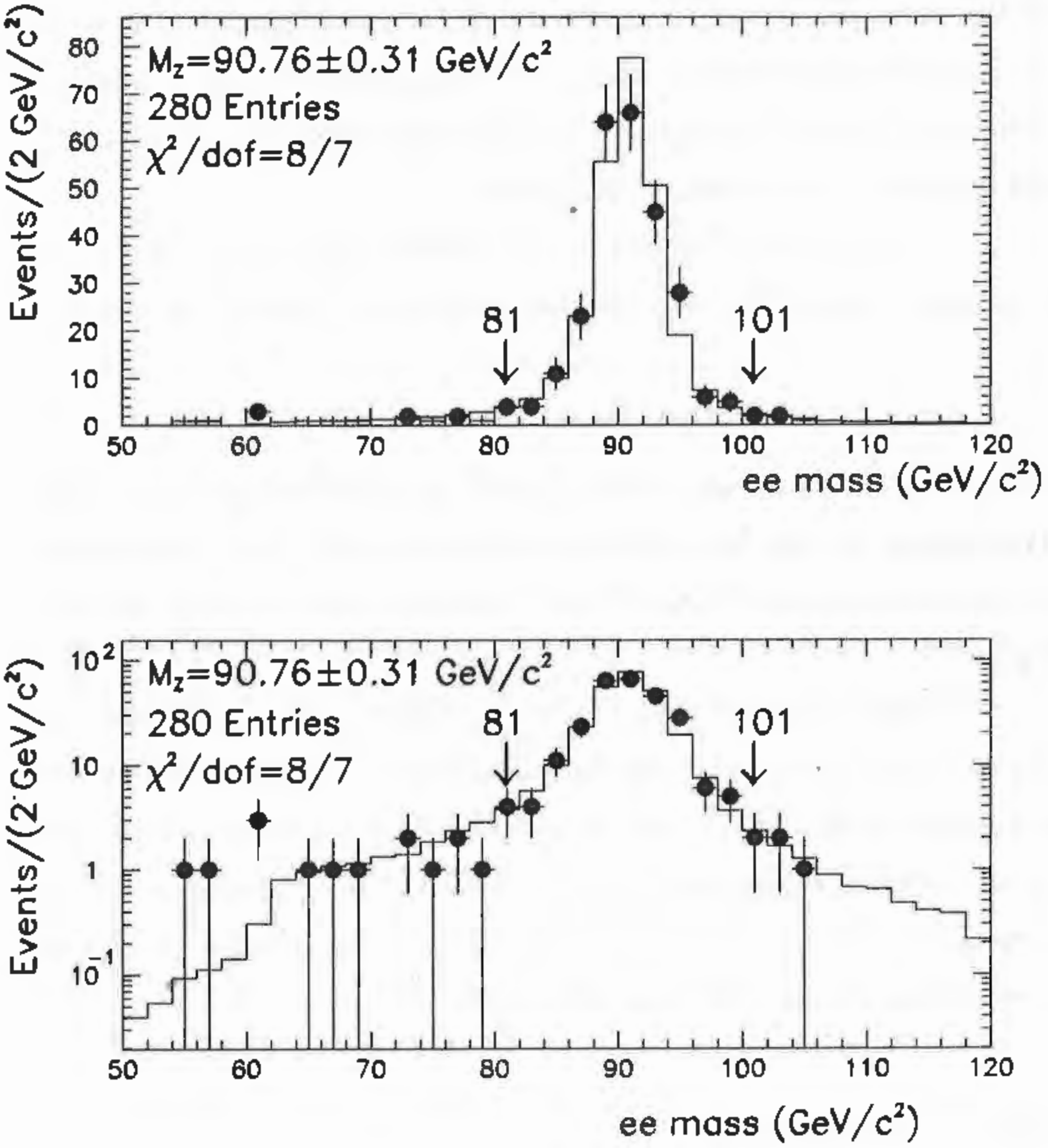

Figure 4.9: Upper: Dielectron mass of events arouud the Z peak. The points are the data shown on linear scale. Lower: logarithmic scale. The solid line is the simulation for the best-fit mass.

CEM scale was determined with an overall uncertainty of 130 MeV/c^2 at the W mass. A CEM calorimeter non-linearity of -210 ± 200 MeV/c^2 at the Z mass relative to the W mass was measured. As a check, the extracted mass of the Z, 90760 ± 310 MeV/c^2 was compared to the precisely measured value from LEP, 91187 ± 7 MeV/c^2.

Chapter 5

RECOIL MEASUREMENT

As discussed in Chapter 2, the only measured quantities relevant to the W mass measurement are the transverse momenta of the electron and the recoiling hadrons. The preceding chapters described the electron energy and momentum measurements in detail; this chapter describes how the recoil is reconstructed, including the corrections applied to avoid biasing the transverse mass measurement.

5.1 Recoil Reconstruction

The CDF detector is instrumented with sampling calorimetry used over the range $|\eta| < 3.6$ [20]. Each detector consists of an electromagnetic detector in front of a hadronic detector. Detector energy thresholds are set above the RMS spread of the noise characteristic of each detector, ranging from 100 MeV for the central detectors to 800 MeV for the forward hadronic detectors. The detectors are segmented into towers each covering a range of $\sim 0.1 \times 15^0$ in $\eta - \phi$ space in the central region and $\sim 0.1 \times 5^0$ in the "plug" and "forward" detectors. A full description of the coverage and segmentation of all the calorimetry subsystems may be found in Table 3 of Reference [13]. The energy in each tower is converted to a transverse energy using:

$$E_T^{\text{tower}} = E^{\text{tower}} \cdot \ sin\ \theta, \tag{5.1}$$

where E^{tower} is the energy measured in the tower and θ is the polar angle between the beamline and the vector pointing from the W event vertex to the center of the cell. The nominal W event vertex is the closest well-reconstructed vertex to the extrapolation of the electron track back to the beamline.

The nominal energy scale of each detector was transferred from test-beam electrons and pions. The calibrated response is essentially that for 50 GeV/c beams. For this measurement, an absolute recoil energy calibration is achieved by balancing momentum in $Z \rightarrow ee$ events using the event modeling technique described in Chapter 6.

To study the modeling of W production and the measurement of the recoil, the recoil transverse energy vector, $\mathbf{u}$, is conveniently decomposed into its components, $u_{//}$ and $u_{\perp}$, where $u_{//}$ is the component of the recoil parallel to the electron's azimuthal direction and $u_{\perp}$ is perpendicular to it. As evident from Equation 2.3, care must be taken not to bias the component of the recoil parallel to the electron direction, $u_{//}$, because that would systematically shift the transverse mass measurements. Several effects are investigated: systematic shifts from leakage of the electron shower into neighboring towers, soft particles from the recoil hitting the same towers as the electron cluster without causing it to fail the electron identification cuts, and biases in $< u_{//} >$ due to the electron identification cuts.

The bias due to excising the electron from the event may be estimated. The recoil energy flow near the electron and the energy leakage are measured by looking at the towers adjacent in azimuth to the electron cluster.

The measured energy should be the sum of two contributions: the hadronic recoil and leakage or bremsstrahlung from the electron [38]. Figure 5.1 shows that measuring the average energy of these towers as a function of the position of the electron shower resolves the two contributions. Consequently, whenever the electron shower is within 10 cm of an azimuthal boundary, the corresponding adjacent towers are removed from the recoil measurement. The two or three towers defining the electron cluster are always removed. The baseline transverse energy, 30 MeV per tower, is added back into every W event to offset this systematic effect. The uncertainty on the measurement of the underlying event energy excised with the electron is 2 MeV/tower for an average uncertainty of 9 MeV on $< u_{//} >$ since an average event has 4.5 towers removed. Since $M^W \approx 1.1 \times\ M_T^W$, an uncertainty on the W mass of 10 MeV/c^2 due to electron removal is taken.

The bias due to electron identification cuts on $< u_{//} >$ may be estimated. If the W decays such that the electron travels in the same direction as the recoil, there is greater opportunity for the particles in the recoil to cause the electron identification to fail. Quadrupling the size of the track isolation cone around the electron indicates that the cut produces a -44 MeV bias on $< u_{//} >$; however, the corresponding shift in the W Mass is 0 ± 15 MeV/c^2. The electromagnetic fraction cut has been measured in the testbeam as well as estimated from detector simulations [39] to be better than 99.5% efficient. Tightening this cut to 0.070 from the nominal 0.100 causes an additional 1% (twice as much) of the sample to be lost and shows a $+3$ MeV shift on $< u_{//} >$, and a $+20 \pm 10$ MeV/c^2 shift of the W mass. These shifts should be taken as upper bounds since the efficiency of the electromagnetic fraction cut is a lower bound. Although these shifts, and that in the previous paragraph, are

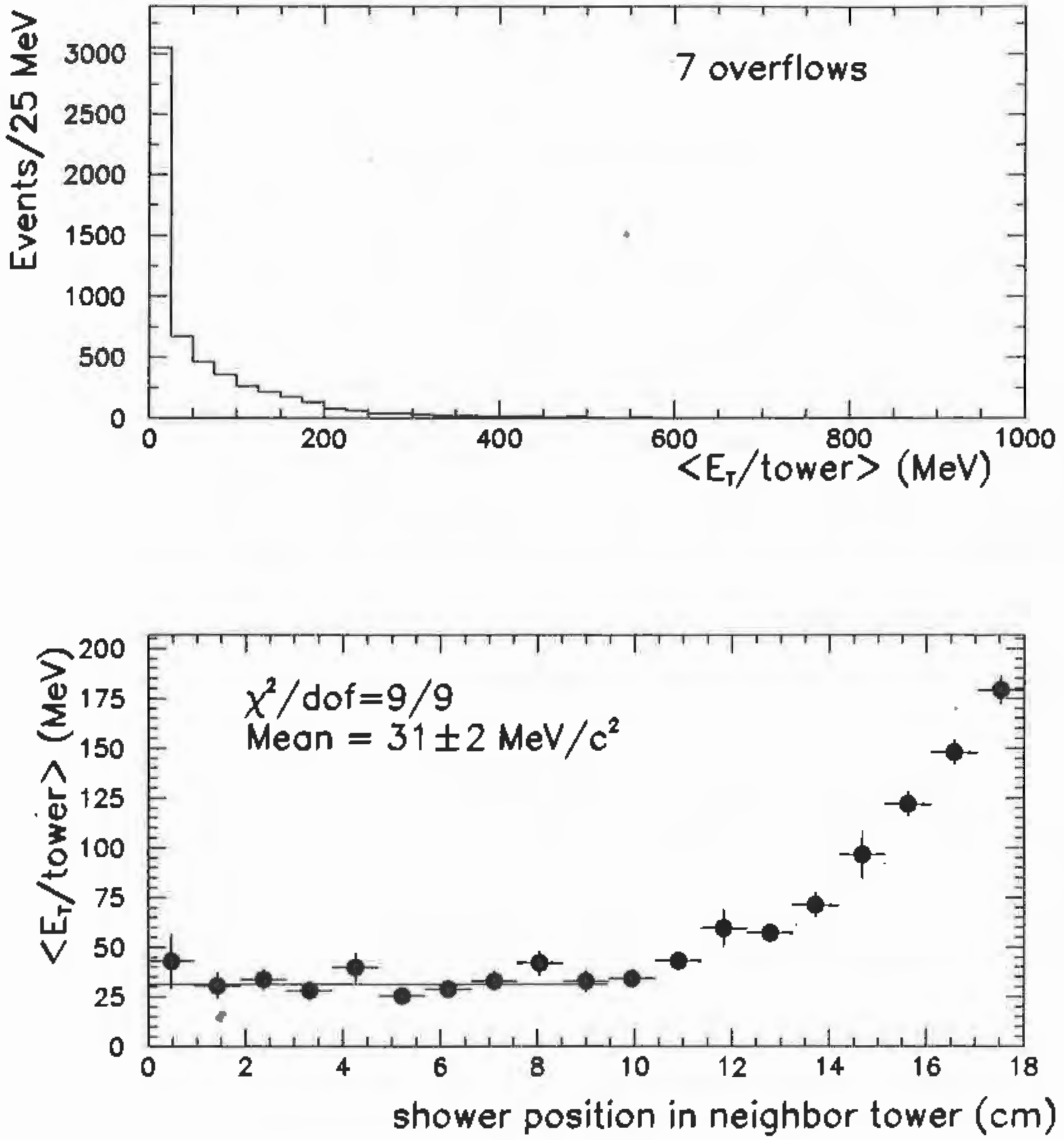

Figure 5.1: Upper: Distribution of average energy per tower adjacent to electron cluster in azimuth. Lower: Average energy flow in towers adjacent in azimuth to the electron cluster (neighbor tower) as a function of the electron shower position.

only marginally statistically significant, 20 MeV will be taken as a systematic uncertainty due to electron identification and removal.

5.2 Recoil Distributions

The widths of the $u_\perp$ and $u_{//}$ distributions respectively constrain and check the W p_T spectrum used in the simulation. The distribution of the absolute value of the vector **u** for the W data is shown in Figure 5.2. The distributions of the components, $u_{//}$ and $u_\perp$ are shown in Figures 5.3 and 5.4. The simulation is superimposed. Note that the agreement is good even though the distributions have a shape different from a simple Gaussian. The simulation described in Chapter 6 predicts an offset in $< u_{//} >$ of -483 MeV/c^2. This is in excellent agreement with the measurement of $-473 \pm 70 \pm 45$ MeV/c^2, where the first uncertainty is statistical and the second uncertainty is the limit placed on systematic bias in the preceeding section. Additional demonstrations of the model's ability to simulate the behavior of the recoil measurement are shown in the following chapter, after the event simulation is described.

5.3 Summary

The reconstruction algorithm of the recoil transverse energy and thus neutrino transverse energy has been described. The electron identification and removal could cause biases in the average of the $u_{//}$ distribution. An offset of -483 MeV is predicted and -473 ± 80 MeV is observed. Electron identification and removal contributes an uncertainty of 20 MeV/c^2 on the W mass.

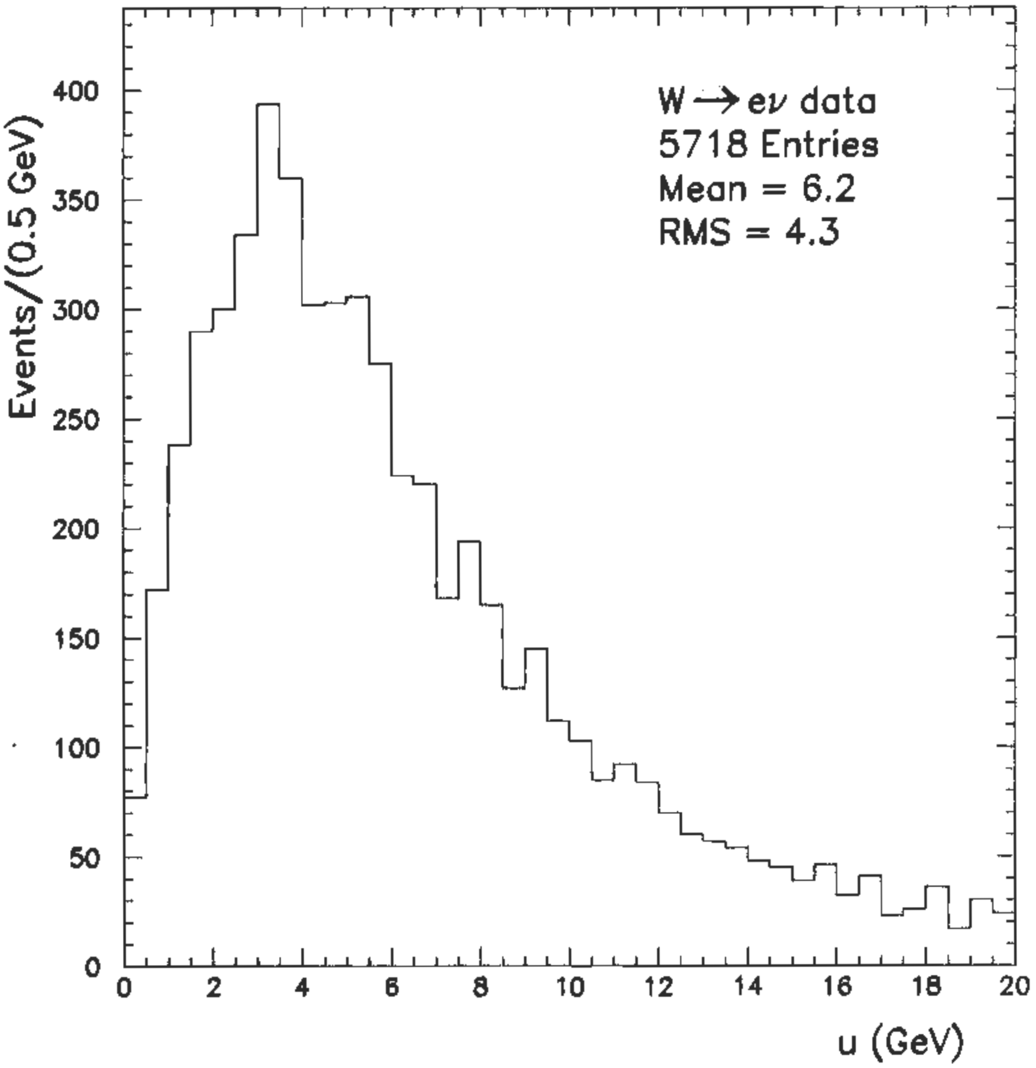

Figure 5.2: Distribution of |u| in the $W \to e\nu$ sample.

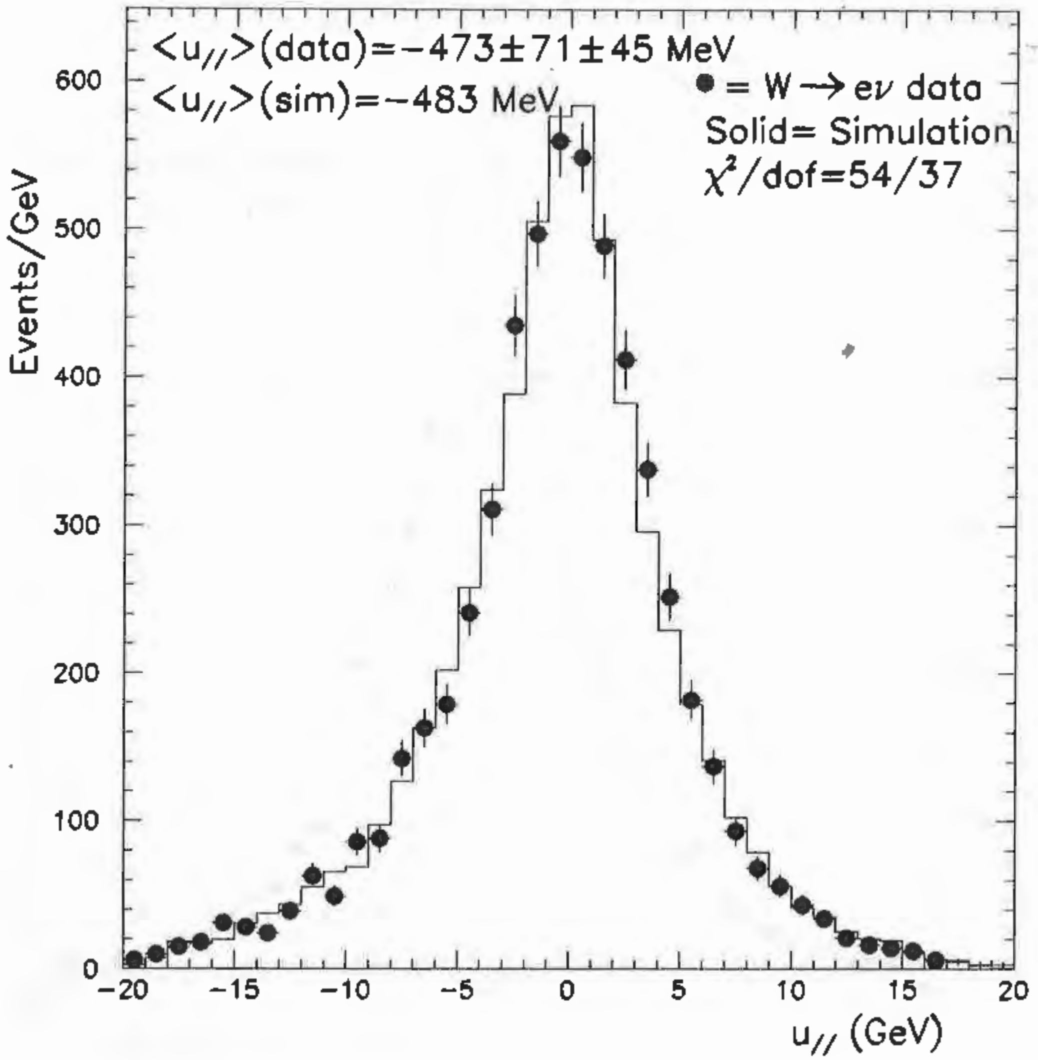

Figure 5.3: Distributions of $u_{//}$ in the $W \rightarrow e\nu$ data (points) and from the simulation (histogram).

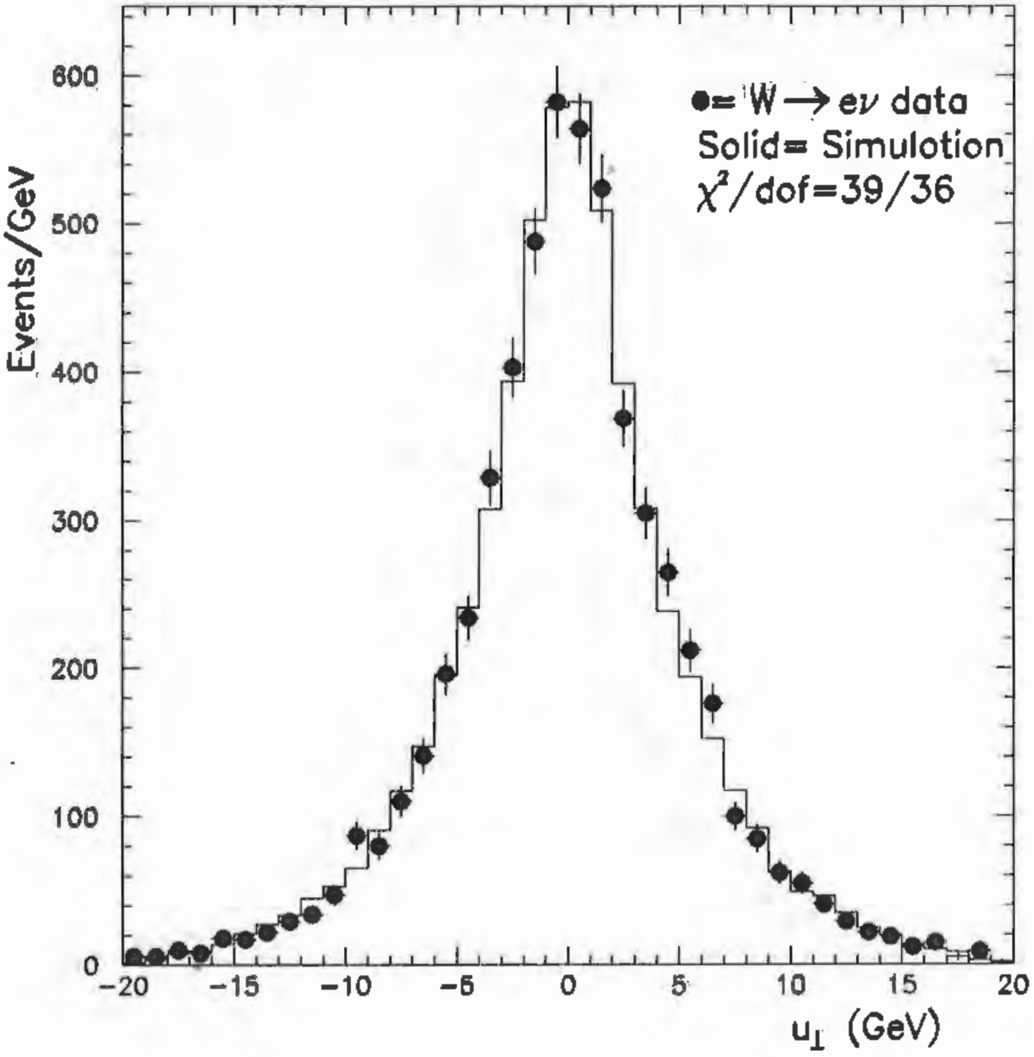

Figure 5.4: Distributions of $u_\perp$ in the $W \rightarrow e\nu$ data (points) and from the simulation (histogram).

Chapter 6

EVENT MODELING

To predict the shape of the transverse mass spectrum for a particular W mass, a model of W production and decay must be assumed. Since the modeling of the W production and the modeling of the recoil are so closely linked in this analysis, they are described together in this chapter. The chapter begins with how the analysis attempts to circumvent at the outset the experimental and theoretical difficulties related to W production by exploiting the transverse mass. The following section describes the details of the simulation of W production. The matching of the detector response to the W recoil follows. The performance of the model is investigated using the most relevant variables: E_T^e, E_T^ν, $u_{//}$, $u_\perp$, $|\mathbf{u}|$, and M_T^W. The next section provides estimates of the contributions to the systematic uncertainty. The last section presents a study of several effects on the W mass using higher-order W production models.

6.1 Why Transverse Mass is Used

While the properties of W decay are well-described by the Standard Model, an accurate description of W production is problematic for two reasons. First, the z-component of the recoil momentum cannot be measured, so the invariant mass of the W cannot be reconstructed on an event-by-event basis. Second, the contributions of initial state radiation and higher-order QCD processes are difficult to calculate or measure. The first contribution contributes mostly an uncertainty on the z-component of the W momentum, p_z^W; the second yields an uncertainty also on its transverse components, p_T^W. Using the transverse mass reduces the effects of both uncertainties. Since only components transverse to the beamline are used, p_z^W does not enter directly, but enters primarily as an acceptance uncertainty arising from the experimental constraint that electrons hit the central detector region. It is the purpose of the transverse mass defined in Equation 2.1 to be invariant to p_T^W boosts to first order, so uncertainties on the transverse momentum spectrum with which the W are produced enter through mis-measurements of the W recoil, $\mathbf{u}$, and to a lesser extent through acceptance effects.

6.2 *W* Production Model

The simulation is based on a leading-order W generator [40] which simulates the W events using the MRSD$-'$ parton distribution functions. The simulated W is boosted in the center-of-mass frame of the quark-antiquark pair producing the W with a transverse momentum spectrum derived from the $Z \rightarrow ee$ data. The p_T spectrum of $Z \rightarrow ee$ events is theoretically expected to be similar to the W p_T spectrum [41]. Nevertheless, the equality of the

W and Z transverse momentum spectra is not assumed, but rather the Z p_T spectrum is only used as an initial guess for the W p_T spectrum. The actual shape of the p_T spectrum of the events in the sample is constrained by the W data themselves. The electron resolution and acceptance are the same as used for the simulations in Chapter 4. The MRSD–$'$ structure functions are chosen as the nominal set since they most closely describe the observed W decay charge asymmetry at CDF [25] which is sensitive to the proton structure [42].

To use the W data to constrain the p_T^W spectrum from which the events should be generated, it is first necessary to understand the measurement of the W recoil. The distribution of the recoiling particles and the detector response to them are difficult to model or measure at the requisite precision. Fortunately, Z bosons are produced at the Tevatron with p_T spectra similar to that of W bosons. Using the facts that both electrons in $Z \rightarrow ee$ events are detected and that the electron energies are measured with better resolution than the recoil allows the response of the detector to the range of recoils to be calibrated. Specifically, when the W simulation generates a W with a particular transverse momentum, the recoil $\mathbf{u}$ measured from a $Z \rightarrow ee$ event with the same transverse momentum is inserted as the underlying event. Only Z events with a central electron are used, while the second electron may be detected within the region $|\eta| \leq 3.6$. The advantage of this technique is that only the W p_T spectrum remains to be tuned to the data; the detector response to the recoil is not tunable. Small imperfections in the recoil modeling due to, for example, the finite Z statistics or the smearing of the Z p_T measurement from electrons would be largely compensated by the p_T^W tuning. Figure 6.1 shows a scatter plot of $|\mathbf{u}|$ versus p_T measured with the electrons in the $Z \rightarrow ee$ events used in this technique.

For demonstration purposes, it is interesting to see the variation of

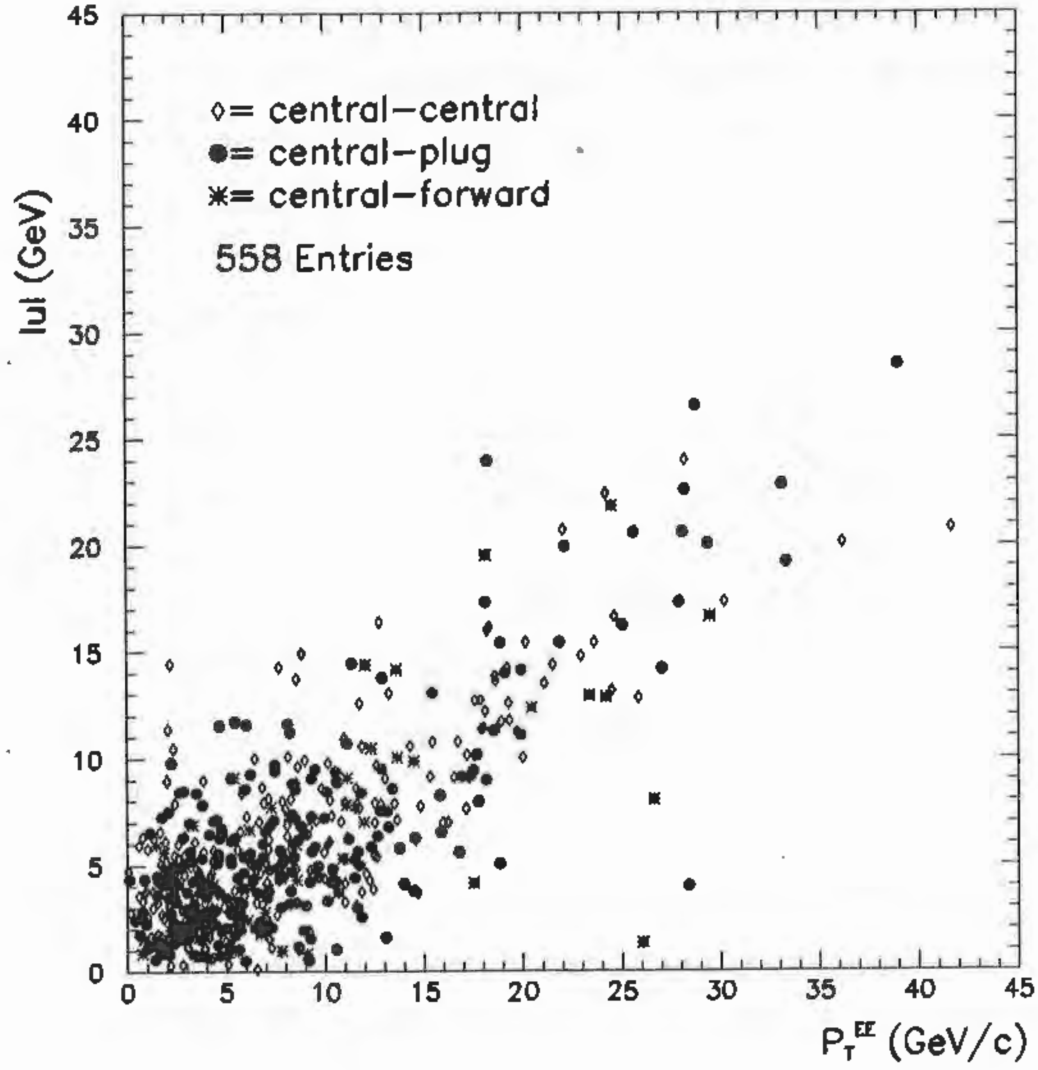

Figure 6.1: Scatter of |u| versus p_T measured with the $Z \to ee$ events.

$|\mathbf{u}|$ with p_T along an axis where the measurement error due to the electrons is minimized, *i.e.*, the perpendicular bisector of the two electrons. A scatter plot of the projections of $\mathbf{u}$ versus p_T^Z along this axis, *i.e.*, u_η versus p_η, is shown in Figure 6.2. Note that the two worst outliers in Figure 6.1 are also the two worst outliers in Figure 6.2, indicating that it is the recoil measurement, not the lepton energy measurement which is causing the deviation. These events and even the next worse outlier are all in the tail of the z-vertex distribution where the recoil measurement is expected to be worse since there are larger cracks into which recoiling hadrons can escape undetected. Thus, the method of inserting underlying events from $Z \rightarrow ee$ data reproduces significant, but rare, deviations, which would be difficult using a parameterization.

Figures 6.1 and 6.2 show that the $\mathbf{u}$ vector was under-reconstructed. This deliberate under-reconstruction of the underlying energy produces the best resolution on the W mass. In the following section, a demonstration is given to show that the change in scale does not introduce additional systematic error on the W mass.

6.3 Constraints and Performance of Model

The width of the $u_\perp$ distribution, 5.28 ± 0.05 GeV/c^2, is used to constrain the shape of the p_T^W spectrum given to W events in the simulation. The width of the $u_{//}$ distribution, 5.36 ± 0.05 GeV/c^2, serves as a check since it is potentially subject to other systematic bias. An unsmearing of the observed $Z \rightarrow ee$ p_T spectrum, where the same cuts on the topology of the energy flow in the event are placed on the Z events as on W events, is used as the nominal spectrum and shown in Figure 6.3. Table 6.1 shows how the widths of the $u_{//}$ and $u_\perp$ distributions predicted by the simulation change as the assumed p_T^W

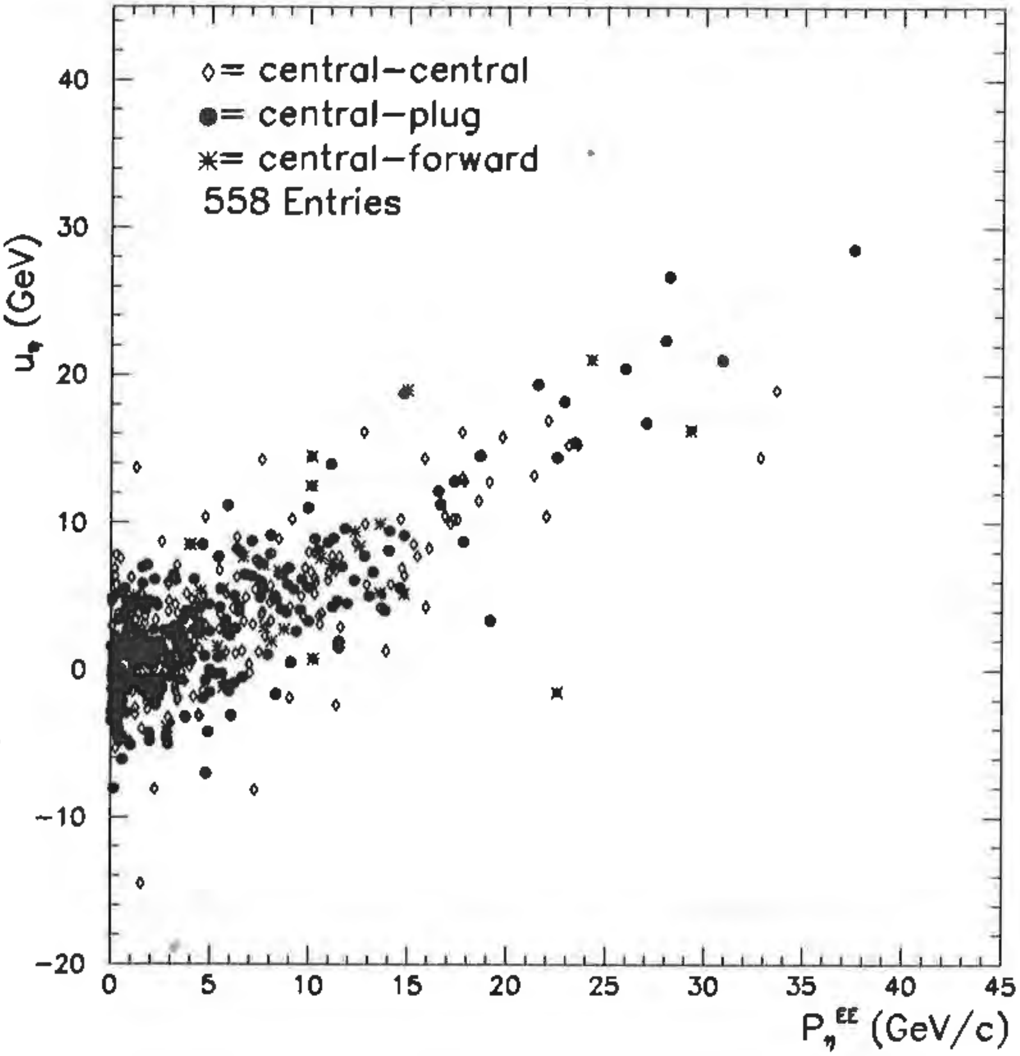

Figure 6.2: Scatter of u_η versus p_η measured with the $Z \rightarrow ee$ events.

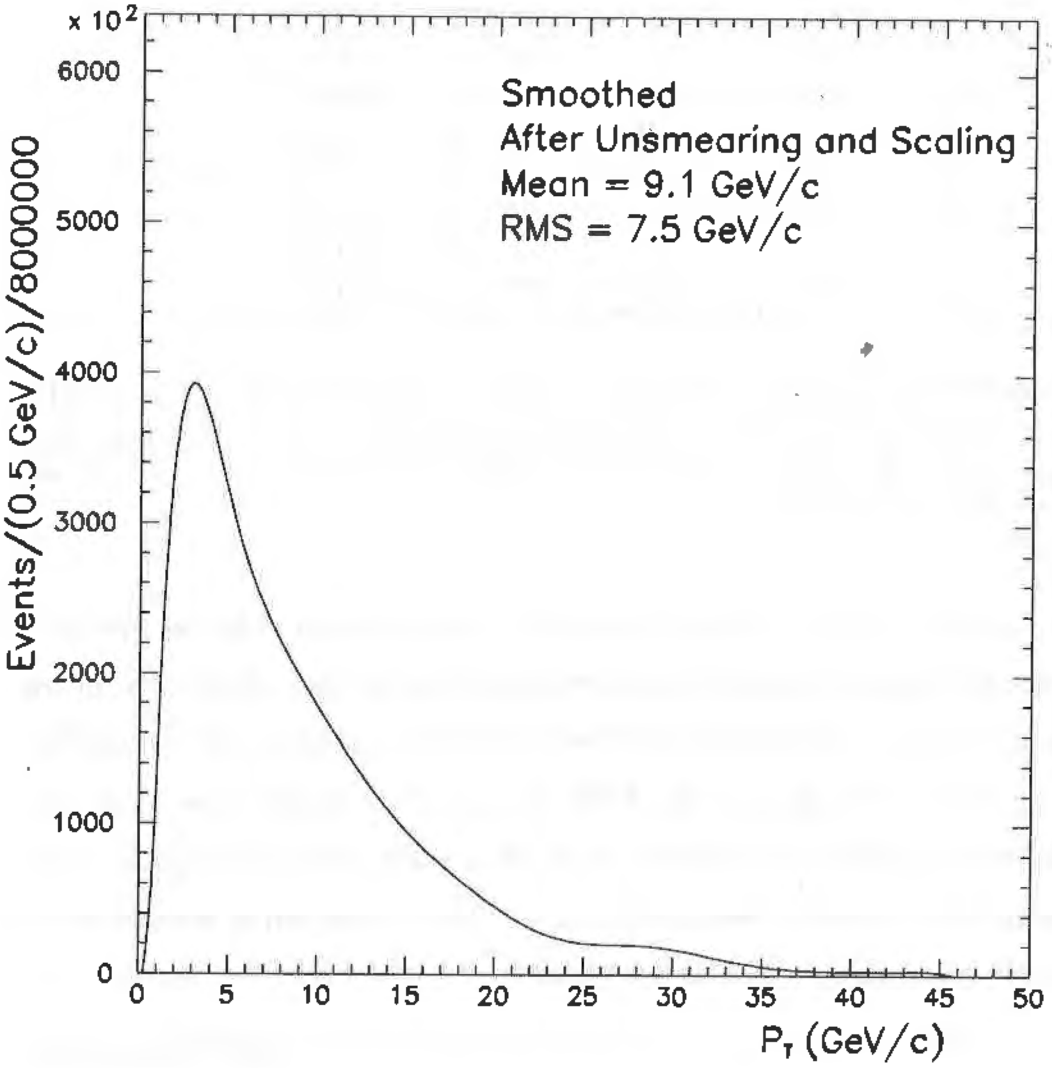

Figure 6.3: The p_T^W spectrum used in the generator. It is derived from the $Z \rightarrow ee$ data after unsmearing.

r	RMS($u_{//}$) (MeV)	RMS($u_\perp$) (MeV)	ΔM_W (MeV/c^2)	$\Delta\Gamma_W$ (MeV)	
1.08	5.23	5.14	-30 ± 19	-322 ± 46	
1.10	5.28	5.18	-7 ± 19	-206 ± 59	
1.11	5.32	5.21	-2 ± 19	-170 ± 51	
1.12	5.38	5.28	-1 ± 19	-44 ± 54	nominal
1.13	5.42	5.32	$+22 \pm 19$	-30 ± 52	
1.14	5.47	5.38	$+31 \pm 19$	$+80 \pm 49$	
1.16	5.53	5.43	$+69 \pm 19$	$+150 \pm 34$	

Table 6.1: Variation of the RMS of $u_{//}$ and $u_\perp$, and systematic mass and width shifts with the scale factor on p_T^W, r, used in the $W \rightarrow e\nu$ simulation. The mass shift is for a fixed-width fit. The width shift is for a fit with both the mass and width floating.

spectrum is scaled by a factor r in the $W \rightarrow e\nu$ simulation. The corresponding mass shift for having other than the nominal distribution is obtained by fitting simulated data with a different r factor to spectra generated in the nominal way. The "1σ" values on the RMS of $u_\perp$ applied to this table show that the scale factor is determined to be 1.120 ± 0.014, which corresponds to an uncertainty on the W mass of 20 MeV/c^2. The corresponding uncertainty on the W width measurement is 120 MeV.

In case one is concerned by the factor $r = 1.120 \pm 0.014$ being greater than unity, one must first note that it cannot be directly interpreted as the true ratio between the mean W and Z p_T. To give such a natural meaning to the ratio, several other experimental uncertainties are incurred. The finite Z statistics in the p_T^Z spectrum would contribute an uncertainty of 2.5% to the scale factor, so interpreted. Second, although care was taken to make the selection criteria as close as possible, several differences lead to additional sources of uncertainty: The Z data were required to pass a track isolation requirement on both legs; changing the cut to one legs shifts $< p_T^Z >$ by +2.0%. The jet cut is made at 30 GeV for both samples; had the jet cut been scaled by the boson mass ratio, there would be a shift of +2.5%. The "first" electron had a p_T cut applied at 15 GeV/c; scaling the p_T cut to 17 GeV/c for the Z electrons which have higher $< E_T >$ scales $< p_T^Z >$ by +4.0%. The unsmearing of the p_T^Z spectrum shifted $< p_T^Z >$ by +2.5% which sets the scale of the corresponding uncertainty. The Z data were selected with one leg passing an isolation requirement. The effect of this cut is investigated by requiring both legs to be isolated; no shift is seen. Combining these uncertainties in quadrature yields a ratio of 1.120 ± 0.053. Second, combining published data from CDF on the p_T spectra of the W and Z bosons [43],[44] with a $p_T^{W/Z}$ cutoff at 20-30 GeV/c, yields a ratio of 1.2-1.3. (With no $p_T^{W/Z}$ cutoff, the value becomes 0.8)

In addition to scaling the p_T^W spectrum, a study is performed where the p_T^W spectrum is skewed keeping its mean constant using

$$p_T^W(skewed) = 9.1 \text{ GeV/c} \ + \ s \times (p_T^W - 9.1 \text{ GeV/c}), \tag{6.1}$$

where s is the skew parameter. If p_T^W is skewed to a value below zero, it is set to zero. The range of parameters is bounded by the RMS of the $u_\perp$ distribution with $|\mathbf{u}| < 10$ GeV to within 4% of no skew. As a check, the truncated RMS of $u_{//}$ behaves as expected as the skew is added. The truncation is performed to be sensitive to a different part of the $\mathbf{u}$ spectrum than that used to tune the scaling of the p_T^W spectrum. Perhaps coincidently, the data coincide with no skew needing to be added, with the truncated RMS values of $u_{//}$ and $u_\perp$ being 3.67 ± 0.04 GeV and 3.69 ± 0.04 GeV, respectively. Note that it was verified that the skewing algorithm does not contribute to a significant scaling of the p_T spectrum; so this uncertainty on s is independent of the uncertainty taken

s	RMS($u_{//}$) (MeV)	RMS($u_\perp$) (MeV)	ΔM_W (MeV/c^2)	$\Delta\Gamma_W$ (MeV)	
1.20	3.44	3.44	-127 ± 14	-310 ± 40	
1.10	3.56	3.56	-25 ± 14	0 ± 40	
1.00	3.67	3.69	-1 ± 19	-44 ± 54	nominal
0.90	3.78	3.77	$+52 \pm 14$	$+30 \pm 30$	
0.80	3.89	3.88	$+78 \pm 14$	$+20 \pm 30$	

Table 6.2: Variation of the RMS of $u_{//}$ and $u_\perp$, and systematic mass shift with the skew parameter, s, used in the $W \to e\nu$ simulation. A one-sigma variation on s covers the range $0.96 - 1.04$. The mass shifts are for a fixed-width fit. The width shifts are for a fit with both the mass and width floating.

for the tuning of the p_T^W scale factor, r. Table 6.2 indicates that a systematic uncertainty of 20 MeV/c^2 on the W mass and 50 MeV/c^2 on the W width should be taken to account for skewing of the input p_T spectrum.

Other uncertainties accrue from using the $Z \to ee$ events to calibrate the detector response to the W recoil. These are distinguished from the uncertainties due to the scaling and skewing of the input p_T^W spectrum in the simulation. Two uncertainties on the recoil modeling are identified and investigated. First, the effect of statistical fluctuations arising from the finite size of the Z sample, 558 events[1], is investigated by generating artificial data with one-fourth of the Z events. Assuming the uncertainty scales as the square root of the number of Z calibration events, the calculated uncertainty on the W mass is 50 ± 20 MeV/c^2. Second, the effect of the energy smearing of the electrons on the Z p_T is investigated by adding an additional electron smearing to each electron in the measurement. After correcting for the additional spreading of $u_\perp$ caused by the p_T^Z smearing (which corresponds to a small change of r from 1.12 to 1.10), the returned value is shifted by -35 ± 15 MeV/c^2,

---

[1] This is greater than the 544 events in Table 4.2 since the cut on $|\mathbf{u}|$ is removed.

which is taken as the corresponding uncertainty. Note that the real difference would probably be smaller since the unsmearing of the input p_T^W spectrum would have accounted for this extra lepton smearing. This uncertainty is also probably a double-counting since an uncertainty is also already included for the skew of the input p_T^W, and so is conservative. The combination of these two effects, finite number of Z events and the smearing of the p_T^Z measurement by the electron measurement, was independently investigated by remaking many W and Z datasets of the same size as used in this analysis with `HERWIG` [45] and a general-purpose detector simulation and looking at the spread in fitted W masses. The observed spread in masses, 40 ± 10 MeV/c^2 agrees well with this result of 60 ± 25 MeV/c^2 for the recoil modeling uncertainty and perhaps even shows it to be conservative. Moreover, the W width measurement made in Chapter 8 will serve as an additional independent check on the resolutions. These two effects, the finite number of Z events used, and the smearing of the electrons used to measure the p_T of the Z, contribute 170 MeV and 200 MeV systematic uncertainties to the W width, respectively.

As a demonstration of the ability of the simulation of the event production and recoil to reproduce the data, the spreads and mean of $u_{//}$ and $u_\perp$ for data and simulation are compared for different cuts on magnitude of the recoil, $|\mathbf{u}|$. Table 6.3 shows the agreement.

The largest bias to $< u_{//} >$ arises from the selection of events with cuts on the electron transverse energy. W events which decay at an angle such that the electron is boosted by the transverse momentnm of the W are preferentially kept. Figure 6.4 shows the data and simulation for $< u_{//} >$ as a function of the E_T of the electron. There is a variation of 28 GeV in $< u_{//} >$ over the range of electron transverse energies, $25 < E_T < 55$ GeV, which the accompanying plot of residuals shows is well-modeled. Similar plots versus the

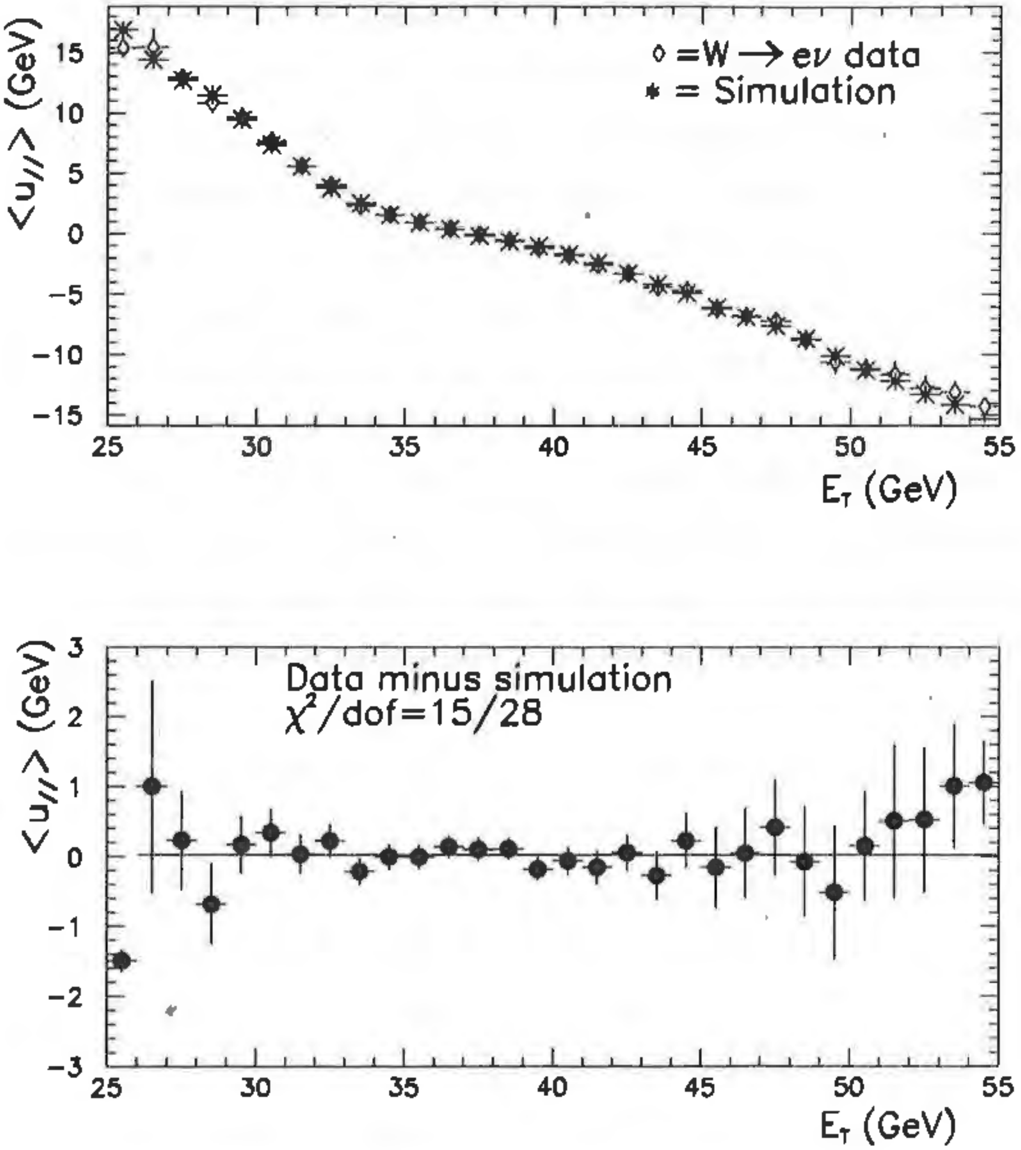

Figure 6.4: Upper: Data (diamonds) versus predicted (asterisks) value of mean offset of $u_{//}$ as a function of the electron E_T. Lower: The residuals of the data minus the simulation.

|u| cut	$< u_{//} >$		$RMS(u_{//})$		$RMS(u_{\perp})$	
(GeV)	(data) (MeV)	(sim) (MeV)	(data) (GeV)	(sim) (GeV)	(data) (GeV)	(sim) (GeV)
20	-473 ± 72	-483	5.36 ± 0.05	5.38	5.28 ± 0.05	5.28
15	-277 ± 63	-318	4.64 ± 0.04	4.74	4.61 ± 0.04	4.72
10	-91 ± 54	-125	3.67 ± 0.04	3.66	3.69 ± 0.04	3.67
5	$+20 \pm 40$	-45	2.23 ± 0.03	2.16	2.19 ± 0.03	2.15
3	-16 ± 40	$+12$	1.42 ± 0.03	1.38	1.37 ± 0.03	1.38

Table 6.3: Variation of the mean and RMS of $u_{//}$ and $u_{\perp}$ with the cut on |**u**| in the data and simulation.

E_T of the neutrino also show good agreement. The variation of $< u_{//} >$ with the transverse mass of the event shown in Figure 6.5. These variations are much smaller, ~ 2 GeV (which is why the transverse mass is used to extract the mass), and are well-described by the simulation. Plots of $< u_{//} >$ versus |**u**| prove to be sensitive to the quality of the event modeling. The data are compared to the simulation for these variables in Figure 6.5.

To quantify the uncertainty due to proton structure functions, many mock datasets of the same size as the true dataset are simulated with different structure functions and fit to the nominal spectra. [46] The measured systematic offsets in the fitted mass are shown in Table 6.4. Martin and Stirling point out that the shift in the W mass with structure function should be highly correlated with the corresponding shift in the mean W decay charge asymmetry [42]. The range of structure functions covers the range of W decay charge asymmetries allowed by the data [25] so the shift in the mass should thus be adequately constrained by this method. Although the variations are consistent with statistical fluctuations, a conservative uncertainty of 40 MeV/c^2 due to structure function choice is assigned. (Note that this uncertainty is much

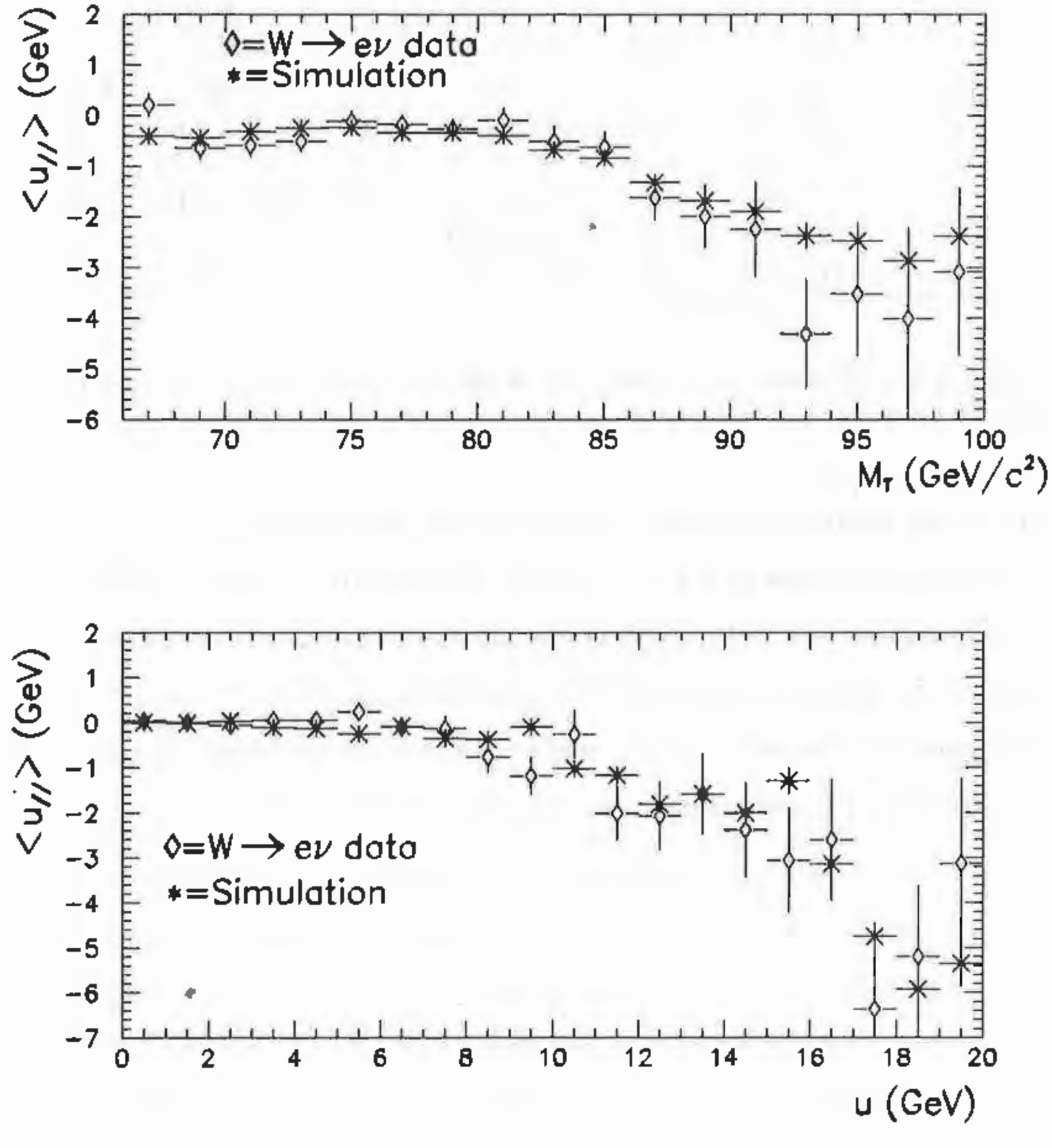

Figure 6.5: Upper: Data (diamonds) versus predicted (asterisks) value of the mean offset of $u_{//}$ as a function of M_T. Lower: Data (diamonds) versus predicted (asterisks) value of the mean offset of $u_{//}$ as a function of $|\mathbf{u}|$.

Structure Function	ΔM_W (MeV/c^2)	Status
MRSD–′	-8 ± 10	nominal
CTEQ2D	-13 ± 19	
CTEQ2M	$+7 \pm 19$	ruled out
CTEQ2L	$+7 \pm 19$	ruled out
CTEQ2ML	-7 ± 19	
CTEQ2MF	$+9 \pm 19$	
CTEQ2MS	$+3 \pm 19$	
CTEQ1M	$+3 \pm 19$	
MRSS0′	$+21 \pm 19$	
MRSD0′	$+18 \pm 19$	
MTB1	$+19 \pm 23$	ruled out
GRVH0	-34 ± 19	ruled out
MRSE′	$+71 \pm 19$	ruled out
HMRSB	$+28 \pm 9$	ruled out
MRSB	$+43 \pm 19$	1990 analysis

Table 6.4: Dependence of the W mass on structure function choice. The references for the various structure functions may be found in Reference [47].

Constant term (%)	ΔM_W (MeV/c^2)	$\Delta\Gamma_W$ (MeV)	
0.2	-42 ± 10	-250 ± 30	
0.7	-32 ± 10	-199 ± 28	
1.2	-1 ± 19	-44 ± 54	nominal
1.7	$+34 \pm 10$	$+114 \pm 24$	
2.2	$+89 \pm 10$	$+331 \pm 23$	
2.7	$+143 \pm 10$	$+568 \pm 20$	

Table 6.5: Variation in the W mass and width if a constant term in the electron resolution other than the nominal is used. The mass shift is for a fixed-width fit. The width shift is for a fit with both the mass and width floating.

smaller than that in the preliminary analysis since more structure functions sets are now excluded and the minimum transverse mass cut was raised from 60 GeV/c^2 to 65 GeV/c^2.) The shift for the MRSB set is shown for comparison to the 1990 analysis.

The fitted W mass also depends on modeling the electron resolution. The width of the $Z \rightarrow ee$ peak, discussed in Chapter 4, indicates that the appropriate constant term to use in Equation 4.1 is $(1.2^{+0.9}_{-1.2})\%$. Table 6.5 shows the variation in the fitted W mass from electrons when artificial data made with a constant term other than the nominal are fit. The corresponding uncertainties are 80 MeV/c^2 on the W mass and 340 MeV on the width.

The recoil energy is reconstructed with an energy scale derived from the nominal gains; this appears from Figure 6.1 to have been an under-reconstruction by about a factor of 1.5. This under-reconstruction, presumably due to cracks, calorimeter non-linearities and energy scale definitions, was deliberate since the using the nominal scale was measured to give the best resolution and statistical uncertainty on the mass measurement. As a check, the mass measurement is repeated with an additional scaling of 1.5 applied to all recoil measurements. The 5718-event mass sample becomes a 5228-event sample with this change in the reconstruction. The measured RMS of $u_{//}$ becomes 6.41 ± 0.06 GeV in agreement with the corresponding prediction by the simulation of 6.47 GeV. The RMS spread of $u_\perp$ was 6.53 ± 0.07 GeV in agreement with the corresponding prediction of 6.60 GeV. The offset in $< u_{//} >$ becomes $+210 \pm 89$ MeV in good agreement with the prediction of +181 MeV. The shift in the W mass had a scale factor of 1.5 been used rather than 1.0, is -79 ± 54 MeV where the uncertainty is the independent statistical uncertainty incurred in the comparison. The difference is neither statistically significant nor larger than the systematic uncertainty already quoted for scaling and skewing the p_T^W distribution and for systematic limitations of the recoil modeling.

The natural width of the W contributes to the shape of the transverse mass as most other resolution effects. For the nominal fits the W width is constrained to its measured value of 2063 ± 85 MeV [30]. Table 6.6 shows how the fitted mass depends on the W width used. The uncertainty taken on the W mass is 20 MeV/c^2 due to knowledge of the W width. This is conservative since the measured value agrees well with the theoretical value which has a smaller uncertainty. A fit to the data with both the W mass and width floated is performed in Chapter 8 as a check.

One must also be concerned with the possibility of a trigger bias that could bias the mass measurement. Here, a trigger bias is a mass shift due to missing events that would have been selected offline. The entire $W \rightarrow e\nu$ sample comes from one of these three triggers: an electromagnetic cluster with $E_T > 16$ GeV with a missing transverse energy of $\not{E}_T > 20$ GeV, where no track is required (CEM16MET20), an inclusive electron trigger at 9 GeV which requires a track (CEM9CFT9), and a jet with track and 20-GeV missing trans-

Γ_W (MeV)	ΔM_W (MeV/c^2)	
1663	-97 ± 14	
1883	-40 ± 14	
2063	-1 ± 19	nominal
2263	$+21 \pm 14$	
2463	$+102 \pm 14$	

Table 6.6: Variation of the fitted W mass with the assumed W width.

verse energy trigger (TAU20MET20). No events came in exclusively on an additional backup trigger requiring $\not{E}_T > 35$. Since these triggers cover the most likely failure modes, the inefficiencies may be calculated. The CEM16MET20 trigger was 99.8% efficient, where its failures were due mostly to not finding enough missing transverse energy. Given such high efficiency, the CEM9CFT9 served as an adequate backup with its 93.1% efficiency. Only 3 events failed both of the first two triggers due to hardware failures during electromagnetic cluster finding. Since any combination of these triggers is allowed, less than one event is expected to have been missed, so the trigger bias on the mass measurement is negligible.

A potential problem with the leading-order generator used is that it does not allow changes in the polarization of the W as the p_T of the W increases. Chiappetta and Le Bellac have shown that the change of polarization adds a term to the angular distribution of the electron from the W decay [48]. When averaged over charges, the angular distribution of the electrons becomes

$$\frac{d\sigma}{d(cos\theta)} = (1 + cos^2\theta) + \alpha(1 - 3cos^2\theta), \tag{6.2}$$

where the first term is reproduced by the leading-order generator and the second term is the correction due the higher-order correction. For the W

events in the mass sample, $< \alpha > \sim 0.7\%$ and is almost always less than 3%. Fitting artificial data made with $\alpha = 10\%$ to the nominal lineshapes shifts results in a fitted mass $+156 \pm 13$ MeV/c^2 from the nominal. So 10 MeV/c^2 is assigned as an uncertainty due to W polarization.

To estimate the uncertainty due to the assumption of the rapidity-independence of the p_T^W spectrum, a theoretical double-differential spectrum of W production in p_T and rapidity provided by Arnold and Kauffman [49] with $\Lambda_{QCD} = 300$ GeV is used [50]. Constraining the Arnold-Kauffman spectrum to reproduce the width of the $u_\perp$ distribution requires that their theoretical p_T^W spectrum be scaled by a factor 0.977. First, as a check, when artificial data generated using this p_T^W spectrum without the rapidity correlation are fitted to the nominal lineshapes, the returned W mass is shifted by $+20 \pm 10$ MeV/c^2 from the value at which it was generated. This shift is smaller than the systematic uncertainty taken for scaling and skewing the input p_T^W distribution. Note that we have no reason to believe the theoretical spectrum to be "correct" at this level, anyway. The theoretical model, which is thus close to the empirically derived spectrum we employ, may be used to isolate and estimate the bias due solely to correlations between p_T^W and rapidity. The shift in the mass between fits using this artificial data generated with and without the rapidity correlation included is 13 ± 14 MeV/c^2, which is consistent with no effect. To be conservative, 15 MeV/c^2 is taken as the corresponding systematic uncertainty.

6.4 Summary

The production model used to simulate $W \to e\nu$ events has been described. The uncertainties due to modeling are summarized along with all other uncertainties in Table 9.1. The choice of the p_T spectrum given to W bosons is constrained by scaling and skewing it until the predicted $u_\perp$ distribution disagrees with the data. The $u_{//}$ distributions are not used as a constraint but show good agreement. The result is a 30 MeV/c^2 uncertainty on the W mass. The modeling of the recoil is limited by the finite number of $Z \rightarrow ee$ events available to map out the calorimeter response and by the smearing on the p_T^Z measurement using electrons. These contribute a 60 MeV/c^2 uncertainty. The smearing of the electron energy measurement is constrained by the observed width of the $Z \rightarrow ee$ peaks and is shown to be consistent with expectations and with an estimate derived from the width of the E/p peak where the width of the $Z \rightarrow \mu\mu$ peak is used to estimate the contribution to the width from the tracking measurement. The corresponding uncertainty is 80 MeV/c^2. The choice of structure function does not make a detectable shift in the W mass, but the ability to measure such a shift, 40 MeV/c^2, is taken as a systematic uncertainty. The effect of higher-order diagrams on the W polarization contributes a 10 MeV/c^2 uncertainty. As a check, using a theoretically motivated p_T^W spectrum rather than the nominal one causes a 20 ± 10 MeV/c^2 shift on the measured mass, less than the systematic error assigned for the p_T^W modeling. Using this theoretical model, a possible rapidity bias is investigated and found to cause no measurable shift in the W mass; however, to be conservative, the ability to measure such a shift, 15 MeV/c^2, is taken as an uncertainty. Systematic uncertainties on the W width are also noted.

Chapter 7

BACKGROUNDS AND RADIATIVE CORRECTIONS

This chapter describes how the analysis accounts for the presence of backgrounds in the signal region.

7.1 Backgrounds

Processes other than $W \rightarrow e\nu$ in the mass samples may affect the mass measurement. This section describes how the presence of the following processes are incorporated into the analysis:

1. $W \rightarrow \tau\nu \rightarrow e\nu\nu\nu$
2. $Z \rightarrow ee$ where the second electron is not found
3. $W \rightarrow \tau\nu \rightarrow$ "one-prong" hadronic tau decays
4. "QCD": heavy-flavor decays and jets faking electrons
5. $Z \rightarrow \tau\tau$ where all decays of τ leptons are considered
6. WW and $t\bar{t}$ production.
7. cosmic rays

Most backgrounds have a lower average transverse mass than the signal and will cause the fitted mass to be lower than that from a fit to a background-free sample. The simulation directly includes contributions to the mass samples from these background processes. The backgrounds affect the value of $< u_{//} >$ and other properties of the dataset which serve as checks against systematic error, which is why the events are included directly in the simulation. In addition, backgrounds may preferentially populate the high E/p region in the $W \rightarrow e\nu$ sample, causing the amount of material inside the tracking volume to be overestimated. The uncertainty in the material measurement given in Chapter 4 is consistent with half of all non-electron backgrounds lying in the "tail" region of the E/p distribution. Each of the seven background processes is addressed in the following paragraphs.

The $W \rightarrow \tau\nu \rightarrow e\nu\nu\nu$ process is included by simulating the decays with their measured branching fractions [26] and determining the electron angular distributions accounting for the effect of polarizations on the decays. Few of these events pass the kinematic cuts. For M_W = 80.5 GeV/c^2, the final sample would contain 45 of its 5718 events from this process as shown in Table 7.2. This process is also included in the radiative simulation. This is the largest background and is also the easiest to include since the decay is precisely modeled.

Events where a Z is created can produce an isolated high-E_T electron in the CEM and a second electron mis-measured enough to be missed. This creates significant $\not{E}_T$ so that the event is classified as a $W \rightarrow e\nu$ event. The low rate of these events allows a correction calculated from `ISAJET` [51] and a general-purpose CDF detector simulation to be adequate. Because of the rapidity-dependence of the efficiency of the extra stiff track cut, a missed electron will tend to be in the forward regions. The kinematics and the residual energy deposited by the missed electron cause the transverse mass spectrum of

Cuts	f
$E_T > 20,\ p_T > 12,\ \not{E}_T < 20$	0.43 ± 0.07
$E_T > 20,\ p_T > 12,\ \not{E}_T < 10$	0.39 ± 0.08
$E_T > 25,\ p_T > 15,\ \not{E}_T < 20$	0.34 ± 0.11
$E_T > 25,\ p_T > 15,\ \not{E}_T < 10$	0.31 ± 0.14
$E_T > 30,\ p_T > 18,\ \not{E}_T < 20$	0.41 ± 0.21
$E_T > 30,\ p_T > 18,\ \not{E}_T < 10$	0.38 ± 0.17

Table 7.1: Variation in the ratio of jet events with an isolated track to those with a high track multiplicity for a range of kinematic cuts. Units on cuts are in GeV or GeV/c.

these events, shown as one of the curves in Figure 7.1, to fall rather than form a Jacobian peak. The spectrum of $u_{//}$ for these events has a long negative tail due to energy left by the missed electrons, which is included in the simulation.

The number of events in the sample due to hadronic jets being falsely identified as electrons and to electrons due to bottom and charm decays may be estimated from inclusive 20 GeV jet data. The distribution of the multiplicity of tracks with p_T greater than 1.0 GeV/c in the track isolation cone ($R < 0.25$) around the electrons is measured for jets passing the other electron identification cuts in events inconsistent with being a W or Z. The $Z \rightarrow ee$ data indicate that to separate background from signal events, it is necessary to look at events with four or more tracks within the isolation cone. The ratio of events with one isolated track to those with four or more tracks in the isolation cone, f, is measured from the jet data and is shown in Table 7.1 for a variety of cuts on the event topology. Varying the kinematic cuts, as shown in Table 7.1, shows that the measurement is robust against possible selection or $\not{E}_T$ biases, and indicates a background fraction of 11 in 5718 as shown in Table 7.2. Checks using different track multiplicity normalizations and samples enriched in heavy flavor are consistent with this background fraction. Events in the W sample which fail the track multiplicity cut are used to predict the shape of the background, shown in Figure 7.1.

It is necessary to consider the "one-prong" hadronic decays of tau leptons from W bosons. This is a background not normally considered in high-E_T electron analyses; however, this measurement is forced to use only loose cuts on the electron shower profile to reduce biases on events with bremsstrahlung of hard photons. The lack of tight matching cuts adds the possibility of $\tau \rightarrow \pi^+\pi^0 X$ events looking like isolated electrons for this analysis. Such events would also be likely to bias the tail of E/p. Another study using `ISAJET` and a general-purpose CDF detector simulation shows that the sum of the contributions from the decays $\tau^\pm \rightarrow h^\pm \nu X$, where $h^\pm$ is a charged pion or kaon, is small as shown in Table 7.2 and Figure 7.1. A 100% uncertainty is taken because of the simulation technique.

The number of events from the process $Z \rightarrow \tau\tau$ is estimated using `ISAJET` and the general-purpose CDF detector simulation. All decay modes of each τ are included in the simulation to account for cuts on event topology. The effect of this process on the W mass is small and is summarized in Table 7.2 and Figure 7.1.

The process of W-pair production is considered separately for direct production using a cross section of 10 pb [52] and for top-quark pair production with a top mass of 174 GeV/c^2 and cross section of 12.6 pb [53]. The contribution to the observed event rate is shown in Table 7.2. Since the sum of these processes produces fewer than one event in the sample and because they produce electrons originating from real W bosons, the processes are negligible and ignored.

Cosmic-ray muons may infrequently emit bremsstrahlung radiation

Decay	Events in $W \to e\nu$ sample
$W \to \tau\nu \to e\nu\nu\nu$	45
Lost $Z^0 \to ee$	7
$W \to \tau\nu \to$"one-prongs"	2
"QCD"	11
$Z^0 \to \tau\tau$	2
Direct WW	0.6
$t\bar{t}$	0.2
Cosmic rays	0

Table 7.2: Backgrounds in the W sample. To estimate the uncertainty due to backgrounds, the sum of all decays other than $W \to \tau\nu \to e\nu\nu\nu$ is varied by 100%.

in the CEM and appear as electrons. Of ~ 150 events failing only the 1.0 cm impact parameter cut, three are identified by an eye scan to be cosmic rays. These events are otherwise quiet, have muon hits aligned with the track on both sides of the detector and have hits in the CTC where the "other leg" was missed by the CTC track reconstruction. Extrapolating into the region with impact parameter less than the cut at 1 cm using a simple ratio indicates that 0.1 events are expected in the sample. As a check, events in the tails of the matching distributions are scanned and no events are seen. The process is negligible and ignored.

To measure the shift on the W mass from all backgrounds except $W \to \tau\nu \to e\nu\nu\nu$, which is considered adequately simulated, each background rate is increased by a factor of ten in the artificial data and the observed shift when these data are fit to the nominal templates is divided by nine (since one is already included). The inclusion of all these processes is seen to shift the W mass by 10 MeV/c^2 which is taken conservatively as the uncertainty.

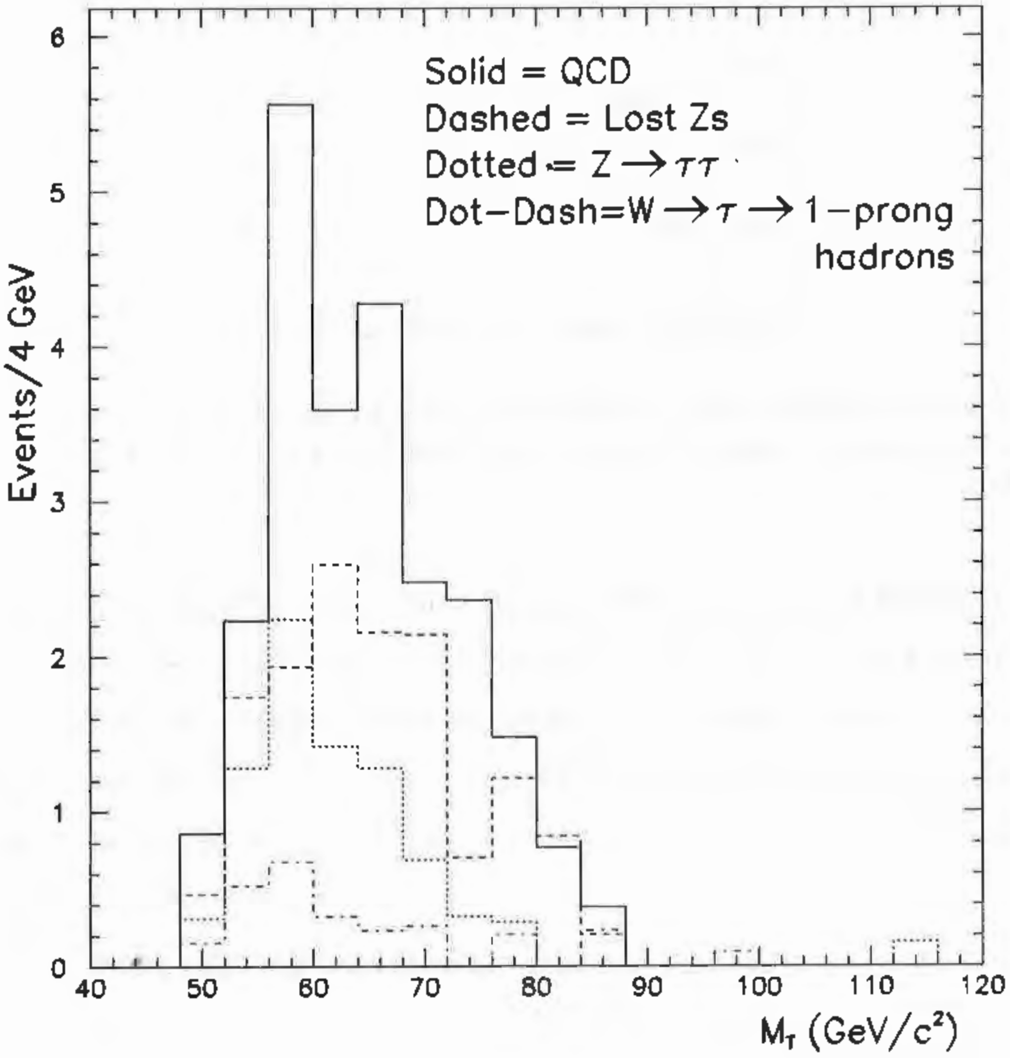

Figure 7.1: Transverse mass distribution of backgrounds in the $W \rightarrow e\nu$ sample (except $W \rightarrow \tau\nu \rightarrow e\nu\nu\nu$).

7.2 Radiative Corrections

The contribution of radiative W decay, $W \rightarrow e\nu\gamma$, is accounted for by using the same radiative simulation used to simulate the E/p spectrum. Most of the shift arises from wide-angle "internal-bremsstrahlung" photons which are radiated from the W propagator or electron external line. Either can cause the reconstructed transverse mass to be lower than would otherwise have been measured. In addition, although "external-bremsstrahlung" photons tend to be collinear with the electron, the effect coupled with the p_T cut on the electron or photon-electron separation in the magnetic field will affect the shape of the transverse mass spectrum. Both "internal" and "external" bremsstrahlung are included when calculating radiative corrections.

Artificial data are created at a known mass with the radiative effects included and fit with the nominal fitter. The simulation used is the same as that used to calculate the E/p shape as described in in Chapter 4. The observed shifts, listed in Table 7.3, are taken as corrections to the fitted mass. For example, the W mass returned from the nominal transverse mass fit will be shifted up by $+65 \pm 20$ MeV/c^2. The uncertainties are due to the finite number of events generated. The shift in $< u_{//} >$ due to radiative effects is +20 MeV/c^2 which is small enough to barely affect the comparisons made in Chapters 5 and 6. As a check, non-radiative events from the radiative simulation were seen to exhibit no shift in the fitted mass.

7.3 Summary

The $W \rightarrow e\nu$ mass measurement is highly insensitive to the presence of backgrounds. The presence of backgrounds is summarized in Table 7.2 and

Fit type	ΔM_W (MeV/c^2)	$\Delta\Gamma_W$ (MeV)
M_T	$+65 \pm 20$	
E_T^e	$+95 \pm 30$	
E_T^ν	-21 ± 30	
M_T (Γ_W floating)	$+58 \pm 24$	-65 ± 57

Table 7.3: Shifts to the W mass due to the fact that radiative effects are ignored in the nominal fit. The observed shift is applied to the fitted W mass.

Figure 7.1. A 10 MeV/c^2 uncertainty is taken on the W mass for the ability to model backgrounds.

Radiative corrections are applied as a shift to the fitted value of the W mass or width. The appropriate shifts for the various fits are listed in Table 7.3. Thus, the nominal fit, to transverse mass, is corrected upwards by 65 MeV/c^2 to account for the radiative shift.

Chapter 8

FITTING

This chapter describes the details of fitting the observed transverse mass spectrum to extract the W mass. The first section begins with a description of the transverse mass fitter. Checks of the internal consistency of the fitter follow. Checks of the fits are also made with the data. The nominal fit is compared to fits from the single-lepton E_T spectra. The mass fit is also made with the intrinsic width of the W floating. Jitter in the method is estimated. Likelihood contours for the floated-width and nominal (fixed-width) fits are shown.

8.1 Fitting Procedure

Although only the $W \to e\nu$ transverse mass fitter is described in detail here, the method is exactly the same as that used to fit the Z mass from the dielectron spectrum, the E/p spectrum, and the single-lepton E_T spectra. Transverse mass spectra are generated for a range of W masses 100 MeV/c^2 apart and W widths 200 MeV/c^2 apart. The range of transverse masses used in the fit is $65 < M_T^W < 100$ GeV/c^2, where 5718 of the 8067 events in the W dataset lie. At each mass-width point, an un-binned log-likelihood is calculated for the hypothesis that the data are consistent with that mass and width. An uncertainty on each point is calculated from the finite statistics used to generate each template. That is, the number of events in each bin of each template contributes a statistical uncertainty on the log-likelihood. Since the statistical uncertainties are well-described by a Gaussian, the log-likelihoods are expected to fit well to a paraboloid in the mass-width plane, which they do. The paraboloid's maximum corresponds to the best-fit value for the mass and width. The contour in the mass-width plane corresponding to an decrease of 0.5 in log-likelihood relative to the maximum defines the "1σ" confidence level. For fixed-width fits, the log-likelihoods are fit to a parabola.

8.2 Checks

Any fitting procedure must satisfy two criteria to show that it is reliable. First, when run on events from a large number of simulated experiments of the same size, the average returned value must be consistent with the nominal mass used to generate the events. Second, the RMS spread of the fitted masses in these experiments must be consistent with the mean statistical uncertainty returned by the fits.

To check these criteria, mock $W \to e\nu$ datasets of the same size as the real data are made at a known mass and width using the same simulation as used to make the templates. Fitting to 225 such datasets, the average of the returned masses is seen to agree with the nominal mass and their RMS spread agrees with the mean statistical uncertainty. Likewise, for the returned width. For example, the spread of returned masses for fixed-width fits to artificial data generated with M_W=80450 MeV/c^2 and Γ_W=2063 MeV/c^2 is shown in

M_T^W (min) (GeV/c^2)	ΔM_W (MeV/c^2)	
50	-47 ± 47	
55	-34 ± 47	
60	$+6 \pm 41$	
65	0	nominal
70	-41 ± 67	

Table 8.1: Difference from the nominal fit as the lower cutoff in transverse mass for the fit is varied. The uncertainty is an estimate of the independent statistical uncertainty (uncertainties subtracted in quadrature).

Figure 8.1. The mean, 80441 ± 10 MeV/c^2, agrees with the nominal value. The RMS spread, 133 ± 6 MeV/c^2, agrees with the mean fitted uncertainty of 144 MeV/c^2. The distribution of fitted masses is well described by a Gaussian and the fits of the log-likelihood points to parabolas are statistically consistent with $<\chi^2>= 1.0$, justifying the assumption of Gaussian statistical uncertainties. All fitters discussed in this thesis, whether one- or two-dimensional, pass these tests. Since each template consists of five million events, the fit is expected to have less than a 10 MeV/c^2 jitter independent of other uncertainties already included. A scatter of this maguitude is seen when refitting to statistically independent datasets and is taken as a systematic uncertainty due to "fitting."

The previous checks only tested the internal consistency of the fitters. Other checks are made with the data. The changes in the fitted mass as the lower and upper transverse mass cuts on the nominal fit are varied and shown in Tables 8.1 and 8.2. The shifts are consistent with the expected deviations from solely statistical variations due to the changing number of events as the fit window is changed.

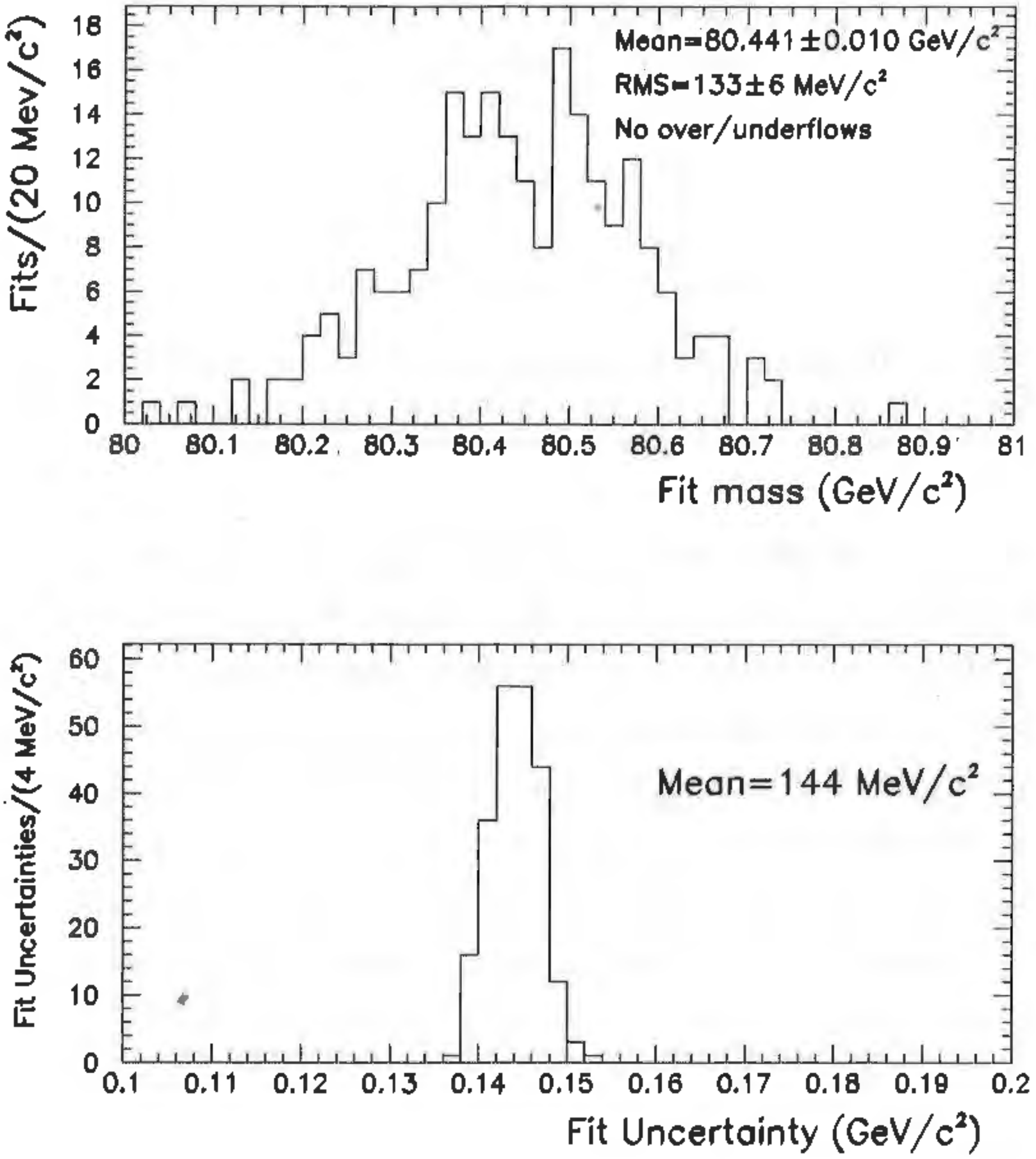

Figure 8.1: Upper: Distribution of returned masses for fixed-width fits to 225 mock $W \to e\nu$ datasets generated at M_W=80450 MeV/c^2. Lower: Distribution of returned statistical uncertainties in those fits.

M_T^W (max) (GeV/c^2)	ΔM_W (MeV/c^2)	
90	-44 ± 49	
95	-50 ± 24	
100	0	nominal
105	-1 ± 17	
110	0 ± 30	
120	-4 ± 34	
150	-11 ± 34	

Table 8.2: Difference from the nominal fit as the upper cutoff in transverse mass for the fit is varied. The uncertainty is an estimate of the independent statistical uncertainty (uncertainties subtracted in quadrature).

Fit type	ΔM_W (MeV/c^2)
Electron E_T fit	$+8 \pm 126$
$\not{E}_T$ fit	$+92 \pm 99$

Table 8.3: Shifts in the W mass as the fit type is changed from the nominal fit of the transverse mass spectrum to a fit of the single-lepton E_T spectra. The shifts are assigned an uncertainty due to the independent statistical uncertainty (uncertainties subtracted in quadrature).

Other fits, *i.e.*, those other than the nominal transverse mass fit, are sensitive to inadequate event modeling. Fits to the individual electron and neutrino E_T spectra are more sensitive to insufficient p_T^W modeling. The resulting shifts in the fitted W mass relative to the nominal value are summarized in Table 8.3. The deviations are consistent with the independent statistical uncertainty, *i.e.*, the statistical uncertainty that would have to be added in quadrature to the smaller uncertainty of the two numbers compared to produce the uncertainty on the other one. In fact, even a larger disagreement

Fit type	ΔM_W (MeV/c^2)
$\lvert\mathbf{u}\rvert < 5$ GeV fit	$+200 \pm 170$
$\lvert\mathbf{u}\rvert > 5$ GeV fit	-150 ± 155

Table 8.4: Shifts in the W mass as the fit type is changed from the nominal fit of transverse mass spectrum to one covering a different subset of $|\mathbf{u}|$. The shifts are assigned an uncertainty for the independent statistical and systematic uncertainties in the comparison. The two shifts are expected to be almost completely anti-correlated.

might be expected since some systematic uncertainties become larger. These spectra are compared to the prediction using the best-fit from the transverse mass in Figure 8.2. Fits may be made to the data split into two roughly equal samples. Those with $|\mathbf{u}| < 5$ GeV and those with $|\mathbf{u}| > 5$ GeV yield samples with 2770 and 2948 events in the fit range, respectively. The results of the two fits relative to the nominal, 5718-event sample are shown in Table 8.4. The shifts are highly anti-correlated so although the numbers are both one standard deviation away from zero, the numbers are dependent and this can be interpreted as only a single check. Note that the splitting is consistent with what would be expected from the apparent statistical fluctuation in $< u_{//} >$ and modest disagreements in the RMS values $u_{//}$ and $u_{\perp}$ with the simulation seen in Table 6.3. Moreover, since the p_T spectrum given to the boson was not retuned for this analysis, these shifts cannot be interpreted as shifts in the analysis had another $|\mathbf{u}|$ cut been used for the "nominal" measurement. Since the shifts cancel each other, the deviation, if real, likely corresponds to a skew of the boson p_T spectrum, which is already included in the systematic uncertainty in Chapter 6. The transverse mass spectrum for each of these

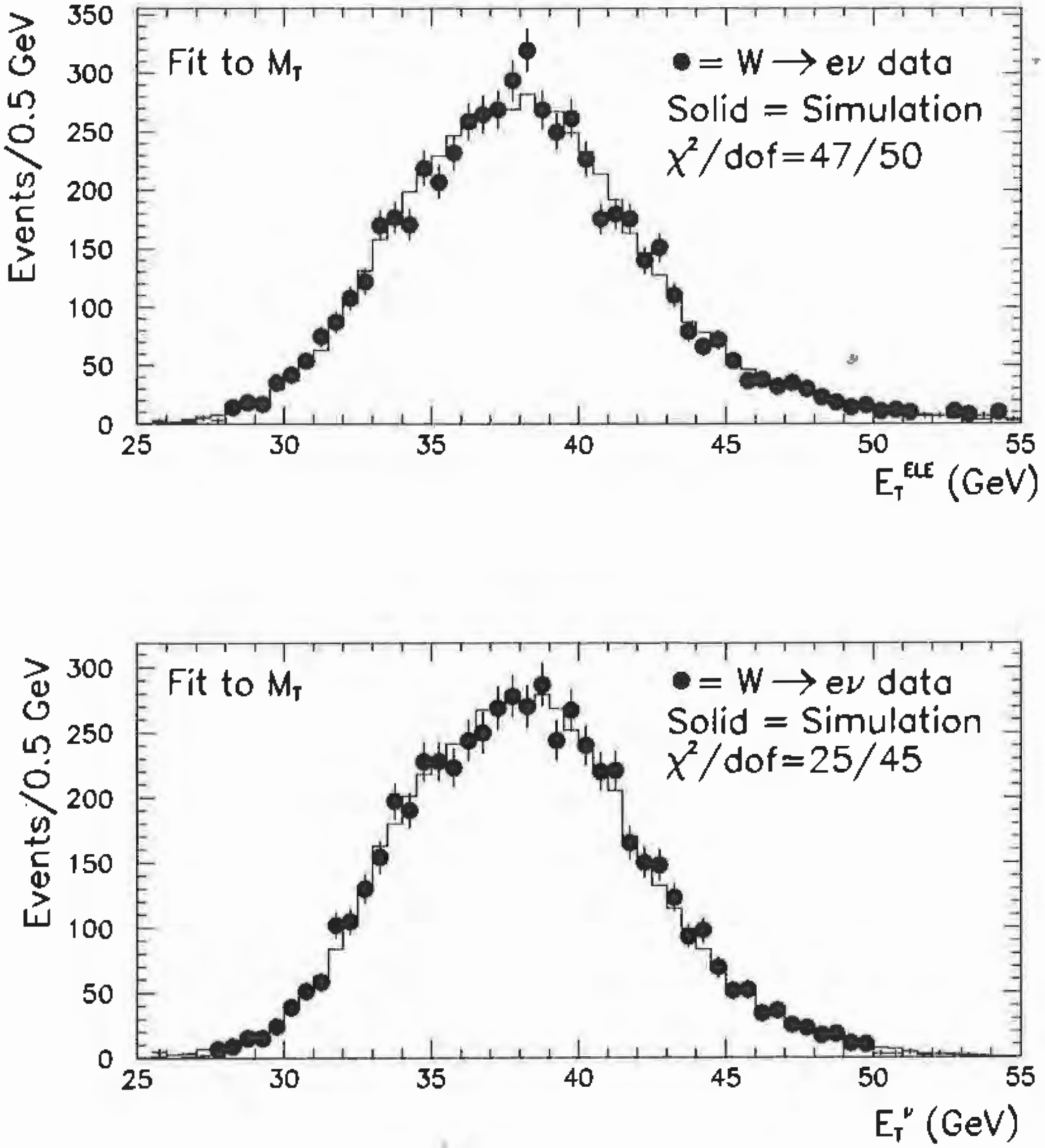

Figure 8.2: Upper: Electron E_T spectra compared to simulation. Lower: same for electron-neutrino E_T. Note that the mass value used for the simulation comes from a fit to the transverse mass, not the single lepton spectra shown.

samples is shown along with the prediction using the mass from the nominal fit in Figure 8.3.

Other checks of systematics are the best-fit W width when it is left floating in the fit and the shift in the best-fit mass when the width is left unconstrained rather than fixed. The best-value for the width from the $W \rightarrow e\nu$ data, after applying the radiative correction in Table 7.3, is

$$\Gamma_W = 2290 \pm 260(\text{stat.}) \pm 460(\text{syst.})\ \text{MeV/c}^2. \tag{8.1}$$

The systematic uncertainties on the width are estimated in the same way as those on the mass and were noted in the previous chapters. The width measurement is extremely sensitive to inadequacies of event modeling and agrees well with with the indirectly measured value of 2063 ± 85 MeV [30] and the directly measured value of 2040 ± 320 MeV [39]. The shift in the fitted mass when the width is allowed to from its nominal value of 2063 MeV is -68 ± 49 MeV/c^2, where the uncertainty represents the independent statistical uncertainty. The likelihood contours for the fitted mass and width for are shown in Figure 8.4.

If the mass difference between the W^+ and W^- were significantly different from zero, that would indicate that CPT symmetry would be broken. Probably any theory that one can imagine formulating must possess this symmetry. Since the electron energy measurements are charge-independent, the measurement of the mass difference is dominated by the statistical uncertainty and systematic uncertainties are negligible. Dividing the sample by charge, there are 2826 W^+ events and 2892 W^- events. The measured mass difference is

$$M(W^+) - M(W^-) = +680 \pm 290\ \text{MeV/c}^2, \tag{8.2}$$

where the same energy scale is used for the positively- and negatively-charged

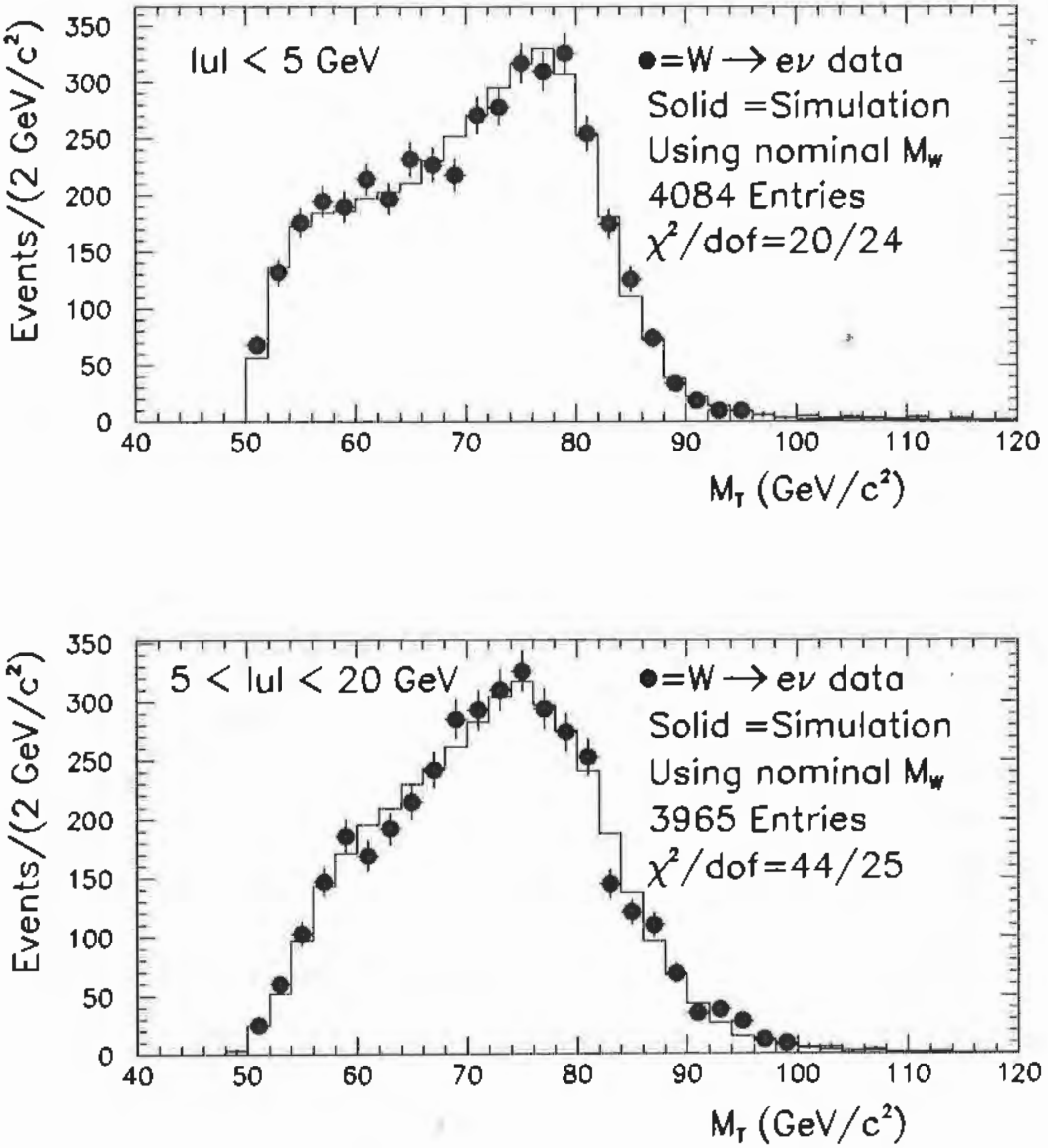

Figure 8.3: Transvserse mass spectra compared to the simulation using the mass value from the nominal fit. Upper: $|\mathbf{u}| < 5$ GeV. Lower: $|\mathbf{u}| > 5$ GeV.

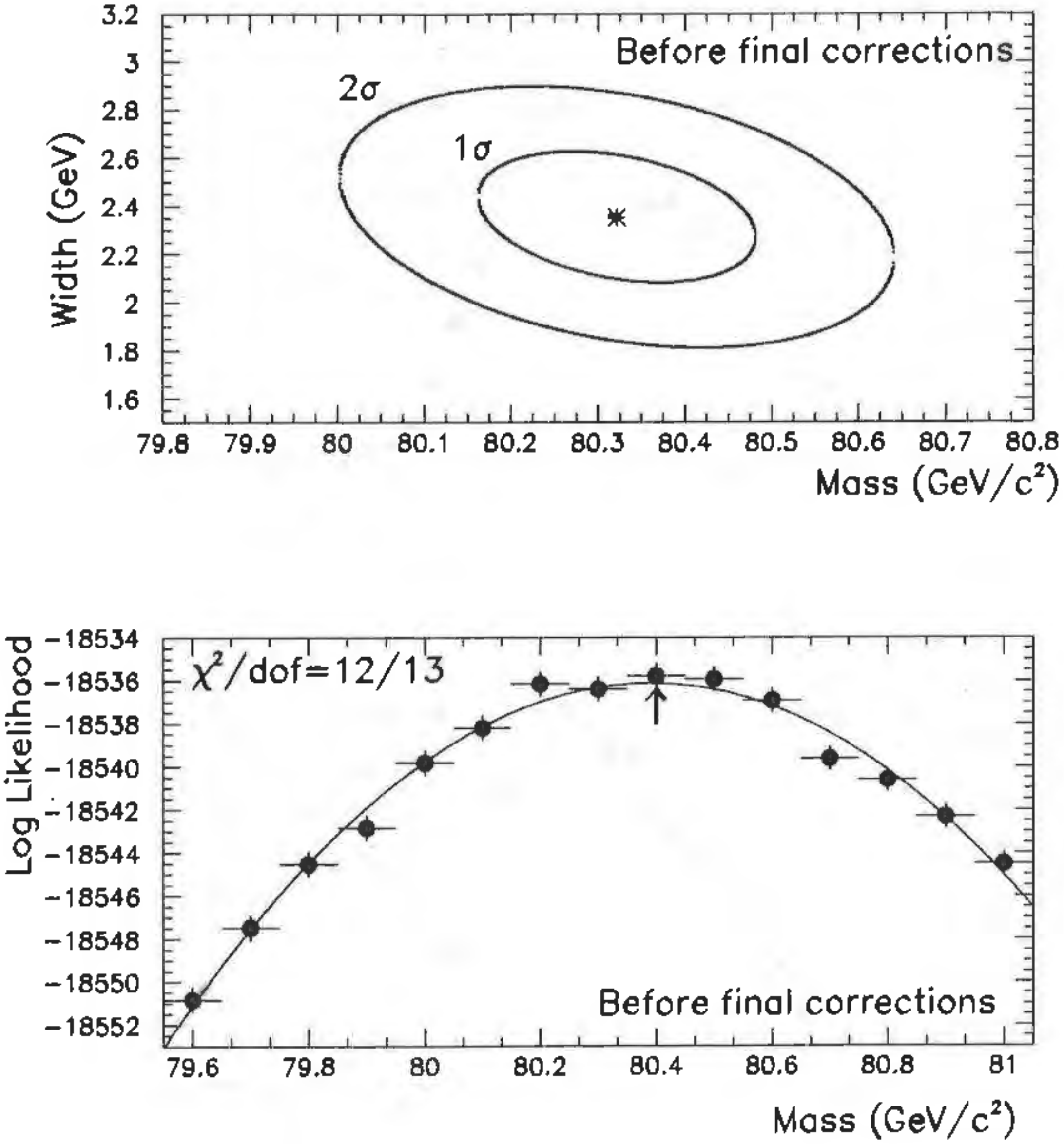

Figure 8.4: Upper: Log-likelihood contours for the simultaneous mass and width fit of the data. Lower: Log-likelihood points for the nominal (fixed-width) fits.

electrons. The result is a 2.3σ deviation. It goes the opposite direction from the previously measured value of -190 ± 580 MeV/c^2 by CDF [9]. Indirect tests comparing the decay rates of muons are about two orders of magnitude more sensitive to this mass difference.

8.3 Nominal Fit

The log-likelihood points for the nominal fit to the transverse mass spectrum are shown in Figure 8.4. The fit of the parabola to the points has $\chi^2/\text{dof} = 12.5/12$. To the fitted value is added 65 MeV/c^2 for the radiative correction described in Chapter 7 and a small shift to account for the 0.02% difference between the CEM scale used for the reconstruction and that obtained in the final scale calibration. The transverse mass and best fit for the electron data are shown in Figure 8.5.

The measured values of the W mass extracted from these fits are given in the final chapter.

8.4 Summary

This chapter described the fitting technique used throughout this thesis. The fits for the W mass demonstrate internal consistency. Other checks, using the data, show that the result is robust to changes in fit window and fit type. The result also reproduces the expected W width when allowed to float. A 10 MeV/c^2 uncertainty is taken due to the finite statistics used to generate the transverse mass lineshapes. The result from the nominal fit is given in the following chapter.

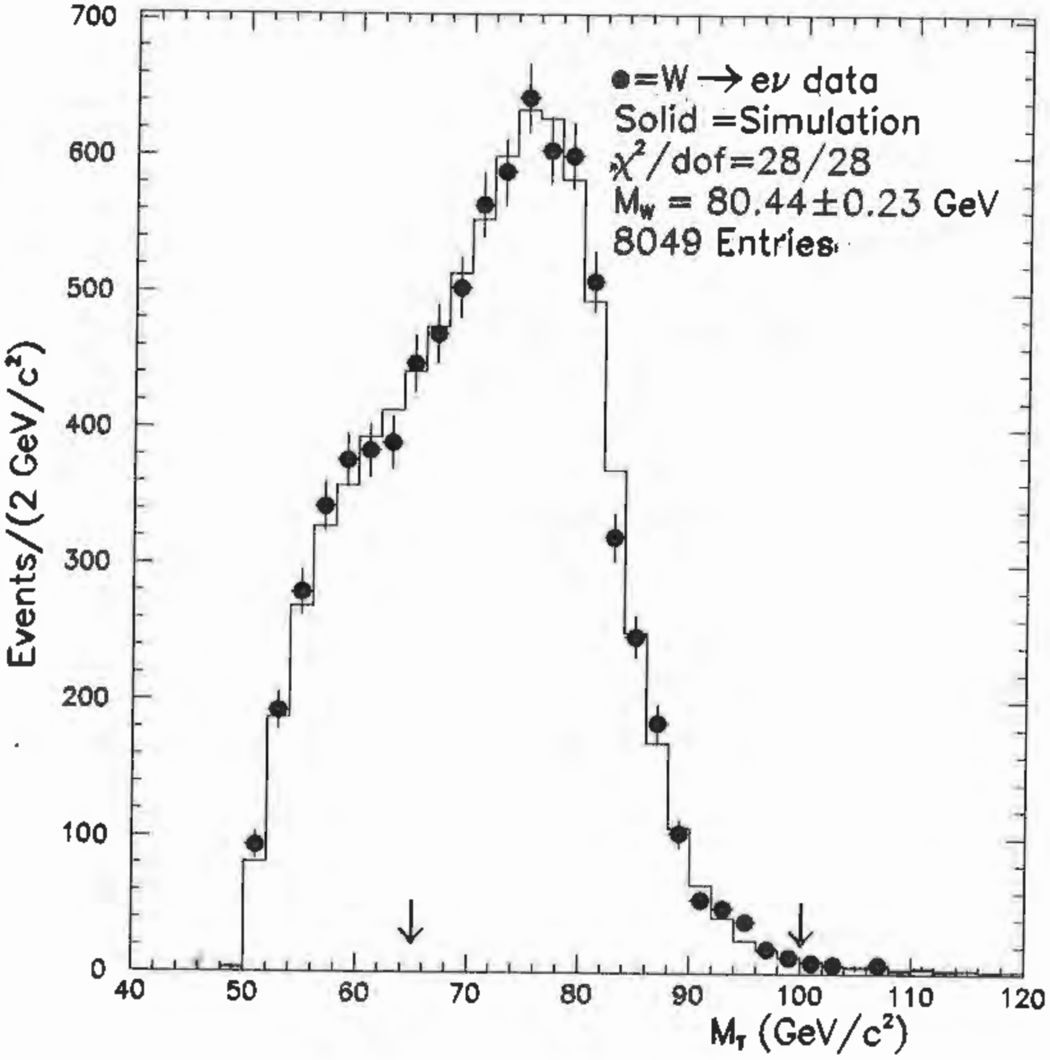

Figure 8.5: Transverse mass spectrum and the nominal fit.

Chapter 9

RESULTS AND IMPLICATIONS

This chapter presents a summary of the measured values and experimental uncertainties in the W mass measurement. The result is compared to previously published values. The implications of this measurement for the Standard Model are discussed.

9.1 Summary of Systematic Uncertainties

A summary of all systematic uncertainties discussed in this thesis is given in Table 9.1. All uncertainties have been rounded to the nearest 5 MeV/c^2. The statistical uncertainty of 145 MeV is determined from the fit. The systematic uncertainty due to knowledge of the energy scale, 130 MeV/c^2, is dominated by systematics of connecting the CTC momentum scale to the CEM energy scale. Other systematics uncertainties due to modeling and event selection add up to 110 MeV/c^2, of which the uncertainty on the electron resolution is largest, but was shown to be conservative. A conservative uncertainty

Quantity	ΔM_W (MeV/c^2)		
I. Statistical	145		
II. Energy Scale	130		
1. Scale from J/ψ		40	
2. Polar-angle false curvature		15	
3. Calorimeter		125	
a. Statistical unc. on E/p			65
b. Systematic unc. on E/p			105
III. Other Systematics	110		
1. Electron resolution		80	
2. Input p_T^W		30	
3. Recoil modeling		60	
4. W width		20	
5. Electron ID and removal		20	
6. Backgrounds		10	
7. Radiative correction		20	
8. Fitting		10	
IV. Theory	45		
1. Proton structure		40	
2. W polarization		10	
3. Rapidity vs. p_T correlation		15	
TOTAL UNCERTAINTY	230		

Table 9.1: Summary of statistical and systematic uncertainties in the W mass measurement.

due to theoretical choices, 45 MeV/c^2, does not contribute significantly to the total uncertainty. The total uncertainty, 230 MeV/c^2, is rounded to the nearest 10 MeV/c^2.

9.2 *W* Mass

The radiative corrections are applied to the fits to arrive at the measured mass values. The mass extracted is:

$$M_W = 80440 \pm 145(\text{stat.}) \pm 180(\text{syst.})\ \text{MeV/c}^2. \tag{9.1}$$

This result is shown alongside modern published results in Table 1.1 and in Figure 9.1.

9.3 Context

This mass measurement and the two previously published numbers shown in Figure 9.1 are consistent. No recent measurement is more than one experimental standard deviation away from the average. Combining published measurements with this one, the new world-average, after accounting for small correlated uncertainties among the measurements of up to 85 MeV/c^2, is

$$M_W^{\text{World}} = 80320 \pm 190\ \text{MeV/c}^2 \tag{9.2}$$

for which the measurements give χ^2/dof=0.71. The world-average will be improved when combined with the CDF analysis using the muon channel and with the measurement from the DZERO collaboration.

Measurements at the *Z* pole and at low energy can be used to infer values for the *W* mass which assume no new phenomena outside of the Standard Model. Fits to properties of the *Z* measured at LEP [32] may allow one

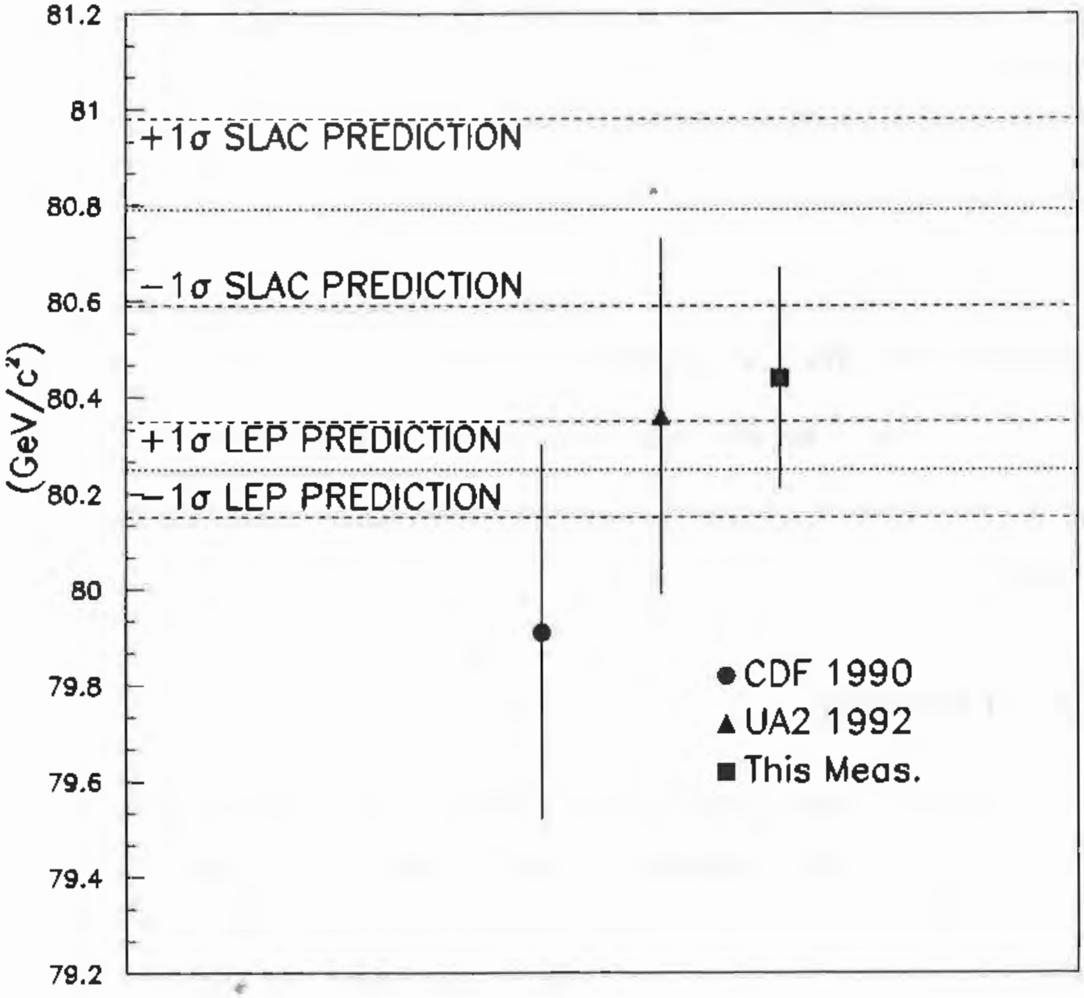

Figure 9.1: Previously published W masses and this measurement compared to the LEP and SLAC predictions. The prediction from deep-inelastic scattering experiments is not shown, but is given in the text.

to infer $M_W^{\mathrm{LEP}} = 80250 \pm 100$ MeV/c^2. The left-right asymmetry of the Z measured at SLAC [54] may be used to infer. $M_W^{\mathrm{SLAC}} = 80790 \pm 190$ MeV/c^2. Deep-inelastic neutrino scattering measurements may be used to infer $M_W^{\mathrm{DIS}} = 80240 \pm 250$ MeV/c^2 [55].

These results may be combined with other electroweak data to yield a prediction for the top quark mass. Or if the top quark mass presented recently by CDF [53] stands, one may check the consistency of the standard model using Figure 9.2.

9.4 Conclusion

A direct measurement of the W mass is one of the few measurements sensitive to the presence of new phenomena in the Standard Model of the electroweak interaction involving charged currents at high momentum transfer. A direct measurement of the W mass using both its electron channel has been described. The mass is measured with the CDF detector which is a combined magnetic spectrometer and calorimeter that allows many controls and checks of the energy scale and other systematic effects. This measurement, $M_W = 80440 \pm 230$ MeV/c^2, has a smaller uncertainty than any previously published direct measurement. The uncertainty will be less than 200 MeV/c^2 when combined with the concurrent measurement using the muon channel. The result indicates no deviation from the Standard Model.

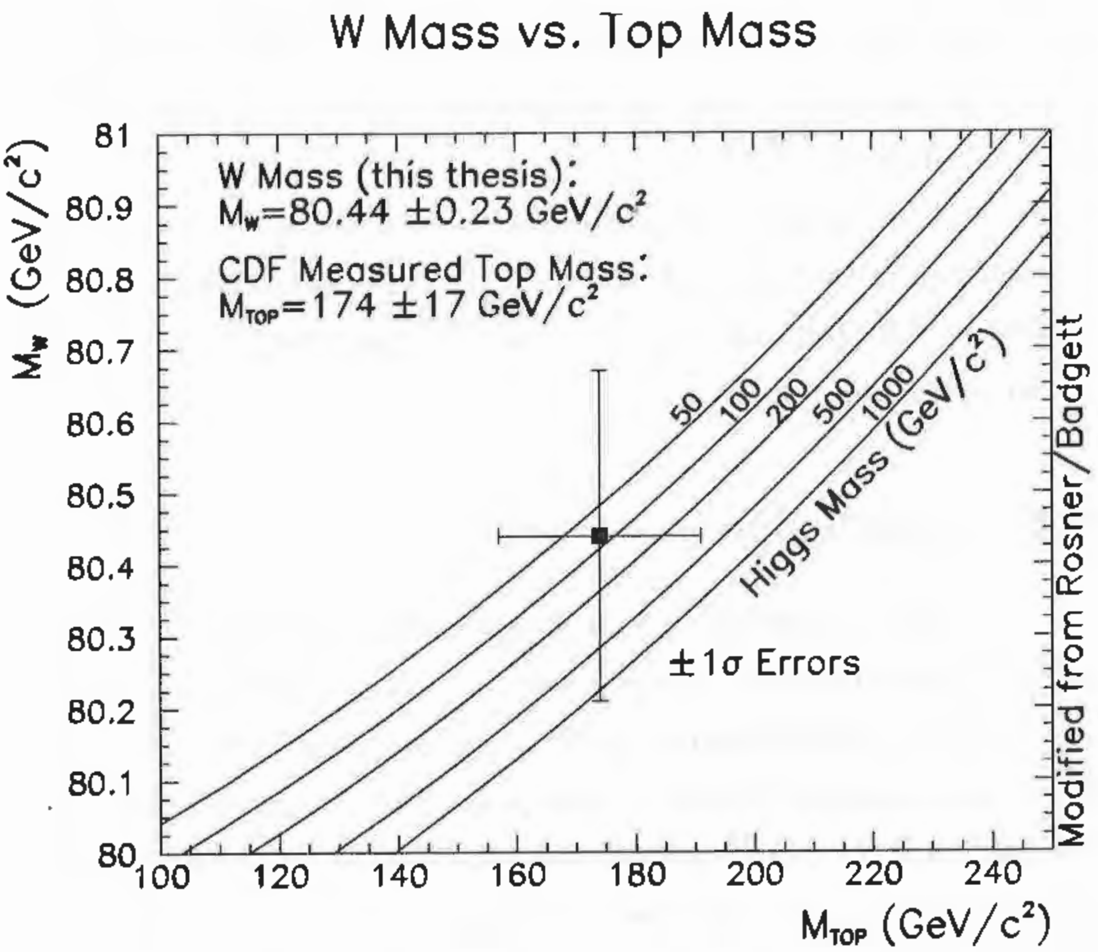

Figure 9.2: Theoretical calculation [2] of the dependence of the W mass on the top quark mass in the minimal Standard Model using several Higgs masses. The data point is the CDF measured top quark mass and the W mass measurement measured in this thesis.

Appendix A

WIDTH CONSTRAINT

This appendix suggests how one might reduce the systematic uncertainty on the W mass by $\sim 10\%$ by using the simultaneous width measurement as a further constraint on the systematic uncertainties due to resolutions.

In the W mass analysis there are systematic uncertainties due to uncertainties in the resolutions on the transverse mass. There are four major contributions to the smearing of the W transverse mass Jacobian peak: smearing of the input p_T^W distribution, smearing of the the **u** measurement, smearing in the electron energy measurement, and "smearing" due to the W width. Biases on the mass due to almost all of these sources of smearing of M_T^W appear to be at least qualitatively equivalent. In Figure A.1, each parameter representing a sources of systematic uncertainty is varied and the resultant mass shift (for a fixed-width fit) versus width shift (for a fit with mass and width floating) is shown. The correlation is evident. The "data" point uses the shift in the mass extracted from the data if the width is unconstrained in the fit; note that the uncertainties on this point are much smaller than the total

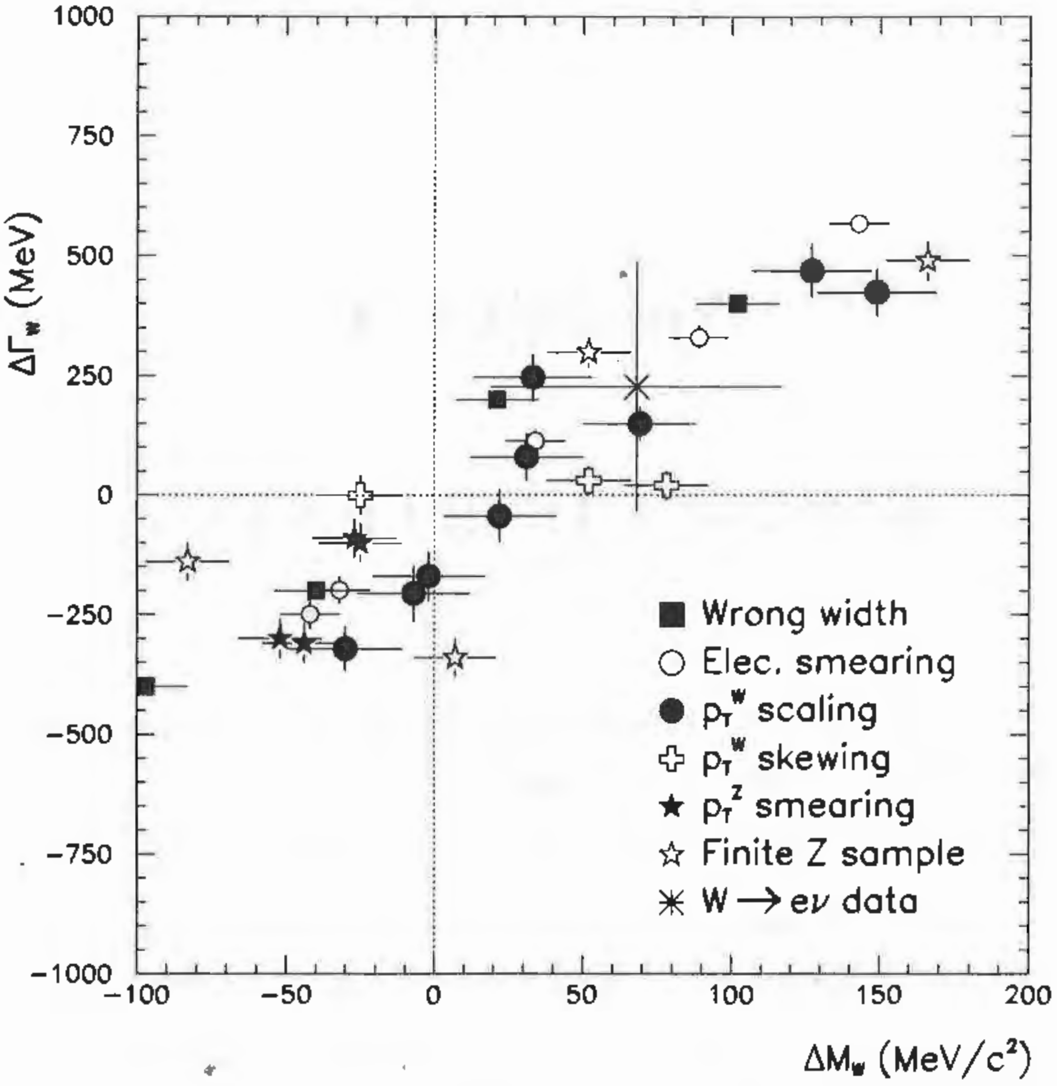

Figure A.1: Shift in the measured W mass (fixed-width fit) and width (fit with mass and width unconstrained) from the generated value as parameters characterizing systematic uncertainties are varied. The point for the "data" mass-shift uses the shift between the two types of fit; the shift for the "width" is relative to the nominal value of 2063 MeV. Note that the uncertainties on the differences for the data are much smaller than the total uncertainties on the mass and width.

uncertainties on the measured mass and width. The deviation of this point in mass-width space is consistent with that of most of the resolution errors.

The W width is extracted from the transverse mass spectrum at the same time as the mass in a fit with both mass and width floating. The width is extracted with a statistical uncertainty of 260 MeV. However, resolution systematics strongly affect the measurement of the W width, resulting in a systematic uncertainty of 460 MeV. One may make use of two facts. First, the W width is known much better from other measurements (2063 ± 85 MeV) [30] than from fitting the transverse mass spectrum. Second, since the statistical uncertainty on the width is smaller than the systematic uncertainty due to resolutions, constraining the width to agree with its indirectly measured value provides a further constraint on the bounds of resolutions. With the constraint applied, the systematic uncertainty on the W mass will be reduced.

This constraint is not the same as the fixed-width constraint in the fits. That reduces the statistical correlation which is present due to the shape of the Jacobian peak. The statistical correlation would remain even if the systematic uncertainties were negligible. Likewise, with infinite statistical power, the systematic correlation would remain. What is referred to in this Appendix is making use of the correlation in the systematic uncertainties due to resolution uncertainties.

The extracted W width is 2290 ± 260 (stat.) $\pm$ 460 (syst.) MeV. In the W mass measurement the total uncertainty is 230 MeV/c^2, where the contribution from the resolutions is 105 MeV/c^2. Given that the constraint, *i.e.*, the statistical uncertainty on the width, is smaller than the systematic uncertainty by a factor $\sim 260/460 = 0.56$, the width could serve as a better bound on the resolutions, thereby reducing their contribution to the systematic uncertainty on the W mass. Unfortunately, as seen in Figure A.1, not all the resolution uncertainties have the same slope in the ΔM versus $\Delta\Gamma$ plane. To account for these deviations an uncertainty of 100% is assigned to the derivative yielding a slope of $(30 \pm 30)\%$ for $\Delta M/\Delta\Gamma$. The width is also varied as if it were a resolution parameter and the mass shifts are seen in Figure A.1 to lie along that line.

Applying such a "width-constraint" to the measurement in the thesis, a small shift in the central value of the resolutions pertains since the fitted width did not lie exactly on the nominal W width. The constraint is combined with the constraints already applied, yielding a W mass measurement of

$$80400 \pm 145(\text{stat.}) \pm 160(\text{syst.})\ \text{MeV/c}^2. \tag{A.1}$$

Thus the systematic uncertainty on the W mass is reduced by 13% while the total uncertainty on the W mass is reduced by 7%. The shift in the W mass from that presented in Chapter 9 is only a 0.5σ systematic shift given the reduction in the systematic uncertainty.

One may check if this method might be optimized by a different choice of transverse mass fit range. If the upper transverse mass cutoff is reduced then both the statistical and systematic uncertainties on the width are expected to increase since there is less sensitivity to the tail of the W Breit-Wigner resonance. Changing the upper cutoff in transverse mass from 100 GeV/c^2 to 90 GeV/c^2 is seen to increase the statistical uncertainty on the W width by 52%; however, the systematic uncertainty due to the constant term increases by 62%. Presumably the effect of other resolutions behaves similarly. Since the power of this method goes as the ratio of the systematic uncertainty on the width to its statistical uncertainty, it appears that there is not much room for optimization. Note that fitting the $W \rightarrow e\nu$ data with the lower transverse mass cutoff does not significantly affect the fitted width, it shifts by -120 ± 790 MeV, becoming even closer to the indirectly measured value of 2063 ± 85 MeV.

The improvement is modest, but if the total uncertainty scales as the statistical uncertainty, this is equivalent to having $\sim$ 15% more data. The improvement from the concurrent muon analysis of CDF data may be similar. If nothing else, considering this relationship between the measured W mass and width provides an additional check that the values obtained in this thesis are reasonable. The usefulness of this method may improve as future measurements become increasingly limited by the systematic uncertainties.

Appendix B

COMMENT ON CHECKS

Many checks of the model and results have been made in this thesis. Of these, 21 have been identified as significant and independent and are listed in Table B.1 The root mean squared standard deviation from zero is 1.08±0.15, in good agreement with the expected value of 1.0. There are 14 entries with standard deviation less than 1.0, where one would expect 14.3. There are 4 entries between 1.0 and 2.0 where one would expect 5.3. There are 3 entries above 2.0 (all close to 2.0) where one would expect one.

Check	Standard deviations
$\Upsilon(1S)$ mass	0.41
$\Upsilon(2S)$ mass	0.35
$\Upsilon(3S)$ mass	2.25
$Z \rightarrow \mu\mu$ mass	0.52
B-field measurement	0.27
CEM constant term	0.07
$Z \rightarrow ee$ mass	1.38
W mass before and after access	0.21
$Z \rightarrow ee$ mass before and after access	2.14
$< u_{//} >$ offset	0.12
RMS $(u_{//})$	0.40
$k = 1.5$	1.50
Γ_W	0.43
E_T^e fit	0.06
E_T^ν fit	0.93
$M_T^{\text{min}} = 50$ GeV/c^2	1.00
$M_T^{\text{min}} = 70$ GeV/c^2	0.61
$M_T^{\text{max}} = 90$ GeV/c^2	0.90
$M_T^{\text{max}} = 150$ GeV/c^2	0.32
$\vert\mathbf{u}\vert < 5$ GeV	1.18
CPT-test	2.30
Root mean-squared deviation from zero	1.08 ± 0.15

Table B.1: List of 21 of the checks made in this thesis.

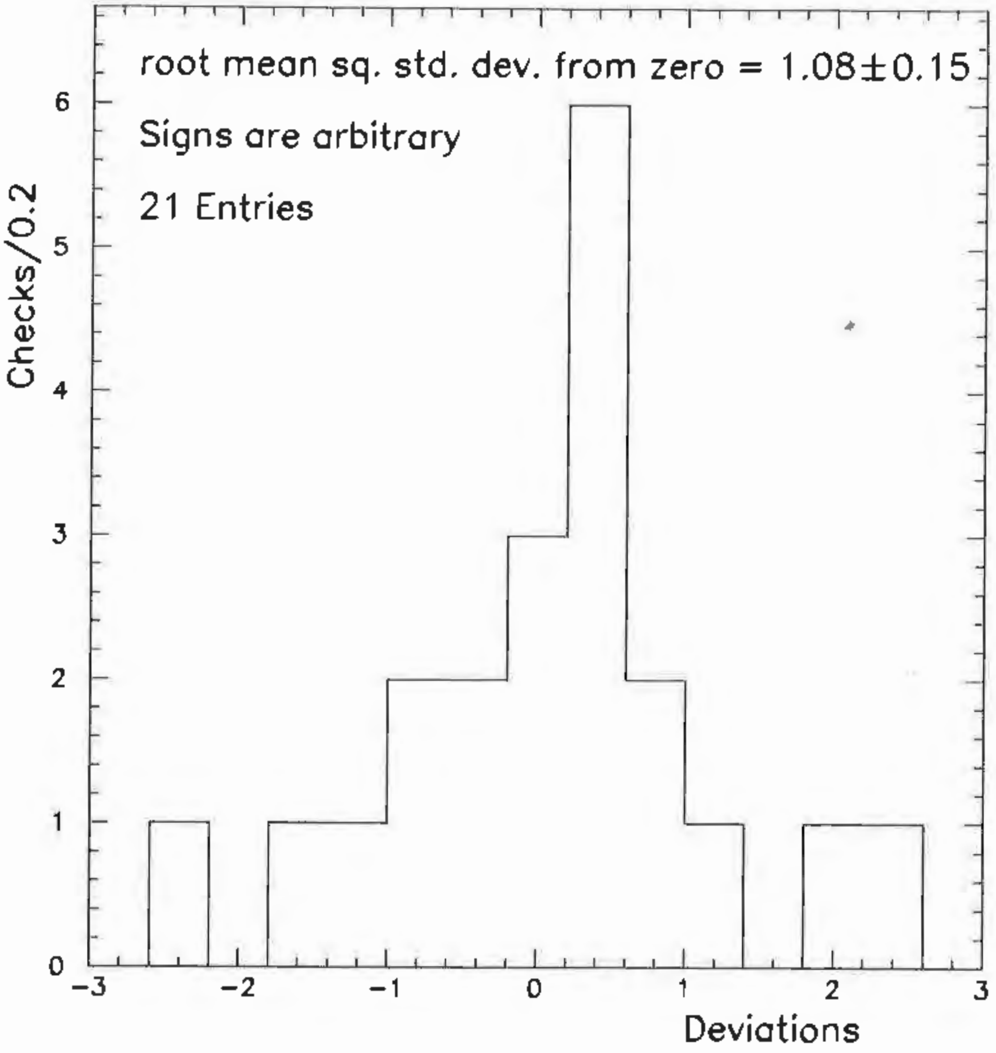

Figure B.1: Standard deviations of 21 of the checks made in this thesis. The "variance" is computed as the root mean squared standard deviation from zero.

REFERENCES

[1] S. L. Glashow, Nucl. Phys. **22**, 579 (1961); S. Weinberg, Phys. Rev. Lett. **19**, 1264 (1967); A. Salam, *Proceedings of the Eighth Nobel Symposium*, edited by N. Svartholm (Almqvist and Wiksells, Stockholm, Wiley, New York, 1968), p. 367.

[2] For a review, see J. L. Rosner, Rev. Mod. Phys., **64**, 1151 (1992); erratum, *ibid.*, **66**, 1117 (1994).

[3] G. Arnison *et al.* (UA1 Collaboration), Phys. Lett., **B122**, 103, (1983).

[4] M. Banner *et al.* (UA2 Collaboration), Phys. Lett. **122B** 476, (1983).

[5] G. Arnison *et al.* (UA1 Collaboration), Europhys. Lett., **1**, 327 (1986).

[6] R. Ansari *et al.* (UA2 Collaboration), Phys. Lett., **B186**, 440 (1987).

[7] F. Abe *et al.* (CDF Collaboration), Phys. Rev. Lett., **62**, 1005 (1989).

[8] J. Alitti *et al.* (UA2 Collaboration), Phys. Lett., **B241**, 150 (1990).

[9] F. Abe *et al.* (CDF Collaboration), Phys. Rev. Lett., **65**, 2243 (1990).

[10] J. Alitti *et al.* (UA2 Collaboration), Phys. Lett., **B276**, 354 (1992).

[11] L. Lederman, Scientific American, March 1991, 48.

[12] S. Drell and T. M. Yan, Phys. Rev. Lett., **25**, 316 (1970); erratum, *ibid.*, **25**, 902 (1970).

[13] F. Abe *et al.* Nucl. Instr. and Meth., **A271**, 387 (1988).

[14] F. Snider *et al.*, Nucl. Instr. and Meth., **A268**, 75 (1988). This is the reference for the previous generation of the device.

[15] F. Bedeschi *et al.*, Nucl. Instr. and Meth., **A268**, 50 (1988).

[16] D. Amidei *et al.*, Nucl. Instr. and Meth., **A269**, 51 (1988).

[17] L. Balka *et al.*, Nucl. Instr. and Meth., **A267**, 272 (1988); S. R. Hahn *et al.*, Nucl. Instr. and Meth., **A267**, 351 (1988); K. Yasuoka *et al.*, Nucl. Instr. and Meth., **A267**, 315 (1988); R. G. Wagner *et al.*, Nucl. Instr. and Meth., **A267**, 330 (1988); T. Devlin *et al.*, Nucl. Instr. and Meth., **A267**, 24 (1988).

[18] S. Bertolucci *et al.*, Nucl. Instr. and Meth., **A267**, 301 (1988).

[19] G. Ascoli *et al.*, Nucl. Instr. and Meth., **A268**, 33 (1988); G. Ascoli *et al.*, Nucl. Instr. and Meth., **A268**, 41 (1988).

[20] Y. Fukui *et al.*, Nucl. Instr. and Meth., **A267**, 280 (1988); W. C. Carithers *et al.*, "Proceedings of the Gas Sampling Calorimetry Workshop II," Batavia, Illinois, 54 (1985). S. Cihangir *et al.*, Nucl. Instr. and Meth., **A267**, 249 (1988); G. Brandenburg *et al.*, Nucl. Instr. and Meth., **A267**, 257 (1988).

[21] I am indebted to S. Kopp and C. Grosso-Pilcher for assembling and making available the CDF "good-run" list. Details are available in CDF internal note #1992.

[22] C. Newman-Holmes, E. E. Schmidt, and R. Yamada, Nucl. Instr. and Meth., **A274**, 443 (1989).

[23] D. Amidei *et al.*, Fermilab preprint, FERMILAB-PUB-94/024-E (1994).

[24] I am indebted to A. Mukherjee and L. Nodulman for providing the tracking calibrations. Details may be found in CDF internal notes #1002 and #2752.

[25] F. Abe *et al.* (CDF Collaboration), submitted to Phys. Rev. Lett. (1994); M. Dickson, Ph.D. dissertation, University of Rochester, 1994.

[26] M. Aguilar-Benitez *et al.* (PDG), *Review of Particle Properties* from Phys. Rev., **D45**, (1992).

[27] R. Keup, Ph.D. dissertation, University of Illinois, 1994.

[28] I am indebted to J. Hylen for this measurement. Details may be found in CDF internal note #2569.

[29] I am indebted to L. Nodulman and K. Byrum for this work. Details may be found in CDF internal notes #2046, #2291, and #2487.

[30] F. Abe *et al.* (CDF Collaboration), Phys. Rev. Lett., **73**, 220 (1994).

[31] I am indebted to S. Hahn and G. Houk for the Cesium-137 source calibrations. I am further indebted to them and and M. Hohlmann for the gain drift studies. Details may be found in CDF internal notes #2270 and #2280.

[32] M. Swartz, "High Energy Tests of the Electroweak Standard Model," XVI International Symposium on Lepton-Photon Interactions, 10-15 August 1993.

[33] F. A. Berends and R. Kleiss, Z. Phys., **C27**, 365 (1985).

[34] R. G. Wagner, Comput. Phys. Commun., **70**, 15 (1992).

[35] Y.-S. Tsai, Rev. Mod. Phys., **45**, 815 (1974).

[36] I am indebted to A. Castro, R. Kadel, P. Lukens, K. Ragan, R. Snider, J. Tonnison and others for assembling and scrutinizing the CDF database for the 1992-93 run.

[37] I am indebted to W. Ashmanskas, J. Hylen, R. Kadel, P. Lukens and A. B. Wicklund for their studies of photon conversions.

[38] I am indebted to S. Eno for developing this technique. Details may be found in CDF internal note #2063.

[39] S. Kopp, Ph.D. Dissertation, University of Chicago, 1994.

[40] I am indebted to Claudio Campagnari for providing me with his leading-order *W* and *Z* event generators.

[41] M. H. Reno, University of Iowa preprint UIOWA-94-01, 1994.

[42] A. D. Martin and W. J. Stirling, Phys. Rev., **B237**, 551 (1990).

[43] F. Abe *et al.* (CDF Collaboration), Phys. Rev. Lett., **66**, 2951 (1991).

[44] F. Abe *et al.* (CDF Collaboration), Phys. Rev. Lett., **67**, 2937 (1991).

[45] G. Marchesini and B. Weber, Nucl. Phys., **B310**, 461 (1988). I am indebted to S. Eno for performing this study.

[46] These results are consistent with a more detailed and more conclusive study of mass shifts versus *W* decay asymmetries performed by Y. K. Kim

and K. Einsweiler. Their study is available as a public CDF document, CDF Note #2618.

[47] H. Plothow-Besch, "PDFLIB: Nucleon, Pion and Photon Parton Density Functions and α_s Calculations, Users' Manual," ver. 4.17, CERN/1994.03.11.

[48] P. Chiappetta and M. Le Bellac, Z. Phys., **C32**, 521 (1986).

[49] P. B. Arnold and R. P. Kauffman, Nucl. Phys., **B349**, 381 (1991).

[50] I am indebted to Y. K. Kim for generating this Monte Carlo sample.

[51] F. Paige and S. Protopopescu, `ISAJET` version 6.43, FNAL publication PM0059 (1990).

[52] J. Ohnemus, Phys. Rev., **D44**, (1991) 1403.

[53] F. Abe *et al.* (CDF Collaboration), Phys. Rev. Lett., **73** (1994) 225; F. Abe *et al.* (CDF Collaboration), Phys. Rev., **D50** (1994) 2966.

[54] K. Abe *et al.* (SLD Collaboration), Phys. Rev. Lett., **73**, 25 (1994); M. Swartz, private communication.

[55] M. Shaevitz, Neutrino 94 Conference, Eilat, Israel, May 29, 1994.